Structural and Functional Analysis of Catalase-peroxidases

by

Benjamin Wiseman

A thesis

submitted to the Faculty of Graduate Studies

in partial fulfillment of the requirements for the degree of

DOCTOR OF PHILOSOPHY

Department of Microbiology

University of Manitoba

Winnipeg, Manitoba

Canada

ABSTRACT

Catalase-peroxidases (KatGs), responsible for the activation of the anti-tubercular prodrug isoniazid (INH), are unusual members of the class I plant peroxidase family that possess strong catalase activity as well as peroxidase activity. Due to their strong catalase activity and their ability to activate INH, KatGs have been the subject of intense study for many years, and thus the goal of this work is to further characterize this enzyme in the hope of gaining a better understanding into these unusual reactions. Recent successful crystallization of a few representative KatGs revealed a unique covalent Met-Tyr-Trp cross-link joined to the conserved tryptophan in the heme active site, along with a nearby arginine that is in ionic association with the cross-linked tyrosine. Using the KatG from *Burkholderia pseudomallei* (BpKatG) as a model, site-directed mutagenesis to these residues revealed that they were essential for catalase, but not peroxidase activity. Structural and kinetic analysis revealed that Arg426 acts as a molecular switch, moving between 2 conformations, favoring heme oxidation when not in association with Tyr238 and favoring heme reduction when in association with Tyr238 by imparting its influence on the heme through the cross-link. Analysis of the reaction with peroxyacetic acid using stopped-flow spectrophotometry revealed an initial, rapidly formed enzyme-substrate complex before the formation of the oxoferryl compound I. Kinetic characterization revealed that formation of both the enzyme-substrate complex and the oxoferryl species were dependent on peroxyacetic acid concentration implying that 2 molecules of peroxyacetic acid are required to form the oxoferryl compound I intermediate. Successful co-crystallization with INH and its co-substrate, NAD^+ has revealed their binding sites for the first time in a KatG. The NAD^+ binding site is 20 Å from the entrance to the heme cavity, involving interactions primarily with the ADP portion of the molecule. The best defined INH binding site is located in a funnel shaped channel on the opposite side of the protein from the entrance channel that requires the movement of a glutamate residue for binding. The structures suggest that once INH is cleaved to the isonicotinoyl radical it diffuses to the NAD^+ binding site to form the final active antimicrobial compound, IN-NAD, in a non-enzymatic reaction enhanced by the enzyme's ability to bind NAD^+.

ACKNOWLEDGEMENTS

First and foremost I would like to thank my advisor Dr. Peter Loewen for giving me the opportunity to work in his lab and for his guidance and continuous support over the years. I would also like to thank the members of my advisory committee, Dr. Harry Duckworth, Dr. Ivan Oresnik, and Dr. Pavel Diprov for their thoughtfulness and many useful suggestions throughout the course of this work. I would also like to thank the external examiner Dr. Joanne Turnbull for her very thorough reading of this thesis; her comments and suggestions have surely made this thesis better. I am very grateful to Jack Switala, and everybody in the lab, Rahul Singh, Taweewat Deemagarn, Vikash Jha, and Jacylyn Villanueva for all of their suggestions, technical help and more importantly their friendship. To our collaborators in Vienna, Dr. Christian Obinger and Dr. Christa Jakopitsch for introducing me to stopped-flow and looking after me during my visit. Similarly, to our collaborators Dr. Anabella Ivancich and Dr. Julie Colin in Paris, and Dr. Andy Smith at the University of Sussex for making me feel welcome during my visits to their labs, and their expertise in EPR and stopped-flow spectroscopy. To our collaborators Dr. Ignacio Fita and Dr. Xavier Carpena in Barcelona for the crystallography and NMR that is endlessly referenced throughout this thesis. To the staff at the protein crystallography beamline at the Canadian Light Source at the University of Saskatchewan for all their assistance in data collection. Finally, to Sharon Berg and the all the faculty, staff, and students in the Department of Microbiology for their kindness and assistance over the years.

TABLE OF CONTENTS

LIST OF FIGURES

Figure **Page**

LIST OF TABLES

Table **Page**

LIST OF ABBREVIATIONS

A	Absorbance
ABTS	2,2'-azinobis(3-ethylbenzothiazolinesulfonic acid)
ADP	Adenosine diphosphate
AMP	Adenosine monophosphate
Amp^R	Ampicillin resistant
Å	Angstrom
APX	Ascorbate peroxidase
ATP	Adenosine triphosphate
BLC	Bovine liver catalase
bp(s)	Base pair(s)
BpKatG	Catalase-peroxidase from *Burkholderia pseudomallei*
CBB	Coomassie Brilliant Blue
C*c*P	Cytochrome *c* peroxidase
CHES	N-Cyclohexyl-2-aminoethanesulfonic acid
Ci	Curie
CIP	Calf intestinal alkaline phosphatase
Δ	Change
Da	Dalton
dATP	Deoxyadenosine triphosphate
DEAE	Diethylaminoethyl
DMSO	Dimethylsulfoxide
DNA	Deoxribonucleic acid
dNTP	Deoxyribonicleotide triphosphate
ε	molar extinction coefficient
EcKatG	Catalase-peroxidase from *Escherichia coli*
EDTA	Ethylene diamine tetraactic acid
EPR	Electron paramagnetic resonance
g	Gram
HmKatG	Catalase-peroxidase from *Haloarcular marismortui*
HPI	Hydroperoxidase I
HPII	Hydroperoxidase II
HRP	Horseradish peroxidase
INH	Isonicotinic acid hydrazide or isoniazid
kbp(s)	Kilo base pair(s)
k_{cat}	Turnover number
kDa	KiloDalton
K_M	Michealis-Menten constant
L	Liter
LB	Luria-Bertani
μL	Microliter
μM	Micromolar
M	Molar
mg	Milligram
min	Minute

mL	Milliliter
mM	Millimolar
MPD	2-methyl-2,4-pentanediol
msec	millisecond
MtKatG	Catalase-peroxidase from *Mycobacterium tuberculosis*
NAD	Nicotinamide adenine dinucleotide (oxidized)
NADH	Nicotinamide adenine dinucleotide (reduced)
NADPH	Nicotinamide adenine dinucleotide phosphate
ng	Nanogram
nm	Nanometer
NMR	Nuclear magnetic resonance
OD	Optical density
PAA	peroxyacetic acid
PAGE	Polyacrylamide gel electrophoresis
PCR	polymerase chain reaction
PEG-4K	polyethylene glycol 4000
Por	Porphyrin
$Por^{\bullet+}$	Porphyrin π-cation radical
psi	pounds per square inch
RNA	Ribonucleic acid
RNase	Ribonuclease
ROS	Reactive oxygen species
SDS	Sodium dodecyl sulfate
sec	Second
SOD	Superoxide dismutase
STD	Saturation transfer difference
SynKatG	Catalase-peroxidase from *Synechocystis PCC 6803*
TAE	Tris-acetate-EDTA
TBE	Tris-borate-EDTA
TE	Tris-EDTA
U	Units
V	Volts
V_i	Initial velocity
V_{max}	Maximum velocity
v/v	Volume per unit volume
w/v	Weight per unit volume

Ever tried. Ever failed. No matter. Try again. Fail again. Fail better.

-Samuel Beckett

1. GENERAL INTRODUCTION

1.1. Oxygen and life

Oxygen was almost nonexistent in earth's early atmosphere and thus life originally evolved in an anaerobic world. These early organisms evolved about 3.8 billion years ago without the selective pressure on their metabolic and biochemical pathways to avoid the reactivity of oxygen. However, about 2.5 billion years ago photosystem II appeared and oxygen levels slowly started to rise. Organisms then began to use oxygen as a terminal electron acceptor to produce adenosine triphosphate (ATP). The process of cellular respiration using O_2 enabled aerobic organisms to produce much more ATP than anaerobic organisms, helping them to dominate Earth's biosphere. Photosynthesis and cellular respiration of O_2 allowed for the evolution of eukaryotic cells and ultimately complex multicellular organisms such as plants and animals (Campbell and Reese, 2005).

1.1.1. Oxidative stress

The increased production of energy in the form of ATP using O_2 as a terminal electron acceptor comes at the cost of generating reactive oxygen species, including superoxide anion ($O_2\bullet^-$), and hydrogen peroxide (H_2O_2) as dangerous by-products. Hydrogen peroxide, although not a radical can react in the presence of divalent metal ions such as iron and copper to produce the highly damaging hydroxyl radical (HO•). The paramagnetic nature of molecular oxygen makes it an ideal candidate for use as a terminal electron acceptor, although 1 electron transfer to O_2 generates partially reduced and reactive species. As shown

in the scheme below, when molecular oxygen is reduced with 1 electron, a superoxide anion radical is produced which in turn can then be further reduced with another electron to generate hydrogen peroxide. Hydrogen peroxide can then suffer homolytic cleavage to generate the highly reactive (and strongest oxidant found in biological systems) hydroxyl radical.

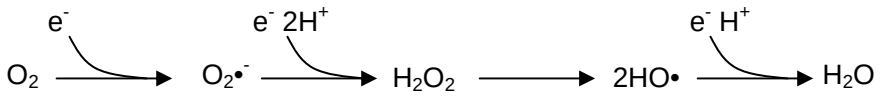

Studies in *E. coli* have determined that approximately 15 μM of hydrogen peroxide and 5 μM of superoxide anion are generated per second during exponential growth (Imlay, 2008). These species are generated from a variety of sources, including enzymatic (NADH oxidase, succinate dehydrogenase, and fumerate reductase) and environmental (ultraviolet radiation, heavy metals, and hydrogen peroxide diffusing passively into the cells) (Imlay, 2008). These partially reduced forms of oxygen, or reactive oxygen species, are lethal to cells and can oxidatively destroy iron-sulfur clusters of enzymes, damage DNA and cell membranes, and modify amino acids (Storz and Imlay, 1999). For example, DNA is particularly susceptible to damage from the hydroxyl radical, and enzymes that use an iron-sulfur cluster $[4Fe\text{-}4S]^{2+}$ can be oxidized and inactivated by hydrogen peroxide and superoxide anions (Imlay, 2008).

1.1.2. Oxidative defense mechanisms

To protect themselves against the damage caused by reactive oxygen species, cells have developed a number of antioxidant enzymes that are capable of scavenging superoxide anions and hydrogen peroxide. These enzymes can be

placed into 3 general groups: superoxide dismutases, catalases, and peroxidases, which also include catalase-peroxidases.

Superoxide dismutases were originally discovered by Irwin Fridovich and Joe McCord and consist of 3 major classes, depending on the metal cofactor: Cu/Zn type, Fe and Mn type, and the Ni type (McCord and Fridovich, 1988). As their name implies, they dismutate the superoxide anion to molecular oxygen and hydrogen peroxide (reaction 1).

$$2O_2\bullet^- + 2H^+ \rightarrow H_2O_2 + O_2 \qquad (1)$$

Catalases are found in all domains of life and clearly divide into 3 groups: the typical monofunctional catalase, the bifunctional catalase-peroxidase, and the non-heme catalases (Nicholls *et al*, 2001). Although the details differ significantly among the 3 groups, the overall reaction catalyzed by catalases is the degradation of 2 molecules of hydrogen peroxide into water and oxygen (reaction 2) and will be discussed in detail in the following sections.

$$2H_2O_2 \rightarrow 2H_2O + O_2 \qquad (2)$$

Peroxidases are another diverse group of enzymes that are ubiquitous in nature. They can be divided into 2 main groups: plant peroxidases and animal peroxidases. Similar to catalases, peroxidases catalyze the degradation of hydrogen peroxide to water, but rely instead on a variety of biomolecules available in the cell as reductants (R in reaction 3). They will be discussed in greater detail in the following sections.

$$2H_2O_2 + 2RH \rightarrow 2H_2O + 2R \qquad (3)$$

In addition to these scavenging enzymes that act as the primary defense against reactive oxygen species, there are many other enzymes that are capable of repairing damage already done. For example, methionine sulfoxide reductases can reverse methionine oxidation, proteases can hydrolyze damaged proteins, and endonucleases can remove oxidized bases from nucleic acids (Stortz and Imly, 1999).

1.2. Monofunctional heme catalases

Catalases have been extensively studied for over 100 years since their discovery in tobacco leaf (Loew, 1901) and have since been found in all domains of life. Currently there are over 2000 sequences and 13 crystal structures available (Chelikani *et al*, 2004) for the monofunctional heme catalase making them one of the most studied classes of enzymes.

1.2.1. Distribution and phylogeny

Monofunctional catalase sequences can be sub-grouped into 3 groups or clades that have arisen from a minimum of 2 gene duplication events (Klotz and Loewen, 2003). Clade 1 catalases are predominantly of plant origin with a few algal and bacterial representatives. Clade 2 includes all large subunit catalases (>75 kDa) of bacterial and fungal origins (HPII of *E. coli* is a clade 2 catalase). Clade 3 enzymes are all small subunit catalases (<60 kDa) from bacteria, archea, and eukaryotes (Klotz and Loewen, 2003). Overall, catalases do not group according to 16S rRNA based species phylogenetic relationships. For example, the *B. fragilis* and *M. barkeri* catalases group closely together on the phylogenetic

tree, although the organisms are rather distantly related (Klotz and Loewen, 2003).

The large subunit, clade 2 catalases have extended N- and C- termini, missing in clade 1 and clade 3, that appears to enhance thermal stability and prevent degradation due to proteolysis (Switala *et al*, 1999). Thus, it appears that the large subunit, clade 2 catalases are the common ancestor for both clade 1 and 3 after a gene duplication event followed by a loss of sequence. Also, the absence of clade 3 catalases from older taxonomic species suggests that enzymes from this group were the last to develop (Klotz and Loewen, 2003).

1.2.2. General structural and biochemical properties

Most monofunctional catalases are active as tetramers (although hexamers, and even an unusual trimer from *Desulfovibrio gigas* (Santos *et al*, 2000) have been reported) and contain 1 non-covalently bound heme b or heme d molecule per subunit. Although catalases only follow typical Michaelis-Menten kinetics at very low substrate concentrations, observed turnover numbers ranging from 54,000 sec^{-1} to 833,000 sec^{-1} and K_M values 38 to 599 mM H_2O_2 have been reported (Chelikani *et al*, 2004). The small subunit catalases become inactivated by hydrogen peroxide at concentrations above 300 mM and large subunit catalases only suffer inactivation above 3 M (Chelikani *et al*, 2004). The robust nature of these enzymes is quite amazing considering the chance of a microbe encountering such harsh conditions is virtually impossible (except in a laboratory, of course). Also some of the small subunit, clade 3 catalases are capable of binding NADPH, whereas neither clade 1 nor clade 2 can. Clade 1 catalases lack

the required residues to bind NADPH, and a portion of the extended C-terminal sequence of clade 2 catalases protrudes into the binding site making NADPH binding impossible. Recently, it has been speculated that NADPH binding helps prevent enzymatic inactivation by protecting the reactive ferryloxo intermediate Compound I against deactivation to the catalytically inactive intermediate Compound II (Sicking *et al*, 2008).

To date, 13 crystal structures of monofunctional catalases from different organisims have been determined including 4 clade 1 catalases from *Pseudomonas syringae* (CatF), *Exiguobacterium oxidotolerans* (EKTA) (Hara *et al*, 2007) and *Vibrio salmonicida* (VSC) (Riise *et al*, 2007); 3 clade 2 catalases from *Penicillium vitale* (PVC) (Vanishtein *et al*, 1981 and 1986), *Escherichia coli* (HPII) (Bravo *et al*, 1995 and 1999), and *Neurospora crasa* (Cat1) (Diaz *et al*, 2004), and 7 clade 3 catalases from *Bos taurus* (liver) (BLC) (Murthy *et al*, 1981, Fita *et al*, 1986, and Ko *et al*, 1999), *Proteus mirabilis* (PMC) (Gouet *et al*, 1995), *Saccharomyces cerevisiae* (CATA) (Berthet *et al*, 1997, and Maté *et al* 1999), *Homo sapiens* (erythrocyte) (HEC) (Puntam *et al*, 1999), *Micrococcus lysodeikticus* (MLC) (Murshudov *et al*, 1982), *Helicobacter pylori* (HPC) (Loewen *et al*, 2004), and *Enterococcus faecalis* (Håkansson *et al*, 2004). In addition, a catalase like domain has been found fused to an allene oxide synthase from *Plexaura homomalla* (AOS) (Oldham *et al*, 2005), but it lacks catalase activity. As shown in Fig. 1.1, the characteristic features of a typical catalase structure include a core beta barrel containing a deeply buried heme active site accessed by 2 or 3 channels (Chelikani *et al*, 2004). Clade 3, small

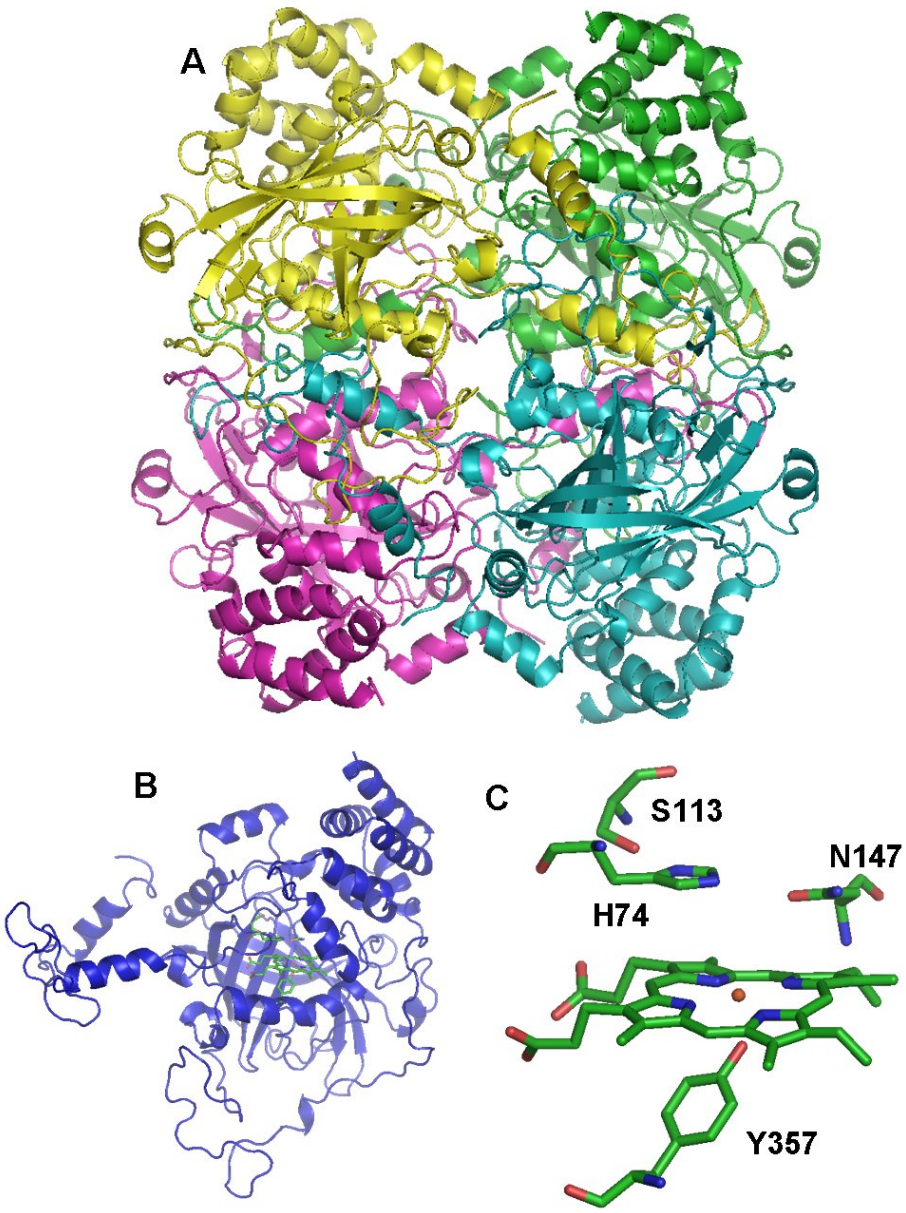

Figure 1.1. Crystal structure of beef liver catalase. Panel A: 4 subunits in relation to each other. Panel B: a single subunit. Panel C: the catalytically important residues in the heme active site. This figure was prepared with coordinates submitted to the protein data bank (PDB id: 4BLC).

subunit catalases, have a common active site orientation with the histidine imidazole ring over ring III of the heme b (Chelikani *et al*, 2004). However in clade 2, large subunit catalases the orientation of the heme is flipped with respect to the active site histidine followed by oxidation to form a cis-hydroxyspirolactone group on ring III (Nicholls *et al*, 2001).

The deeply buried heme active site is connected to the surface by 2 or 3 channels. The primary access route for hydrogen peroxide to the heme active site is a main access channel that approaches the heme perpendicular to its plane. The second and third channels are referred to as minor and their roles are not yet clear, although a possible role in the release of reaction products has been discussed (Carpena *et al*, 2003). A structure-function study of conserved residues in the main access channel has suggested that an electrical potential created between a negatively charged aspartate side chain and the positively charged heme iron may act on the electrical dipoles of water and hydrogen peroxide molecules entering the heme cavity to orient them optimally for reaction (Chelikani *et al*, 2003). Disruption of this potential field by mutation of the aspartate results in reduction of catalase activity.

1.2.3. The heme active site and catalytic mechanism

Once hydrogen peroxide has reached the deeply buried heme, it encounters a highly conserved active site consisting of 4 relatively invariant residues that are essential for catalase activity and integrity of the enzyme. These residues include a histidine, a serine, an asparagine, and a tyrosine (H74, S113, N147, and Y357 in BLC respectively) (Nicholls *et al*, 2001) as shown in Fig. 1.1.

On the heme's distal side, an essential histidine (H74) is located roughly 3.5 Å above and almost parallel with the heme next to an asparagine (N147) which is roughly 6.0 Å from the heme. The heme's proximal side consists of a coordinated tyrosine (Y357) that makes up the fifth ligand to the heme iron (Fita and Rossmann, 1985).

All monofunctional catalases have a common 2-step mechanism for the degradation of hydrogen peroxide into water and oxygen. In the first step, 1 molecule of hydrogen peroxide oxidizes the heme to generate an oxyferryl intermediate called compound I (reaction 1). In the second step, a second molecule of hydrogen peroxide reduces compound I to regenerate the resting, ferric enzyme releasing oxygen and water (reaction 2).

$$\text{Enz (Por-Fe}^{III}\text{)} + H_2O_2 \rightarrow \text{CpdI (Por}^{\bullet+}\text{-Fe}^{V}\text{=O)} + H_2O \qquad (1)$$

$$\text{CpdI (Por}^{\bullet+}\text{-Fe}^{V}\text{=O)} + H_2O_2 \rightarrow \text{Enz (Por-Fe}^{III}\text{)} + H_2O + O_2 \qquad (2)$$

Compound I is a short lived catalytic intermediate consisting of a porphyrin cation radical characterized by a distinctive absorption spectrum resulting in an approximate 50 % decrease in intensity in the Soret band at 406 nm with respect to the resting, ferric enzyme (Nicholls *et al*, 2001). When a peroxide molecule enters the heme cavity, it is sterically forced between His74 and Asn147 before interacting with the heme (Fita and Rossmann, 1985). His74 acts as a general acid-base catalyst by hydrogen-bonding and accepting a proton from hydrogen peroxide. The interaction is stabilized by Asn147 with additional hydrogen bonding leading to scission of the peroxide O-O bond with 1 oxygen being transferred to the heme iron to generate compound I and the other being released

as water (Fita and Rossmann, 1985). Compound I reduction to regenerate the resting state enzyme also involves the same residues. His74 acts as a proton acceptor from the hydrogen peroxide in a complex further stabilized by Asn147. The second hydrogen of the hydrogen peroxide is transferred to the oxoferryl oxygen allowing the release of molecular oxygen and water with the enzyme returning to the ferric state.

1.3. Non-heme catalases

Some microorganisms, which are unable to synthesize heme, can nevertheless produce a catalase (Kono and Fridovich, 1983). Most catalase-positive microorganisms that cannot synthesize heme contain non-heme or manganese containing catalases. This class of catalase is largely restricted to eubacteria and the minor catalase activity is likely only to have significance in modern anaerobic bacteria such as clostridia and some lactobacilli (Klotz and Loewen, 2003). An interesting exception to this are species of *Methanobrevibacter* isolated from the hind gut of termites (Leadbetter *et al*, 1998) that cannot synthesize heme but produce a typical monofunctional heme-catalase and thus must import heme from the surrounding environment to produce an active enzyme (Shima *et al*, 2001).

Mn-catalases are not as wide spread as classic heme-containing catalases, and have only been identified in bacteria (Chelikani *et al*, 2004). Evolutionarily, the Mn-catalases seem to have appeared sometime between the monofunctional catalases and the much later appearing catalase-peroxidases (Klotz and Loewen, 2003). As their name implies, they do not contain a heme active site, and a

dimanganese cluster is found in the active center, 1 cluster in each of the 6 subunits of the hexamer (Chelikani *et al*, 2004, and Kono and Fridovich, 1983). They exhibit a much lower reactivity towards hydrogen peroxide with a Vmax that is only 1/100 that of monofunctional catalases and a K_M value of 250 mM for H_2O_2 (Kono and Fridovich, 1983). It has been suggested that the low activity in comparison to typical catalases could be the reason for them not becoming more widespread in nature (Chelikani *et al*, 2004).

1.4. Monofunctional heme peroxidases

Heme peroxidases are ubiquitous in all kingdoms of life and have been extensively studied for well over a century. In fact, the amount of material in the scientific literature is staggering as noted by a 2 volume review citing well over 5000 references (Gaspar *et al*, 1982 and 1992). The first reported observation of a reaction catalyzed by a peroxidase was in 1810 when a beautiful blue color was noted upon treatment of powdered resin tree heartwood with horseradish roots (Planche, 1810, and Veitch, 2004) and have since become model enzymes.

1.4.1. Disribution and phylogeny

Heme peroxidases can generally be classified into 2 superfamilies that arose independently. The plant superfamily of (archae)bacterial, fungal, and plant heme peroxidases is represented by catalase-peroxidases (KatG), ascorbate peroxidases (APX), cytochrome *c* peroxidases (C*c*P), manganese and lignin peroxidases, and plant secretory peroxidases (Passardi *et al*, 2007). The second superfamily (named the peroxidase-cyclooxygenase or animal peroxidase superfamily) includes the mammalian peroxidases represented by

myeloperoxidase (MPO), eosinophil peroxidase (EPO), lactoperoxidase (LPO) and thyroid peroxidase (TPO) (Zámocky *et al*, 2008b). Both superfamilies differ greatly in their primary and tertiary structures and thus this overview will concentrate on the plant superfamily.

On the basis of sequence similarities Karen Welinder was able to organize the plant peroxidase superfamily into 3 classes (Welinder, 1992). Class I contains peroxidases of prokaryotic origin including yeast cytochrome *c* peroxidase, ascorbate peroxidases and catalase-peroxidases. Class II contains secreted fungal peroxidases including lignin peroxidase, manganese peroxidase and ink cap mushroom peroxidase. Class III contains classical secretory plant peroxidases including the intensely studied horseradish peroxidase, peanut peroxidase and barley peroxidase (Welinder, 1992).

Interestingly, APX appears to be present in only chloroplastic organisms, C*c*P is mainly restricted to organisms containing mitochondria, and KatGs are mainly found in bacteria and some fungi (Passardi *et al*, 2007). Class II peroxidases are involved in lignin degradation and only found in the Homobasidiomycetes, whereas Class III peroxidases are restricted to higher plants (Passardi *et al*, 2007). It has also been suggested that class I peroxidases arose from a nonduplicated peroxidase sequence from an ancestral bacterium and that this ancestral peroxidase was probably present in the bacterium that gave rise to the mitochondrion and chloroplast (Passardi *et al*, 2007). Also, it appears that class I peroxidases are at the origins of both class II and III peroxidases, because

the ancestor of class II is most likely C*c*P and organisms containing class III peroxidases lack any C*c*P encoding genes (Passardi *et al*, 2007).

1.4.2. General structural and biochemical properties

Monofunctional plant peroxidases are typically found as monomers ranging in mass from 30 to 40 kDa with 1 non-covalently bound heme b molecule (Bonagura *et al*, 2003). As shown in Fig. 1.2, the crystal structure of yeast C*c*P was originally solved in 1980 (Poulos *et al*, 1980), and subsequently refined to higher resolution in 1984 (Finzel *et al*, 1984). The crystal structure of pea cystolic ascorbate peroxidase did not appear until 1995 (Patterson and Poulos, 1995) and soybean ascorbate peroxidase in 2003 (Sharp *et al*, 2003). The structures reveal a protein with a high alpha helical content and a non-covalently bound heme in the core of the protein about 10 Å from the nearest surface (Erman and Vitello, 2002). The overall helical topology is highly conserved among the plant peroxidases with a root mean square deviation of the corresponding alpha-carbons between C*c*P and APX of only 1.3 Å (Patterson and Poulos, 1995). Both peroxidases have the distal active site triad Arg-Trp-His and proximal His-Trp-Asp triad typical of the class I peroxidases. The only significant differences noticed between C*c*P and APX were a small 8 amino acid deletion adjacent to the active site in APX and a potassium binding site present in pea APX (Patterson and Poulos, 1995), but not C*c*P.

Class II peroxidases share the same overall topology as class I but also possess 2 calcium ions and 4 conserved disulfide bridges. The proximal tryptophan residue, conserved in class I peroxidases, is replaced with either a

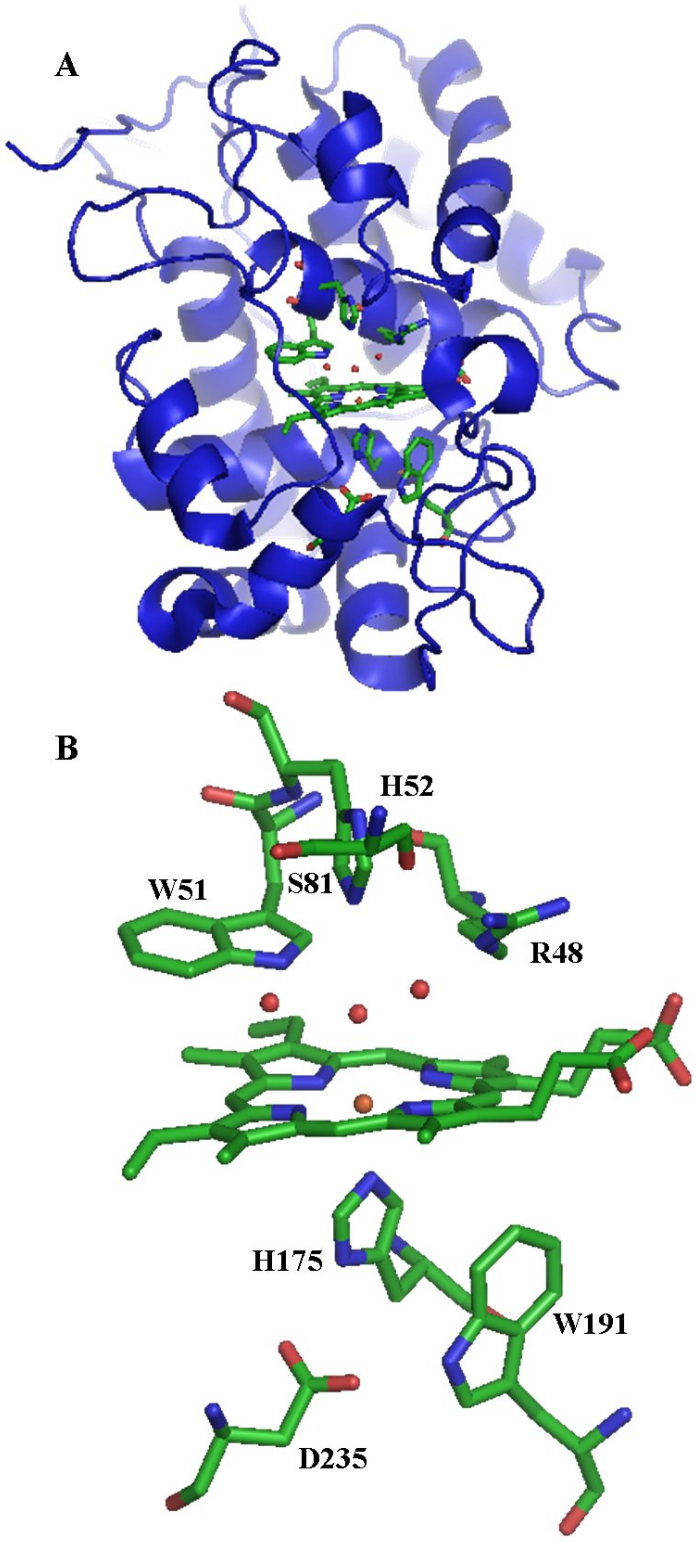

Figure 1.2. Crystal structure of yeast cytochrome *c* peroxidase. Panel A: ribbon diagram of the monomeric enzyme. Panel B: the catalytically important residues in the heme active site. This figure was prepared with coordinates submitted to the protein data bank (PDB id: 1CCP).

phenylalanine or a leucine residue (Dunford, 1999). Available crystal structures of class II peroxidases include lignin peroxidase (Edwards *et al*, 1993, and Poulos *et al*, 1993), manganese peroxidase (Sundaramoorthy *et al*, 1994), and the identical *Coprinus cinereus* (Petersen *et al*, 1994) and *Arthromyces ramosus* peroxidases (Kunishima *et al*, 1994 and 1996).

Class III peroxidases again share the overall topology as class I and like class II peroxidases bind 2 calcium ions and have 4 conserved disulfide bridges. In addition, both the proximal and distal tryptophans are replaced by phenylalanine (Dunford, 1999). Available crystal structures of class III peroxidases include peanut peroxidase (Schuller *et al*, 1996), barley peroxidase (Henriksen *et al*, 1998), and the extensively studied horseradish peroxidase (Gajhede *et al*, 1997).

1.4.3. The heme active site and catalytic mechanism

As shown in Fig. 1.2, the heme active site is buried within a crevice and is accessible by a short access channel with the edge of the heme group (heme b) about 10 Å from the nearest molecular surface (Erman and Vitello, 2002). In C*c*P and APX the heme active site consists of the conserved His175-Trp191-Asp235 triad (C*c*P numbering) proximal to the heme with His175 coordinated to the heme iron and Trp191 parallel and in Van der Waals contact with the imidazole of His175 and the heme group (Erman and Vitello, 2002). The side chain of Asp235 is hydrogen bonded to both His175 and Trp191. On the distal side of the heme the conserved Arg48-Trp51-His52 triad is present in C*c*P and APX with the tryptophan side chain stacked parallel to the heme (Erman and Vitello, 2002). In

classes II and III the conserved proximal tryptophan (W191) is replaced with either a phenylalanine or a leucine and in class III peroxidases the conserved distal tryptophan (W51) is also replaced with a phenylalanine (Dunford, 1999).

Using nothing more than the 1980 crystal structure of yeast C*c*P Thomas Poulos and Joseph Kraut suggested a mechanism for the transfer of an oxygen atom from hydrogen peroxide to the heme iron (Poulos and Kraut, 1980). Two features of this remarkable work have stood up to scrutiny and later confirmed through site-directed mutagenesis studies (Erman and Vitello, 2002): 1) the distal histidine (H52) is a proton acceptor from hydrogen peroxide; and 2) the distal arginine (R48) is a charge stabilizer. Notice that the active site tryptophan (W51) does not a direct play a role in the initial step of hydrogen peroxide reduction. There is some evidence that Trp51 may help stabilize compound I once it has already formed (Erman and Vitello, 2002).

Unlike catalases, these enzymes are capable of catalyzing the dismutation of hydrogen peroxide into oxygen and water at only a very low rate, if at all. The first step, common to both catalases and peroxidases in the enzymatic mechanism is the reduction of hydrogen peroxide to water generating an enzymatic intermediate known as compound I. This intermediate originates from the 2 electron oxidation of the native enzyme by hydrogen peroxide that generates the oxoferryl moiety and the concomitant formation of a porphyrin π-cation radical ($Por^{\bullet+}$) and subsequently a protein-based radical in some enzymes (Ivancich *et al*, 2003) (reaction 1). However, unlike monofunctional catalases, monofunctional peroxidases are not capable of reducing compound I back to the ferric resting

state with a second molecule of hydrogen peroxide (reaction 2). Instead, they rely upon electron donors (peroxidase substrate) in a 2-step, 1 electron reduction cycling through a second enzymatic intermediate compound II (reactions 1 and 2). These radical and reaction intermediates are routinely detected and distinguished from one another via electron paramagnetic resonance (EPR) (Ivancich *et al*, 2003) and stopped-flow absorption spectroscopy.

$$\text{CpdI (Por}^{\bullet+}\text{-Fe}^{V}\text{=O) + AH} \rightarrow \text{CpdII (Por-Fe}^{IV}\text{-OH) + A}^{\bullet} \qquad (1)$$

$$\text{CpdII (Por-Fe}^{IV}\text{-OH) + AH} \rightarrow \text{Enz (Por-Fe}^{III}\text{) + H}_2\text{O + A}^{\bullet} \qquad (2)$$

The peroxidase substrate (AH in reactions 3 and 4) is enzyme specific as reflected in peroxidase nomenclature. For example ascorbate peroxidase has a high affinity for ascorbate as its peroxidase substrate while cytochrome *c* peroxidase reacts with cytochrome *c*. However, peroxidases like horseradish peroxidase are capable of reacting with multiple substrates including aromatic phenols, phenolic acids, indoles, amines, and sulfonates (Veitch, 2004).

1.4.4. Radical sites in C*c*P and APX

As mentioned above, the transfer of an oxygen atom from hydrogen peroxide to the heme iron generates an oxoferryl species known as compound I. The concomitant formation of a porphyrin π-cation radical ($Por^{\bullet+}$) or in some cases a subsequent protein-based radical (Ivancich *et al*, 2003) quickly follows. It remains difficult to predict why, despite the high sequence similarity and virtually identical active sites, radicals at different sites, including the porphyrin and several different tyrosine and tryptophan residues, are preferentially stabilized in different proteins.

It has been long known that cytochrome *c* peroxidase produces a tryptophanyl radical upon formation of compound I (Dunford, 1999, and Erman and Vitello, 2002). In the Poulos-Kraut mechanism of compound I formation (Poulos and Kraut, 1980) they predicted that this radical must reside on the distal side tryptophan (W51). This active site residue seemed the most logical with the indole ring of the tryptophan about 3.6 Å above and parallel to the heme pyrrole ring (Poulos *et al*, 1980). However, through site directed mutagenesis and EPR studies this was later been shown not to be the case (Sivaraja *et al*, 1989). Replacement of the proximal tryptophan (W191) with a non-oxidizable phenylalanine decreased without eliminating enzymatic activity, but did eliminate the radical signal as detected by EPR. This residue which lies perpendicular to the heme and in hydrogen bonding distance to the histidine ligand to the iron is in fact the site of the tryptophan radical in C*c*P compound I (Sivaraja *et al*, 1989).

Based on sequence alignments and upon solution of the crystal structure of pea ascorbate peroxidase (Patterson and Poulos, 1995), it was immediately assumed that a tryptophanyl radical would be formed on the analogous residue (W179) as in C*c*P. However, despite an identical active site to C*c*P this was not the case (Patterson *et al*, 1995), because the EPR spectrum was not consistent with that of a protein-based radical. It was concluded that ascorbate peroxidase forms a stable compound I porprhyrin π-cation radical even though it has a tryptophan residue (W179) positioned precisely where tryptophanyl radical (W191) is located in cytochrome *c* peroxidase (Patterson *et al*, 1995).

In 1992, a crystal structure of the complex between the electron transfer partners, cytochrome *c* peroxidase and cytochrome *c* was solved at 2.3 Å. It revealed a possible electron transfer pathway between C*c*P and its redox partner (Pelletier and Kraut, 1992). Cytochrome *c* was shown to bind on the surface, proximal to the heme, with a direct path from the surface to the known radical site of Trp191 for electrons to travel (Pelletier and Kraut, 1992). This structure, for the first time linked a radical site with substrate specificity. Although, effectively able to oxidize ascorbate, APX has never shown any affinity for cytochrome *c* (Dunford, 1999). This observation now makes some sense: with the radical staying on the porphyrin ring there would be no direct transfer pathway available for electrons to transfer to cytochrome *c* in APX. Finally, in 2003 the crystal structure of a complex between soybean APX and ascorbate was solved further cementing the link between radical site and peroxidase substrate (Sharp *et al*, 2003). Ascorbate was shown to replace 5 ordered water molecules directly and hydrogen bond to the side chain of Arg172 and the heme propionate (Sharp *et al*, 2003). Again, as in C*c*P, the APX binding site for its peroxidase substrate is directly linked to a radical site, the porphyrin providing an easy route for electrons to travel.

With the C*c*P-cytochrome *c* and APX-ascorbate complex it is possible to rationalize the different substrate binding specificities and account for their different catalytic properties. In C*c*P an insertion of 8 amino acids blocks the ascorbate binding site in APX providing an explanation for why C*c*P has never shown any affinity for ascorbate. Although the precise reason why a tryptophanyl

radical is not detected in compound I of APX is not known, the APX-ascorbate complex shows direct coupling of ascorbate to the heme porphyrin ring completely bypassing any need for a tryptophanyl radical at Trp179.

1.5. Catalase-peroxidases (KatGs)

Unlike monofunctional catalases, which have been extensively studied for over 100 years, catalase-peroxidases (also called KatGs after the encoding gene *katG*) were first characterized in *E. coli* in 1979 (Claiborne and Fridovich, 1979) and subsequently first sequenced in 1988 (Triggs-Raine *et al*, 1988). As their name implies these enzymes are capable of both catalase and peroxidase activity. In 1992, catalase-peroxidases gained significant notoriety when it was confirmed that mutations in the *katG* gene in *Mycobacterium tuberculosis* (MtKatG) were responsible for resistance to the front-line antitubercular drug isoniazid (INH) (Zhang *et al*, 1992). To date there are over 300 sequences and 4 crystal structures available.

1.5.1. Distribution and phylogeny

Currently there are over 300 sequences of *katG* genes (Zámocky *et al*, 2008a) and unlike monofunctional catalases, they cannot be subgrouped. The catalase-peroxidase genes are mainly restricted to bacteria, but there are a few fungal and other eukaryotic examples (Passardi e*t al*, 2007b). Interestingly, the *katG* gene is distributed in roughly 40 % of the bacterial genomes and even closely related species differ in the origin of their *katG* gene or do not contain any *katG* genes (Zámocky *et al*, 2008a) suggesting that KatGs may have an important, but not essential function for bacterial viability. Overall, phylogenetic

relationships among *katG* genes seem to be rather chaotic (Passardi *et al*, 2007b, and Zámocky *et al*, 2008a). Also, there are 2 distinct evolutionary lines of *katG* genes in eukaryotes: one in algae and one in fungi (Zámocky *et al*, 2008a), with both arising from a lateral gene transfer from bacteria living in close relation.

Originally, it appeared that *katG* genes arose in Archaebacteria and were laterally transferred into pathogenic Proteobacteria (Faguy and Dolittle, 2000). However, an analysis of a larger number of gene sequences suggests that KatGs evolved much later than monofunctional heme-containing catalases and sometime after a lateral gene transfer from bacteria to the eukaryotic ancestor (Klotz and Loewen, 2003) and may be the precursor of cytochrome *c* peroxidase and ascorbate peroxidase. However, an alternate view is that KatGs along with C*c*P and APX arose from an ancestral nonduplicated peroxidase from ancestral bacteria (Passardi *et al*, 2007).

1.5.2. General structure and biochemical properties

Catalase-peroxidases show high sequence similarity to the monofunctional plant peroxidase (Welinder, 1992), not to any typical monofunctional catalase. They belong to Class I of the plant-fungal-bacterial peroxidase superfamily, together with cytochrome *c* peroxidase and ascorbate peroxidase (Zámocky *et al*, 2000), and are the only member of the group to possess high catalase activity. Also, KatGs exhibit unique pH dependence with the maximum catalase activity seen between pH 6.5 and 7.0 and the maxiumum peroxidase activity seen between pH 4.5 and 5.0 (Singh *et al*, 2008). Similar to monofunctional catalases, KatGs do not follow typical Michaelis-Menten kinetics. Additionally, catalase turnover

rates ranging from 4,900 sec^{-1} to 15,900 sec^{-1} have been reported (Singh *et al*, 2008), much lower then even the slowest monofunctional catalase. Similarly, the K_M value for hydrogen peroxide in the catalase reaction between 3 mM and 5 mM are also much lower. Although the actual *in vivo* peroxidase substrate of KatGs is unknown, activities ranging from 8 sec^{-1} to 25 sec^{-1} with various artificial peroxidase substrates have been reported (Singh *et al*, 2008) with K_M values ranging between 60 μM to 1000 μM for hydrogen peroxide and 10 μM to 300 μM for the peroxidase substrate (Singh *et al*, 2008).

KatGs are typically found as dimers (~80 kDa per subunit) (Fig. 1.3). Because the subunits of KatGs are roughly twice as large as other members of the family and both the N- and C-terminal domains show sequence similarity to the monomeric peroxidases, it has been proposed that they arose from a gene duplication and fusion event (Welinder, 1991), as each half is similar to the eukaryotic, monomeric peroxidase. Of the 2 sequence related domains, only the N-terminal domain contains a non-covalently bound heme b. Despite its similarity to the N-terminal region, the C-terminal domain has less sequence similarity with the plant peroxidases, does not bind heme, and does not contain the well conserved active site (Carpena *et al*, 2004). Although the precise role of the C-terminal region is not known, it is speculated to assist in protein folding and stability, dimerization, and solubility (Baker *et al*, 2004 and 2006, and Zámocky *et al*, 2008a).

There are currently 4 KatG crystal structures available: *Burkholderia pseudomallei* (BpKatG) (Carpena *et al*, 2003b), *Synechococcus* PCC7942 (Wada

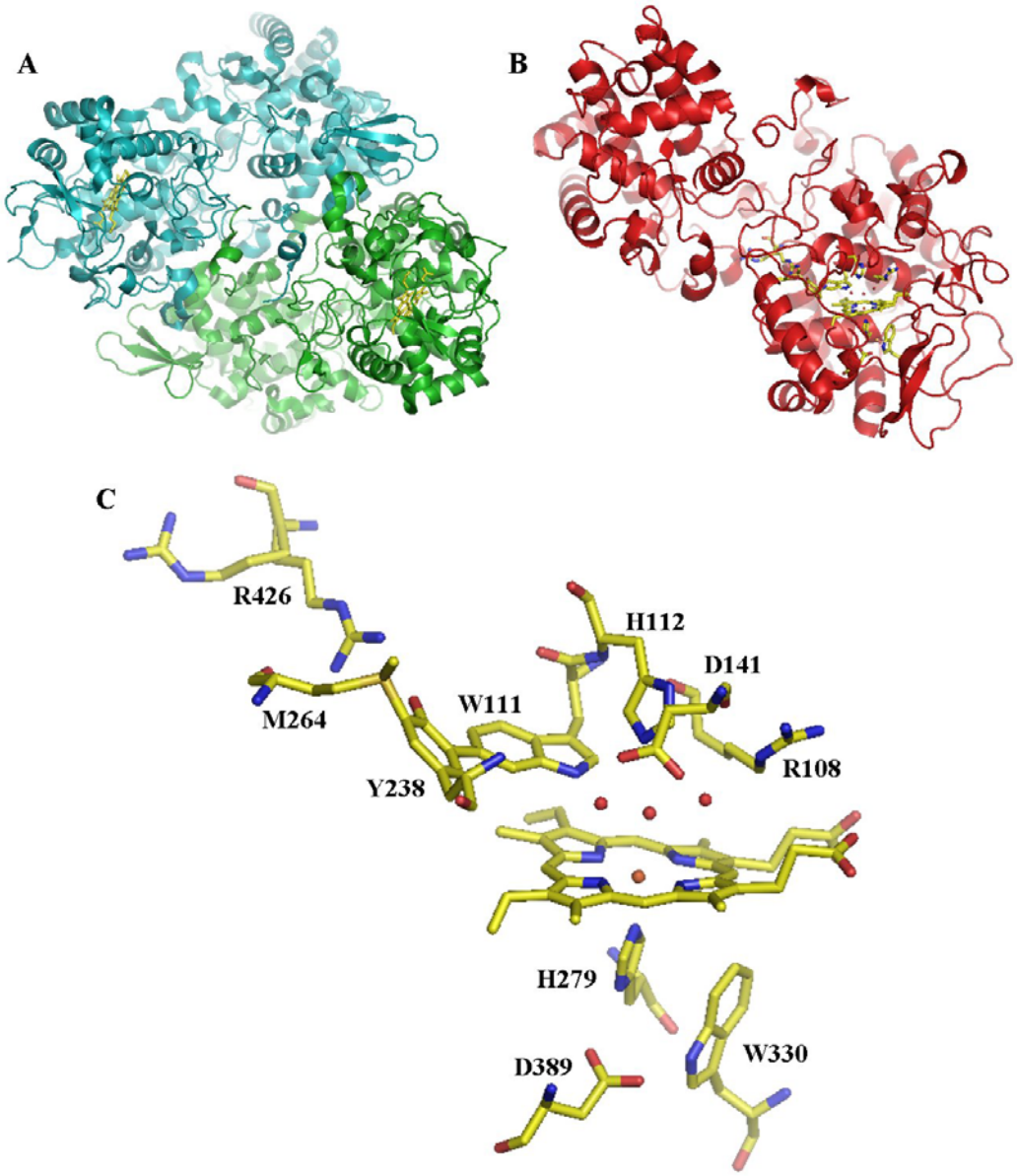

Figure 1.3. Crystal structure of the catalase-peroxidase from *Burkholderia pseudomallei*. Panel A: 2 subunits in relation to each other. Panel B: a single subunit. Panel C: the catalytically important residues in the heme active site. This figure was prepared with coordinates submitted to the protein data bank (PDB id: 1MWV).

et al, 2002), *Haloarcula marismortui* (HmKatG) (Yamada *et al*, 2002), and *Mycobacterium tuberculosis* (MtKatG) (Bertrand *et al*, 2004) which confirm an active site and overall topology similar to other members of the class I plant peroxidase family (Fig. 1.3 and 1.4). Catalase-peroxidases are largely alpha-helical proteins with 2 sequence and structurally related globular domains within each of the 2 identical subunits, and a deeply buried heme active site accessed by 2 channels. One truly unique feature of catalase-peroxidases is a covalent cross-link between the side chains of Trp111, Tyr238, and Met264 (BpKatG numbering) first reported in the crystal structure from the *Haloarcula marismortui* KatG (Yamada *et al*, 2002), and subsequently seen in all other reported KatG crystal structures. This feature was later confirmed in solution by mass spectrometry (Donald *et al*, 2003, Jakopitsch *et al*, 2003, and Ghiladi *et al*, 2005a).

1.5.3. The heme active site

The structures of KatG, including the similarity in overall topology to APX and C*c*P and the virtually identical active sites, clearly confirm the inclusion of KatGs in the class I plant peroxidase group (Fig. 1.4). The distinguishing features of this class of peroxidase, which are also present in KatGs including the active site arginine-histidine-tryptophan triad on the distal side of the heme and the histidine-tryptophan-aspartate triad on the proximal side of the heme. A superposition of C*c*P onto the N-terminal half of HmKatG revealed less than 2.5 Å deviation of all equivalent alpha carbons, and only 0.27 Å deviation in the alpha carbons of the active site residues (Yamada *et al*, 2002).

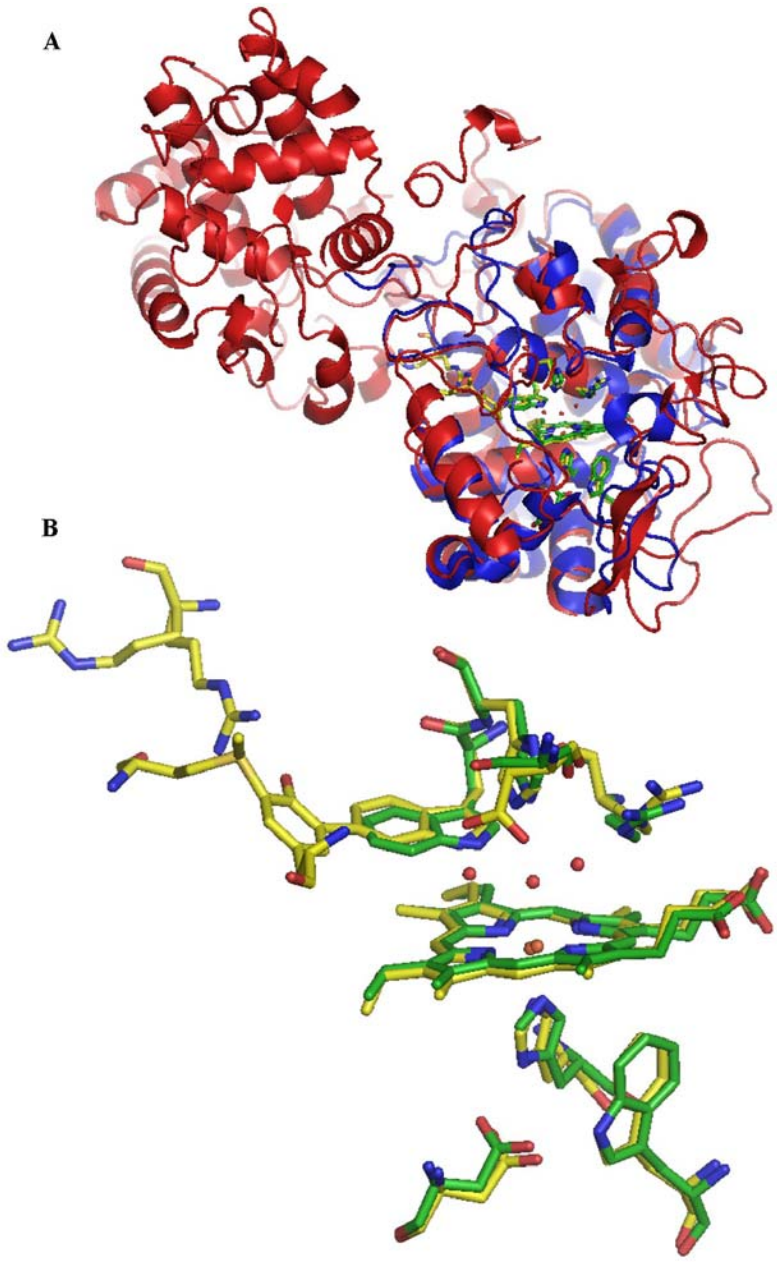

Figure 1.4. Structural alignment of yeast cytochrome *c* peroxidase with the catalase-peroxidase from *Burkholderia pseudomallei*. Panel A: ribbon diagram of both subunits overlayed, cytochrome *c* peroxidase is in blue and the catalase-peroxidase in red. Panel B: an overlay of the catalytically important residues in the heme active site, cytochrome *c* peroxidase is in green and the catalase-peroxidase is in yellow. This figure was prepared with coordinates submitted to the protein data bank (PDB id: 1CCP and 1MWV).

The heme active site in KatG is more deeply buried than in C*c*P and APX because of the larger subunit size and it is accessed through a funnel shaped channel. Similarity to the main access channel of monofunctional catalases is evident in the narrowest constriction being close to the active site heme cavity near Ser324 and Asp141 (Carpena *et al*, 2003b). Asp141 and its equivalent in other KatGs is located in the entrance to the channel, 7.8 Å from the heme iron and is hydrogen bonded to a large KatG specific loop. Asp141 is absent in plant peroxidases. By contrast, the heme-containing active site in plant peroxidases is more accessible through a shorter channel with no restrictions to entry.

As mentioned above, the first step common to both the catalase and peroxidase reactions is the reduction of hydrogen peroxide to water, and generation of an oxoferryl species known as compound I. The same mechanism described for compound I formation in peroxidases involving the distal side histidine acting as a proton acceptor and the distal side arginine acting as a charge stabilizer has been confirmed in catalase-peroxidases as well (Hillar *et al*, 2000, and Reselsberger *et al*, 2000). Interestingly, in the process of confirming compound I formation in KatGs, mutations to the distal side tryptophan completely abolished catalase activity with little to no affect on peroxidase activity (Hillar *et al*, 2000, and Reselsberger *et al*, 2000). Unknown at the time was that this tryptophan belonged to the unusual KatG-specific covalent adduct.

Interestingly, removal of the conserved active site aspartate (D141 in BpKatG) located at the entrance to the heme active site reduced catalase activity to roughly 5 % of wild-type enzyme levels with only a moderate decrease in

peroxidase activity (roughly 60 % of wild-type enzyme levels) (Deemagarn *et al*, 2007). Also, removal of the active site arginine (R108 in BpKatG) and histidine (H112 in BpKatG) has the analogous affect of removing those residues on plant peroxidase with a reduction to about 30 % and 1 % of wild-type enzyme levels, respectively (Singh *et al*, 2004). This observation again confirms that the same mechanism of compound I formation is employed for both KatGs and monofunctional peroxidases.

It has been suggested that Asp141 plays a direct role in hydrogen peroxide deprotonation during the compound I reduction step of the catalase reaction (Jakopitsch *et al*, 2003c). However, removing both Asp141 and Arg108 together restored catalase activity to roughly 80 % of wild-type enzyme levels (Deemagarn *et al*, 2007) suggesting that Asp141 does not have a direct role in hydrogen peroxide deprotonation. It has also been suggested that Asp141 creates an electrical potential field with the heme to act upon the electrical dipoles of the incoming substrate (Jakopitsch *et al*, 2005) in a similar manner to what is seen in monofunctional catalases (Chelikani *et al*, 2003). However, the orientation of the aspartate and overall geometry of the active site is quite different in KatGs compared to monofunctional catalases making this unlikely (Deemagarn *et al*, 2007). A more likely role for this residue is that it promotes catalase activity in the presence of Arg108 by creating a binding site for the incoming hydrogen peroxide that competes with the normal His112-Arg108 site seen in typical monofunctional peroxidases (Deemagarn *et al*, 2007). This competition reduces affinity at the His112-Arg108 site and directs the hydrogen peroxide to the

Trp111-His112 site promoting compound I reduction (Deemagarn *et al*, 2007). Basically Asp141 creates a fork at the entrance to the active site directing the incoming substrate into 2 paths; one path leading to the normal Arg108-His112 binding site, and the other to the Trp111-His112 binding site.

1.5.4. The Trp-Tyr-Met covalent cross-link

Successful crystallization of the catalase-peroxidase from *Haloarcula marismortui* revealed an unusual covalent cross-link joining the side chains of the active site Trp111, Tyr238, and Met264 (BpKatG numbering) that has subsequently been seen in all KatG crystal structures to date. This was later confirmed to be present in solution by mass spectrometry (Donald *et al*, 2003, Jakopitsch *et al*, 2003b, and Ghiladi *et al*, 2005a) strongly suggesting this structure is a common feature to all KatGs. This linkage involves the indole ring of the active site Trp111 and the sulfur of Met264 joined to the ortho positions of Tyr238 (Donald *et al*, 2003).

Prior to a KatG crystal structure, targets for site directed mutagenesis had to rely on the structures of ascorbate and cytochrome *c* peroxidase. Thus it was not known at the time that mutagenesis to the conserved active site tryptophan (W111 in BpKatG) was actually disrupting this covalent cross-link. Replacement of this residue in the KatGs from *E. coli* (HPI) (Hillar *et al*, 2000) and the cyanobacteria *Synechocystis* (SynKatG) (Regelsberger *et al*, 2000) results in a complete loss of catalase activity (less than 0.1 % activity compared to wild-type enzyme levels) with no affect or even an enhancement to peroxidase activity. Subsequently, disruption of this cross-link by the replacement of the tyrosine and

methionine residues (Jakospitch *et al*, 2003a and 2004, Singh *et al*, 2004, Ghiladi *et al*, 2005a, 2005b and 2005c) involved in the cross-link was found to have a similar effect to completely abolishing catalase activity without affecting peroxidase activity. Interestingly, mutagenesis of a nearby arginine (R426 of BpKatG) (Jakospitch *et al*, 2004, and Ghiladi *et al*, 2005c) that is associated with the cross-linked tyrosine reduced catalase activity to 10 % of native levels with little effect on the peroxidase reaction even though a completely formed cross-link is still present. Also surprisingly, removal of the methionine resulted in a completely catalase-inactive enzyme despite the tyrosine-tryptophan portion of the cross-link still being formed (Jakospitch *et al*, 2003b) suggesting that a complete cross-link is required for catalase activity. Thus disruptions to this cross-link in anyway, or removal of Arg426 has the dramatic effect of completely abolishing catalase activity, effectively converting the KatG into a monofunctional peroxidase.

The fact that these highly conserved residues in KatGs, in particular Asp141, Tyr238, Met264 and Arg426, are rarely found in any plant peroxidases, and certainly never found as a group in any one peroxidase, provides a strong hint as to why they have little or no catalase activity. In both C*c*P and APX the tyrosine is replaced by a proline (Pipirou *et al*, 2007) and the methionine is replace by a leucine in yeast C*c*P, but interestingly remains a methionine in APX. It appears that this region is highly reactive, even in peroxidases, as there have been recent reports of peroxide dependent covalent cross-links between the heme and tryptophan in C*c*P and APX (Pipirou *et al*, 2007 and 2009) and even a

tryptophan-tyrosine cross-link in a mutant of C*c*P (Bhaskar *et al*, 2003). Also, the orginal crystal structure of BpKatG (Carpena *et al*, 2003) showed an unusual perhydroxy modification on the vinyl group of ring I of the heme close to cross-linked tryptophan (W111 in BpKatG) and later a similar perhyroxy modification on Trp111 in the structure of the S234T variant of BpKatG (Deemagarn *et al*, 2004). It would be interesting to determine if the conversion of the proline in ascorbate peroxidase back to a tyrosine would give rise to an analogous Met-Tyr-Trp cross-link and whether this would potentially give rise to some catalase activity.

It has been demonstrated that formation of the Met-Tyr-Trp cross-link is an autocatalytic process that requires the formation of compound I (Ghiladi *et al*, 2005a). Interestingly, removal of the methionine still allows the formation of the Tyr-Trp portion of the cross-link (Ghiladi *et al*, 2005b, and Jakopitsch *et al*, 2003) suggesting that the Tyr-Trp portion forms first followed by the Met-Tyr portion. The hypothesis is that compound I formation leads to subsequent oxidation of the nearby tryptophan and tyrosine residues to produce radical species that couple to form the Tyr-Trp crosslink. The methionine portion of the cross-link forms by a second compound I oxidation of the Tyr-Trp linkage leading to a nucleophilic attack of the sulfur atom in the methionine ultimately forming the complete Met-Tyr-Trp cross-link (Ghiladi *et al*, 2005a and 2005b).

1.5.5. Radical sites in KatGs

Similar to monofunctional catalases and peroxidases, KatGs are capable of generating the reactive intermediate compound I, upon reaction with hydrogen

peroxide, which can then go on to react with various peroxidase substrates or in the case of catalases a second molecule of hydrogen peroxide. Compound I is generated in the 2-electron oxidation of the enzyme by hydrogen peroxide that generates an oxoferryl moiety and the concomitant formation of a porphyrin π-cation radical (Ivancich *et al*, 2003) or a protein radical. As described above, ascorbate and horseradish peroxidase, and most monofunctional catalases, form only the porphyrin π-cation radical. However, in the case of cytochrome *c* peroxidase a tryptophanyl radical located near the heme prosthetic group on the proximal tryptophan (W191) was identified (Sivaraja *et al*, 1989), and in the case of lignin peroxidase a tryptophanyl radical located near the surface (W171) was identified (Sollewijn Gelpke *et al*, 2002). In all cases, location of the radical is directly related to subsequent substrate oxidation. For example, in the cases of ascorbate and horseradish peroxidase their peroxidase substrate binds near the heme prothetic group allowing direct coupling with the porphyrin π-cation radical bypassing the need for any protein based radicals. Similarly, cytochrome *c* and lignin peroxidase substrate binding sites are located on the surface requiring intramolecular electron transfer to the appropriate residue within the protein. Unfortunately, in catalase-peroxidases this process appears more complex as typical KatGs have 22-25 tryptophans, compared to only 7 in C*c*P (Colin *et al*, 2009).

A detailed EPR study involving site-directed mutagenesis and isotopic labeling of tryptophan and tyrosine residues was performed on the catalase-peroxidase from the cyanobacteria *Synechocystis* PCC6803 (SynKatG) (Ivancich

et al, 2003) revealing 2 distinct protein based radicals in the form of a tyrosyl and a tryptophanyl-exchanged coupled radical and a short lived porphyrin π-cation radical. If the tryptophan radical is close enough to the porphyrin there is a "sharing" or "exchange" of the radical making the protein radical "exchange coupled" to the porphyrin, a property observable in the EPR signal of the protein radical (Colin *et al*, 2009). There is also evidence for a second tryptophanyl radical that is not exchanged coupled with the oxoferryl moiety (Singh *et al*, 2007) bringing the total to at least 3 distinct protein radicals detected by EPR in catalase-peroxidases. It was concluded that the tryptophanyl-exchange coupled radical resides on Trp106 of SynKatG, a residue belonging to a short conserved stretch in catalase-peroxidases and located 7 to 8 Å from the heme propionate groups (Ivancich *et al*, 2003) and a short distance from the surface analogous to lignin peroxidase. A similar study on MtKatG and BpKatG revealed that the exchange coupled tryptophanyl radical is located on the conserved proximal tryptophan (W341 and W330 respectively) instead (Singh *et al*, 2007, and Colin *et al*, 2009), analogous to cytochrome *c* peroxidase. In all cases where protein radicals are observed, it is the facility of electron transfer from the protein to the porphyrin π-cation radical that gives rise to its short lived nature. In the case of MtKatG and BpKatG, the proximal Trp is exchange coupled to the porphyrin, whereas in SyKatG there is no protein radical close enough to the heme to be exchange coupled, and the porphyrin radical is quenched by electrons from the more distant Tyr106. Alternatively, Tyr353 of MtKatG has been proposed to be the tyrosyl radical site (Zhao *et al*, 2004). This residue is not conserved in other

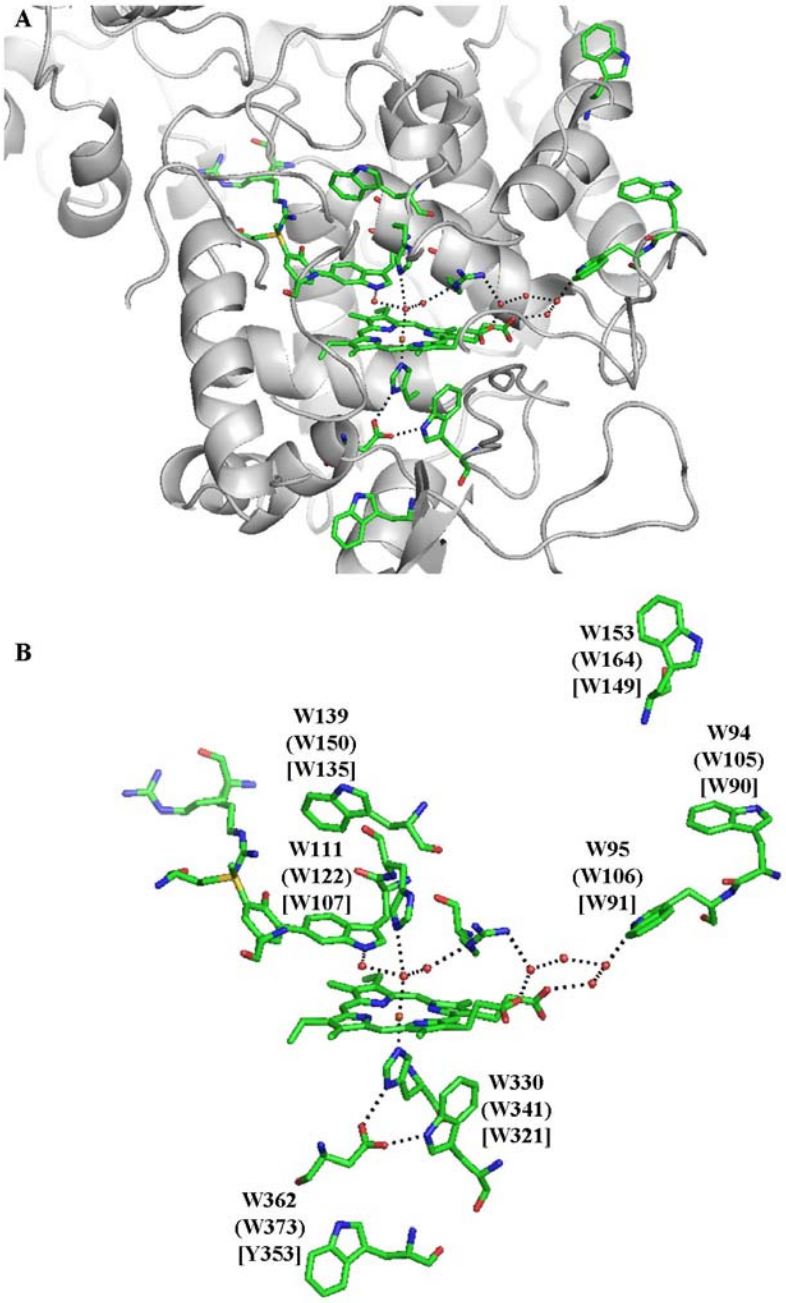

Figure 1.5. Extended heme active site and hydrogen bonding network of the catalase-peroxidase from *Burkholderia pseudomallei*. Panel A: ribbon diagram of the C-terminus. Panel B: heme active site and important tryptophan residues. Amino acid numbering is for BpKatG, but numbering in ( ) and [ ] is for SynKatG and MtKatG respectively. See text for details. This figure was prepared with coordinates submitted to the Protein Data Bank (PDB id. 1MWV).

KatGs (a tryptophan roughly 70 % of the time) and is proximal and some distance from the heme (~15 Å from the heme iron) with no obvious route for electron transfer and thus remains a subject for debate (Singh *et al*, 2007, and Colin *et al*, 2009).

The actual *in vivo* peroxidase substrate in KatGs is unknown. By extension, the substrate binding site is unknown but as in peroxidases there is certainly a link between it and the sites of stable protein radical formation. As shown in Fig. 1.5, the existence of an extensive hydrogen bonding network on the distal side of the heme has been identified as a potential path for electrons to move throughout the protein. A recent EPR study has identified other radical sites away from the heme pocket in BpKatG that depend on the integrity of this hydrogen bonding network (Colin *et al*, 2009). In particular, the formation of a radical at Trp153 of BpKatG, found close to the enzyme surface depends on this network; whereas radical formation at Trp139 depends on the formation of the KatG specific Met-Try-Trp adduct (Colin *et al*, 2009). These additional sites could help explain the occurrence of other oxidizing sites for 1 electron oxidation of substrates (such as INH) elsewhere in the protein.

1.5.6. The catalase-peroxidase from *Mycobacterium tuberculosis*

MtKatG is the only catalase found in *Mycobacterium tuberculosis* (Passardi *et al*, 2007) and it received notoriety when a correlation was observed between isoniazid resistance and loss of catalase and peroxidase activity in *Mycobacterium tuberculosis* (Middlebrook 1952 and 1954, Middlebrook and Cohn, 1953). This enzyme was first purified and characterized in 1974 by Diaz

and Wayne (1974). In 1992, catalase-peroxidases gained world wide attention when it was confirmed that the KatG from *Mycobacterium tuberculosis* is in fact responsible for the activation of the anti-tuberculosis drug isoniazid and that mutations to the *katG* gene lead to INH resistance (Zhang *et al*, 1992). The gene were subsequently cloned and the enzyme characterized by a number of groups (Nagy *et al*, 1997, Johnsson *et al*, 1997, and Saint-Joanis *et al*, 1999). Despite this attention, the crystal structure of MtKatG was not reported until 2004 (Bertrand *et al*, 2004), just after structures from *Burkholderia pseudomallei* (BpKatG) (Carpena *et al*, 2003b), *Synechococcus* PCC 7942 (Wada *et al*, 2002), and *Haloarcula marismortui* (HmKatG) (Yamada *et al*, 2002) appeared.

1.5.6.1. The mode of action of isoniazid

Isoniazid, consisting of a pyridine ring with a carbonylhydrazide group located para to the ring nitrogen was first chemically synthesized from ethyl isonicotinate and hydrate in 1912 (Meyer and Malley, 1912), but its antituberculosis activity was not discovered for another 40 years (Fox *et al*, 1952, and Offe *et al*, 1952). Wide spread use of INH soon followed as the drug proved to by highly superior to any other antituberculosis drugs (Robitzek and Elikoff, 1952). Since then INH has proven to be inexpensive to manufacture and relatively nontoxic and has become (and remains so even after 50 years) the main front-line drug used to combat tuberculosis (Vilchèze and Jacobs, 2007).

Despite INH's widespread use, its mode of action is still not completely understood, but it is known to be a prodrug requiring activation by KatG (Zhang *et al*, 1992) to become fully functional as an antituberculosis agent. Early studies

on the toxic effect of INH on *M. tuberculosis* showed that mycolic acid biosynthesis, required for cell wall synthesis, was inhibited, preventing cell growth (Winder and Collins, 1970). Over 20 years later this effect was attributed to at least 2 enzymes, the NADH-dependent enoyl-ACP reductase known as InhA (Banerjee *et al*, 1994) and the β-ketoacyl-ACP synthase known as KasA (Mdluli *et al*, 1998), both of which are potential targets of the activated form of INH.

InhA is an important enzyme in the biosynthesis of long-chain fatty acids, including mycolic acid, a specific component of the mycobacterial cell wall, and further studies have suggested it is the primary target of INH (Dessen *et al*, 1995, and Rozwarski *et al*, 1998). Crystallographic studies have revealed an isonicotinoyl-NAD (IN-NAD) adduct bound to the active site of InhA. The IN-NAD adduct binds in the same site as the enzyme's cofactor NADH, effectively acting as a competitive inhibitor, thereby inhibiting mycolic acid biosynthesis (Nguyen *et al*, 2001, and Lei *et al*, 2000). This suggests a mechanism whereby the hydrazine portion of INH is removed; likely generating an isonicotinoyl radical that then reacts with NAD^+/NADH to form the final antituberculosis agent. Structures of INH, some of its chemical analogs, and the isonicotinoyl radical, as well as the IN-NAD adduct are shown in Fig. 1.6.

1.5.6.2. The role of KatGs in isoniazid activation

A vast number of studies have focussed on the cleavage of INH catalyzed by KatG but no clear explanation has emerged as to how KatGs accomplish this. It has been suggested that INH is somehow activated through the peroxidatic reaction of KatGs (Magliozzo and Marcinkeviciene, 1997) and that it reacts with

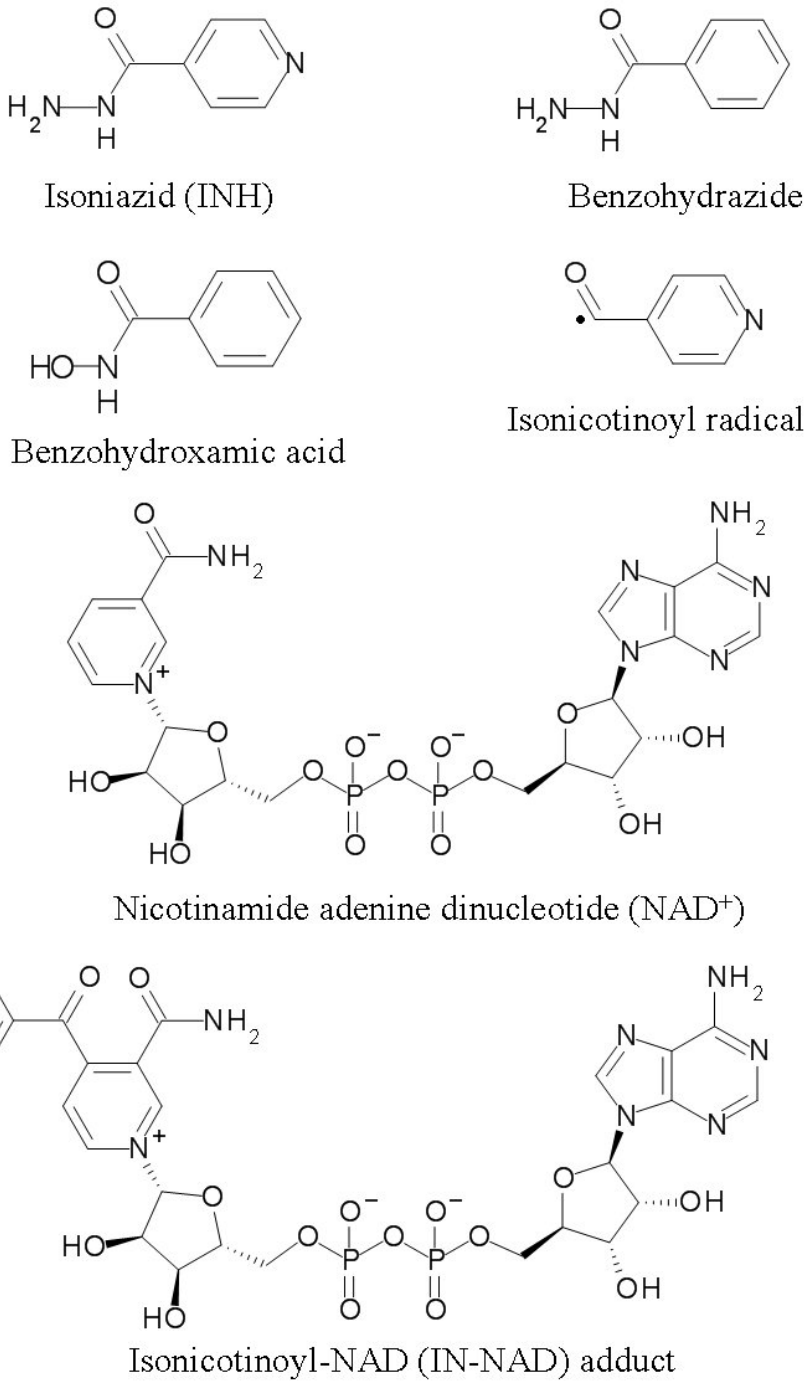

Figure 1.6. Chemical structures of isoniazid, NAD^+ and related compounds. This figure was prepared using Symyx Draw 3.2 (www.symyx.com).

enzyme intermediates in the peroxidase cycle (Ghiladi *et al*, 2005c). Also, a recent EPR study suggested that INH reacts with one of the protein radicals, probably the non-exchanged coupled tryptophanyl radical. This radical was not detected when KatG was incubated with INH suggesting it is being consumed during INH activation (Singh *et al*, 2007). Isoniazid can also be converted to IN-NAD nonenzymatically, in a mixture of INH, NADH or NAD^+ and Mn ion alone (Zabinski and Blanchard, 1997, Wei *et al*, 2003, and Singh *et al*, 2004).

When NAD^+ was included in a reaction mixture with INH and no oxidant other than molecular oxygen, an IN-NAD species was generated even in the absence of KatG. This led to the suggestion that the role of KatG is limited to the cleavage of INH and the subsequent coupling to NAD^+ is a nonenzymatic event involving a homolytic aromatic substitution reaction (Lei *et al*, 2000). Singh and coworkers have shown however, that KatG does significantly increase the production of both the isonicotinyl radical and the IN-NAD adduct (Singh *et al*, 2004). Moreover, these authors note that KatGs are capable of binding NAD^+/NADH and actually possess a low level of NADH oxidase activity that is inhibited by NAD^+. The tentative conclusion was that KatGs do play a direct role in enhancing the rate of production of IN-NAD which is why the enzyme is required for INH activation *in vivo*.

Thus, the current model of INH action is as follows: once INH diffuses into the *M. tuberculosis* cell (Bardou *et al*, 1998) it is first 'activated' by the removal of the hydrazine group, catalyzed by KatG, leading to the formation of an isonicotinoyl radical that couples with NAD^+ to yield the final IN-NAD adduct

(Vilchèze and Jacobs, 2007). The resulting IN-NAD adduct is a potent inhibitor of InhA by competitively binding to the active site and preventing NADH binding. This inhibition prevents the accumulation of long chain fatty acids leading to an inhibition of mycolic acid biosynthesis which in turn inhibits cell growth (Vilchèze and Jacobs, 2007).

1.5.6.3. The mechanism of isoniazid resistance

Almost immediately after the discovery of the antituberculosis activity of INH, resistant strains began to be isolated (Pansy *et al*, 1952). Interestingly, many of these strains were found to be catalase-negative (Middlebrook, 1954). It has become evident over the years that resistance to INH in *M. tuberculosis* clinical isolates is most commonly associated with mutations to the *katG* gene with so far, at least 130 mutations in *katG* having been reported (Vilchèze and Jacobs, 2007). Mainly point mutations have been reported, but missence and nonsence mutations (Heym *et al*, 1995), insertions, deletions, truncation and more rarely full gene deletions have also been reported (Zhang *et al*, 1992, Heym and Cole, 1992, and Ramaswamy *et al*, 2003). All of these mutations have varying effects on the catalase-peroxidase activity.

Of the catalogued 130 mutations in *katG*, the point mutation encoding S315T is found in 60 % (Ahmad and Mokaddas, 2004) to 80 % (Silva *et al*, 2003) of all INH resistant clinically isolated strains. This particular mutant is highly deficient in producing the IN-NAD adduct but still retains near normal levels of catalase and peroxidase activities (Ghiladi *et al*, 2004). This is in contrast to other mutations conferring INH resistance such as full gene deletion, or insertions and

deletions, or nonsence muations which also result in the loss of catalase and peroxidase activites. The high prevalence of this mutation is no doubt due to the protective effects of the retained catalase and peroxidase activities against the reactive oxygen species encountered within macrophages, along with the inability to produce the IN-NAD adduct.

Although still under discussion, several studies have proposed that the S315T replacement affects INH activation and binding (Wengenack *et al*, 1997 and 1998, and Yu *et al*, 2003a), and ultimately the production of the IN-NAD adduct (Ghiladi *et al*, 2004). The recent success in crystallization of a few representative KatGs have shown this residue to be located in the main access channel, at its narrowest point, about 14 Å from the heme iron. The side chain of Ser315 (Ser324 in BpKatG) forms a hydrogen bond with the carboxylate group of the heme propionate side-chain (Carpena *et al*, 2003b, and Bertrand *et al*, 2004) and it has been suggested that this interaction could draw electrons away from the serine residue towards the electron-deficient heme of compound I or II (Carpena *et al*, 2003b). Structural determination of the S315T variant of MtKatG (Zhao *et al*, 2006) and the analogous variant S324T of BpKatG (Deemagarn *et al*, 2005) has shown the extra methyl group of the threonine side chain to be pointing directly into the access channel, narrowing the access channel. Accordingly, it has been suggested that this mutation is blocking the access channel, and thus preventing INH binding (Deemagarn *et al*, 2005, and Zhao *et al*, 2006).

Other explanations for the variant's phenotype besides simple lack of INH binding needs to be considered, such as disruption the hydrogen bonding network

that could potentially alter radical locations and the overall electronic environment of the heme and enzymatic intermediates that may mediate INH activation. Currently, the INH binding site(s) in KatGs is not known. A structure of the INH analog benzohydroxamic acid bound to horseradish peroxidase (Henriksen *et al*, 1998) and structures of INH bound to both ascorbate peroxidase and cytochrome *c* peroxidase (Metcalfe *et al*, 2008) show binding near the heme edge in all cases. However, as described above KatGs have a much longer and constricted access channel compared to other peroxidases. In fact the equivalent region of INH binding in C*c*P and AXP and benzohydroxamic binding in horseradish peroxidase are constricted in KatGs making substrate access much more difficult.

Although, not as common as mutations to *katG*, mutations in the *inhA* gene have also been reported. Most of these changes are confined to the NADH binding pocket and hence reduce affinity for the cofactor NADH, causing increased resistane to inhibition (Quémard *et al*, 1995). However, most mutations associated with i*nhA* are not found in the gene itself but are usually found in the promoter region, with one such mutation increasing *inhA* mRNA levels 20 times higher than that seen in the wild-type (Vilchèze *et al*, 2006). Finally, there have also been reports of clinical isolates resistant to INH with mutations in other genes besides *katG* or *inhA* such as: *furA*, *ahpC*, *fadE24*, *kazA*, and efpA (Ramaswamy *et al*, 2003, and Zhang *et al*, 2005). However these mutations were always found in combination with mutations in *katG* and/or the *inhA* promoter region.

1.6. Objective of thesis

Recent high resolution crystal structures of a few representative KatGs confirmed their relation to monofunctional peroxidases and revealed a truly unique Met-Tyr-Trp covalent cross-link located at the heme active site. KatGs are also responsible for the activation of isoniazid as an antitubercular drug in *Mycobacterium tuberculosis* (Zhang *et al*, 1992). However, despite recent success in KatG crystallization, one of the most important unanswered questions is the location of the isoniazid and NADH/NAD^+ binding sites. It is also important to note that because of the overwhelming catalase activity of KatGs, it is necessary to use organic peroxides in place of H_2O_2 to study the reaction intermediates. Thus, the focus of this work is 3-fold: first, to investigate the catalytic and structural role of the unusual Met-Tyr-Trp covalent cross-link and a nearby arginine that is associated with the cross-linked tyrosine; second, to further probe the enzyme's reaction pathway by studying the much slower reaction with peroxyacetic acid on the millisecond time scale; and third, to understand the role of KatGs in the activation of the antitubercular drug isoniazid and the mechanism of isonicotinoyl-NAD synthesis. In this thesis, studies are performed on the KatG from *Burkholderia pseudomallei* (BpKatG) as it exhibits typical properties of a catalase-peroxidase and has proven amenable to crystallization. Our goals are accomplished using the techniques of site-directed mutagenesis, enzyme kinetics, X-ray crystallography, and stopped-flow absorption spectroscopy.

2. MATERIALS AND METHODS

2.1. Biochemical and common reagents

All chemicals, reagents, and antibiotics used in the course of this study were of the highest grade available and purchased from either Fisher Scientific Ltd. (Mississauga, Ontario) or Sigma Chemical Co. (St. Louis, Missouri). Restriction enzymes, T4 DNA ligase, polynucleotide kinase were purchased from Invitrogen Canada Inc. (Burlington, Ontario). Unmodified T7 DNA polymerase was purchased from New England Biolabs Ltd. (Pickering, Ontario). The T7 sequencing kit was purchased from USB Corporation (Cleveland, Ohio). Media components used for growth of *E. coli* cultures were purchased from DIFCO. The following buffers were used: pH 3.0-5.5 50 mM sodium acetate, pH 6.0-7.5 50 mM potassium phosphate, pH 8.0-9.0 50 mM Tris-HCl, and pH 9.5 and above 50 mM CHES. Growth media were prepared using reverse osmosis distilled water; all other solutions were prepared with MilliQ water (Millipore Co., Billerica, Massachusetts).

2.2. *Escherichia coli* strains, plasmids and bacteriophage

The *E.coli* strains, plasmids, and bacteriophage used in this study are listed in Table 2.1. The *Burkholderia pseudomallei katG* gene (Fig. 2.1) was inserted into plasmid pKS- to generate the pBpG plasmid (Carpena *et al*, 2002). The strain CJ236 harboring the various pBpG subclones was used for the generation of uracil-containing, single-stranded DNA needed for site-directed mutagenesis. The helper phage R408 was used to infect CJ236 and generate single-stranded DNA. Strains NM522 and JM109 were routinely used for cloning, and plasmid

Table 2.1. Genotypes and sources of *Escherichia coli* strains, *Burkholderia pseudomallei katG* encoded plasmids and bacteriophage used in this study.

	Genotype	Source
***E. coli* strains**		
CJ236	*dut*1 *ung*1 *thi*-1 *rel*A1/pCJ105/*cam*^{r}F'	Kunkel *et al*, 1987
NM522	*sup*E Δ(*lac-pro*AB) *hsd*-5 [F' *pro*AB *lac*I^{q} *lacZ*Δ15]	Mead *et al*, 1985
JM109	*rec*A1 *sup*E44 *end*A1 *hsd*A1 *had*R17 *gyr*A96 *rel*A1 *thi* Δ(lac-proAB)	Yanisch-Perron *et al*, 1985
UM262	*rec*A *katG*::Tn10 *pro leu rps*L *hsd*M *hsd*R *end*I *lacy*	Loewen *et al*, 1990
Plasmids		
pKS- (pBluescript™)	Amp^{R}	Stratagene Cloning System
pBpG (*B. pseudomallei katG* clone)	Amp^{R}	Deemagarn, T. M.Sc. thesis, 2004
pBpG subclones		
pBpG-KC	Amp^{R}	Deemagarn, T. M.Sc. thesis, 2004
pBpG-CH	Amp^{R}	Singh, R. Ph.D. thesis, 2006
pBpG-HC	Amp^{R}	This study
pBpG-CE	Amp^{R}	This study
pBpG-KH	Amp^{R}	Singh, R. Ph.D. thesis, 2006
pBpG-HE	Amp^{R}	This study
Bacteriophage		
R408 (helper phage)		Stratagene Cloning System

```
GGTACCGTGAGAAGCTCGATATCCCGGCGACGGTGAATTGAGCGCGGCGAGCGCAGCTG    60
CCATGGCACTCTTCGAGCTATAGGGCCGCTGCCACTTAACTCGCGCCGCTCGCGACGAC
KpnI

CGGGCCGCCGCGCGCCATGATCGGACGGGGCTTCGGGGCCCCGTTTATTTTTGCCTATCG  120
GCCCGGCGGCGCGCGGTACTAGCCTGCCCCGAAGCCCCGGGGCAAATAAAAACGGATAGC

GATAAATAAAATTTATTAAATTACATATATCAATAGCAAATAATAGAATGCTTCGCATGG  180
CTATTTATTTTAAATAATTTAATGTATATAGTTATCGTTTATTATCTTACGAAGCGTACC

ATCGGCGCAGCGCCGCCGGACGGTAACTGCAAGCGTCAAGGGAGGATGTCATGATGCAAC  240
TAGCCGCGTCGCGGCGGCCTGCCATTGACGTTCGCAGTTCCCTCCTACAGTACTACGTTG

CGGCATTGTCGCGCGCGCGGCGGAACATTGCGCCGCGCCCGGCGGTCATTGATCGTGCCA  300
GCCGTAACAGCGCGCGCGCCGCCTTGTAACGCGGCGCGGGCCGCCAGTAACTAGCACGGT

AGGCTGCCATCCGGAGCCTGCGTCCGATTGCGTTCGCTTATCTGGCGGACCGCGCCCACG  360
TCCGACGGTAGGCCACGGACGCAGGCTAACGCAAGCGAATAGACCGCCTGGCGCGGGTGC

GCGGCTGAGCGCCGCCGCGTGCCGGGCCGCTTTTTTCGCGCCGCGCGTCGCGTCGCACGC  420
CGCCGACTCGCGGCGGCGCACGGCCCGGCGAAAAAAGCGCGGCGCGCAGCGCAGCGTGCG

                                                      M  P  G  S    (4)
AGGAGGGGTCAACCTGTTTGTTTCCCCGCAAAGTCGCCCCCCGAACGATGCCCGGCTCCG  480
TCCTCCCCAGTTGGACAAACAAAGGGGCGTTTCAGCGGGGGGCTTGCTACGGGCCGAGGC

G  A  G  P  R  R  R  G  V  H  E  Q  R  R  N  R  M  S  N  E   (24)
ATGCCGGGCCCCGCAGGCGGGGCGTACACGAACAAAGGAGAAATCGCATGTCGAATGAAG  540
TACGGCCCGGGGCGTCCGCCCCGCATGTGCTTGTTTCCTCTTTAGCGTACAGCTTACTTC

A  K  C  P  F  H  Q  A  A  G  N  G  T  S  N  R  D  W  W  P   (44)
CGAAGTGCCCGTTCCATCAAGCCGCAGGCAACGGCACGTCGAACCGGGACTGGTGGCCCA  600
GCTTCACGGGCAAGGTAGTTCGGCGTCCGTTGCCGTGCAGCTTGGCCCTGACCACCGGGT

N  Q  L  D  L  S  I  L  H  R  H  S  S  L  S  D  P  M  G  K   (64)
ATCAGCTGGACCTGAGCATCCTGCATCGGCACTCGTCGCTGTCCGATCCGATGGGCAAGG  660
TAGTCGACCTGGACTCGTAGGACGTAGCCGTGAGCAGCGACAGGCTAGGCTACCCGTTCC

D  F  N  Y  A  Q  A  F  E  K  L  D  L  A  A  V  K  R  D  L   (84)
ATTTCAACTACGCGCAGGCGTTCGAGAAGCTCGACCTCGCGGCGGTGAAGCGCGACCTCC  720
TAAAGTTGATGCGCGTCCGCAAGCTCTTCGAGCTGGAGCGCCGCCACTTCGCGCTGGAGG

H  A  L  M  T  T  S  Q  D  W  W  P  A  D  F  G  H  Y  G  G  (104)
ACGCGCTGATGACGACGTCGCAGGACTGGTGGCCGGCCGATTTCGGCCACTACGGCGGCC  780
TGCGCGACTACTGCTGCAGCGTCCTGACCACCGGCCGGCTAAAGCCGGTGATGCCGCCGG

L  F  I  R  M  A  W  H  S  A  G  T  Y  R  T  A  D  G  R  G  (124)
TGTTCATCCGCATGGCATGGCACAGCGCGGGCACGTACCGCACGGCCGACGGCCGCGGCG  840
ACAAGTAGGCGTACCGTACCGTGTCGCGCCCGTGCATGGCGTGCCGGCTGCCGGCGCCGC
        ---------TTT--------->W111F
        ---------CAC--------->W111H
```

Figure 2.1. The DNA and corresponding amino acid sequence of *Burkholderia pseudomallei katG* indicating restriction sites (in italics) and mutagenic primers. The numbers in ( ) refer to amino acid sequence. GenBank Accession: AY040244.

```
G  A  G  E  G  Q  Q  R  F  A  P  L  N  S  W  P  D  N  A  N  (144)
GCGCGGGCGAAGGGCAGCAGCGCTTCGCGCCGCTCAACAGCTGGCCCGACAACGCGAACC  900
CGCGCCCGCTTCCCGTCGTCGCGAAGCGCGGCGAGTTGTCGACCGGGCTGTTGCGCTTGG


L  D  K  A  R  R  L  L  W  P  I  K  Q  K  Y  G  R  A  I  S  (164)
TCGACAAGGCGCGCCGGCTGCTGTGGCCGATCAAGCAGAAGTACGGCCGCGCCATCTCGT  960
AGCTGTTCCGCGCGGCCGACGACACCGGCTAGTTCGTCTTCATGCCGGCGCGGTAGAGCA

W  A  D  L  L  I  L  T  G  N  V  A  L  E  S  M  G  F  K  T  (184)
GGGCCGACCTGCTGATCCTGACGGGCAACGTCGCGCTCGAATCGATGGGCTTCAAGACCT 1020
CCCGGCTGGACGACTAGGACTGCCCGTTGCAGCGCGAGCTTAGCTACCCGAAGTTCTGGA
                                        ClaI

F  G  F  A  G  G  R  A  D  T  W  E  P  E  D  V  Y  W  G  S  (204)
TCGGCTTCGCGGGCGGCCGCGCGGACACGTGGGAAGCCCGAGGACGTCTACTGGGGCTCG 1080
AGCCGAAGCGCCCGCCGGCGCGCCTGTGCACCCTTCGGGCTCCTGCAGATGACCCCGAGC

E  K  I  W  L  E  L  S  G  G  P  N  S  R  Y  S  G  D  R  Q  (224)
GAAAAGATCTGGCTGGAACTGAGCGGCGGCCGAACAGCCGCTATTCGGGCGACCGCCAGC 1140
CTTTTCTAGACCGACCTTGACTCGCCGCCGGCTTGTCGGCGATAAGCCCGCTGGCGGTCG

L  E  N  P  L  A  A  V  Q  M  G  L  I  Y  V  N  P  E  G  P  (244)
TCGAGAACCCGCTCGCCGCCGTGCAGATGGGCCTCATCTACGTGAATCCGGAAGGCCCGG 1200
AGCTCTTGGGCGAGCGGCGGCACGTCTACCCGGAGTAGATGCACTTAGGCCTTCCGGGCC
                           ---------GCC--------->Y238A
                           ---------TTC--------->Y238F

D  G  N  P  D  P  V  A  A  A  R  D  I  R  D  T  F  A  R  M  (264)
ACGGCAATCCCGATCCGGTCGCCGCGGCGCGCGACATTCGTGACACCTTCGCGCGCATGG 1260
TGCCGTTAGGGCTAGGCCAGCGGCGCCGCGCGCTGTAAGCACTGTGGAAGCGCGCGTACC
                                                ---------GCG-
                                                ---------CTG-

A  M  N  D  E  E  T  V  A  L  I  A  G  G  H  T  F  G  K  T  (284)
CGATGAACGACGAAGAGACGGTCGCGCTGATCGCGGGCGGCCACACGTTCGGCAAGACGC 1320
GCTACTTGCTGCTTCTCTGCCAGCGCGACTAGCGCCCGCCGGTGTGCAAGCCGTTCTGCG
--------->M264A
--------->M264L

H  G  A  G  P  A  S  N  V  G  A  E  P  E  A  A  G  I  E  A  (304)
ACGGCGCGGGGCCCGCGTCGAACGTCGGCGCCGAGCCGGAGGCCGCGGGCATCGAAGCGC 1380
TGCCGCGCCCCGGGCGCAGCTTGCAGCCGCGGCTCGGCCTCCGGCGCCCGTAGCTTCGCG

Q  G  L  G  W  K  S  A  Y  R  T  G  K  G  A  D  A  I  T  S  (324)
AGGGCCTCGGCTGGAAGAGCGCGTACCGCACGGGCAAGGGCGCGGACGCGATCACGAGCG 1440
TCCCGGAGCCGACCTTCTCGCGCATGGCGTGCCCGTTCCCGCGCCTGCGCTAGTGCTCGC

G  L  E  V  T  W  T  T  T  P  T  Q  W  S  H  N  F  F  E  N  (344)
GGCTCGAAGTCACGTGGACGACGACGCCGACGCAGTGGAGCCACAACTTCTTCGAGAACC 1500
CCGAGCTTCAGTGCACCTGCTGCTGCGGCTGCGTCACCTCGGTGTTGAAGAAGCTCTTGG
     ---------TTC--------->W330F
```

Figure 2.1. continued.

```
L  F  G  Y  E  W  E  L  T  K  S  P  A  G  A  H  Q  W  V  A  (364)
TGTTCGGCTACGAGTGGGAGCTGACGAAGAGCCCGGCGGGCGCGCACCAGTGGGTCGCGA 1560
ACAAGCCGATGCTCACCCTCGACTGCTTCTCGGGCCGCCCGCGCGTGGTCACCCAGCGCT

K  G  A  D  A  V  I  P  D  A  F  D  P  S  K  K  H  R  P  T  (384)
AGGGCGCCGACGCGGTGATTCCCGACGCGTTCGATCCGTCGAAGAAGCATCGTCCGACGA 1620
TCCCGCGGCTGCGCCACTAAGGGCTGCGCAAGCTAGGCAGCTTCTTCGTAGCAGGCTGCT


M  L  T  T  D  L  S  L  R  F  D  P  A  Y  E  K  I  S  R  R  (404)
TGCTCACGACCGACCTGTCGCTGCGCTTCGATCCGGCGTACGAAAAGATCTCGCGCCGCT 1680
ACGAGTGCTGGCTGGACAGCGACGCGAAGCTAGGCCGCATGCTTTTCTAGAGCGCGGCGA

F  H  E  N  P  E  Q  F  A  D  A  F  A  R  A  W  F  K  L* T  (424)
TCCACGAGAACCCGGAGCAGTTCGCCGACGCGTTCGCGCGCGCCTGGTTCAAGCTTACGC 1740
AGGTGCTCTTGGGCCTCGTCAAGCGGCTGCGCAAGCGCGCGCGGACCAAGTTCGAATGCG
                                                    HindIII
                                                        -------
                                                        -------
                                                        -------
                                                        -------
H  R  D  M  G  P  R  A  R  Y  L  G  P  E  V  P  A  E  V  L  (444)
ACCGCGACATGGGCCCGCGCGCGCGCTATCTCGGCCCGGAAGTGCCGGCCGAGGTGCTGC 1800
TGGCGCTGTACCCGGGCGCGCGCGCGATAGAGCCGGGCCTTCACGGCCGGCTCCACGACG
--AAG--------->R426K
--GCC--------->R426A
--GAG--------->R426E
--CTC--------->R426L

L  W  Q  D  P  I  P  A  V  D  H  P  L  I  D  A  D  A  A  A  (464)
TGTGGCAGGACCCGATTCCGGCCGTCGACCATCCGCTGATCGACGCCGCGGACGCCGCCG 1860
ACACCGTCCTGGGCTAAGGCCGGCAGCTGGTAGGCGACTAGCTGCGGCGCCTGCGGCGGC

E  L  K  A  K  V  L  A  S  G  L  T  V  S  Q  L  V  S  T  A  (484)
AGCTGAAGGCAAAGGTGCTCGCGTCGGGGCTGACCGTGTCGCAGCTCGTTTCCACCGCGT 1920
TCGACTTCCGTTTCCACGAGCGCAGCCCCGACTGGCACAGCGTCGAGCAAAGGTGGCGCA

W  A  A  A  S  T  F  R  G  S  D  K  R  G  G  A  N  G  A  R  (504)
GGGCGGCGGCGTCCACCTTCCGCGGCTCGGACAAGCGCGGCGGCGCGAACGGCGCGCGCA 1980
CCCGCCGCCGCAGGTGGAAGGCGCCGAGCCTGTTCGCGCCGCCGCGCTTGCCGCGCGCGT

I  R  L  A  P  Q  K  D  W  E  A  N  Q  P  E  Q  L  A  A  Y  (524)
TTCGCCTTGCGCCGCAGAAGGACTGGGAGGCGAACCAGCCCGAGCAGCTCGCGGCGGTGC 2040
AAGCGGAACGCGGCGTCTTCCTGACCCTCCGCTTGGTCGGGCTCGTCGAGCGCCGCCACG

L  E  T  L  E  A  I  R  T  A  F  N  G  A  Q  R  G  G  K  Q  (544)
TCGAGACGCTCGAGGCAATTCGCACGGCGTTCAACGGCGCGCAGCGCGGCGGCAAGCAAG 2100
AGCTCTGCGAGCTCCGTTAAGCGTGCCGCAAGTTGCCGCGCGTCGCGCCGCCGTTCGTTC

V  S  L  A  D  L  I  V  L  A  G  C  A  G  V  E  Q  A  A  K  (564)
TGTCGCTCGCCGATCTGATCGTGCTGGCCGGCTGCGCGGGCGTCGAGCAGGCGGCGAAGA 2160
ACAGCGAGCGGCTAGACTAGCACGACCGGCCGACGCGCCCGCAGCTCGTCCGCCGCTTCT
```

Figure 2.1. continued.

```
N  A  G  H  A  V  T  V  P  F  A  P  G  R  A  D  A  S  Q  E  (584)
ACGCGGGCCACGCGGTGACCGTGCCGTTCGCGCCGGGCCGCGCGGACGCATCGCAGGAGC 2220
TGCGCCCGGTGCGCCACTGGCACGGCAAGCGCGGCCCGGCGCGCCTGCGTAGCGTCCTCG

Q  T  D  V  E  S  M  A  V  L  E  P  V  A  D  G  F  R  N  Y  (604)
AGACCGACGTCGAATCGATGGCCGTGCTCGAGCCGGTGGCCGACGGTTTTCGCAACTACC 2280
TCTGGCTGCAGCTTAGCTACCGGCACGAGCTCGGCCACCGGCTGCCAAAAGCGTTGATGG
             ClaI

L  K  G  K  Y  R  V  P  A  E  V  L  L  V  D  K  A  Q  L  L  (624)
TGAAGGGCAAGTATCGGGTGCCCGCCGAGGTGCTGCTCGTCGACAAGGCGCAACTGCTGA 2340
ACTTCCCGTTCATAGCCCACGGGCGGCTCCACGACGAGCAGCTGTTCCGCGTTGACGACT

T  L  S  A  P  E  M  T  V  L  L  G  G  L  R  V  L  G  A  N  (644)
CGCTGAGCGCGCCGGAGATGACGGTGCTGCTGGGCGGCCTGCGCGTGCTGGGCGCGAACG 2400
GCGACTCGCGCGGCCTCTACTGCCACGACGACCCGCCGGACGCGCACGACCCGCGCTTGC

V  G  Q  S  R  H  G  V  F  T  A  R  E  Q  A  L  T  N  D  F  (664)
TCGGGCAGAGCCGGCACGGCGTGTTCACCGCGCGCGAGCAGGCATTGACCAACGACTTCT 2460
AGCCCGTCTCGGCCGTGCCGCACAAGTGGCGCGCGCTCGTCCGTAACTGGTTGCTGAAGA

F  V  N  L  L  D  M  G  T  E  W  K  P  T  A  A  D  A  D  V  (684)
TCGTGAACCTGCTCGACATGGGCACCGAGTGGAAGCCGACGGCGGCCGACGCGGACGTGT 2520
AGCACTTGGACGAGCTGTACCCGTGGCTCACCTTCGGCTGCCGCCGGCTGCGCCTGCACA

F  E  G  R  D  R  A  T  G  E  L  K  W  T  G  T  R  V  D  L  (704)
TCGAAGGGCGCGACCGCGCGACGGGCGAGCTCAAGTGGACGGGCACGCGCGTCGATCTCG 2580
AGCTTCCCGCGCTGGCGCGCTGCCCGCTCGAGTTCACCTGCCCGTGCGCGCAGCTAGAGC

V  F  G  S  H  S  Q  L  R  A  L  A  E  V  Y  G  S  A  D  A  (724)
TGTTCGGCTCGCACTCGCAGTTGCGCGCGCTCGCGGAGGTCTACGGCAGCGCGGACGCGC 2640
ACAAGCCGAGCGTGAGCGTCAACGCGCGCGAGCGCCTCCAGATGCCGTCGCGCCTGCGCG

Q  E  K  F  V  R  D  F  V  A  V  W  N  K  V  M  N  L  D  R  (744)
AGGAGAAGTTCGTGCGCGACTTCGTCGCGGTCTGGAACAAGGTGATGAACCTCGACCGCT 2700
TCCTCTTCAAGCACGCGCTGAAGCAGCGCCAGACCTTGTTCCACTACTTGGAGCTGGCGA

F  D  L  A  *                                                  (748)
TCGATCTCGCGTGATCGCGCCGCCGCGCCGCCGGAGCGGCGGCGCGCGGCGGCGGGGAAC 2760
AGCTAGAGCGCACTAGCGCGGCGGCGCGGCGGCCTCGCCGCCGCGCGCCGCCGCCCCTTG

GGCCGGCTGACGCGGGCCGCTTCCCGCCGGGCCGCTGATATCGTTTCAAGGAGTGACGAT 2820
CCGGCCGACTGCGCCCGGCGAAGGGCGGCCCGGCGACTATAGCAAAGTTCCTCACTGCTA

CATGACGCAAATGATTCTCGACCTGCGCGGGGCGCTCGCGGCGCCGGCCAGGCGCGCGGG 2880
GTACTGCGTTTACTAAGAGCTGGACGCGCCCCGCGAGCGCCGCGGCCGGTCCGCGCGCCC

CGCCGCGGCGTGGCGGCGGCTGATCGGCCTCGCGATCGCGGGCGGCGGCGCGGCCGTGCT 2940
GCGGCGCCGCACCGCCGCCGACTAGCCGGAGCGCTAGCGCCCGCCGCCGCGCCGGCACGA

GGCCGCGCAGGCCGCGCGCTACTTCACGGCGGCCGCCGGCGGTTGAGCGGGCCTGCGTTT 3000
CCGGCGCGTCCGGCGCGCGATGAAGTGCCGCCGGCGGCCGCCAACTCGCCCGGACGCAAA
```

Figure 2.1. continued.

```
CGCGCAAATCGCGCGCTCGCGATCTACGCTAAACTGGTGCGGCGCTCGGCGGGCAGCCGC 3060
GCGCGTTTAGCGCGCGAGCGCTAGATGCGATTTGACCACGCCGCGAGCCGCCCGTCGGCG

ACGCGCGTCTGCCGCCTCTGCATAGGCTGCCCATGCGCATGTCGCCTGCGCGCATCCCGC 3120
TGCGCGCAGACGGCGGAGACGTATCCGACGGGTACGCGTACAGCGGACGCGCGTAGGGCG

ATCGGGCATGCGGATCTTTCGATGCATTTTCGTCGGTTCGAACCATCGGACAAGGAGTTT 3180
TAGCCCGTACGCCTAGAAAGCTACGTAAAAGCAGCCAACGTTGGTAGCCTGTTCCTCAAA

CGAGGATGGCCAAGAAAAGCAACGCAACCCAGATCAACATCGGCATCAGCGACAAGGATC 3240
GCTCCTACCGGTTCTTTTCGTTGCGTTGGGTCTAGTTGTAGCCGTAGTCGCTGTTCCTAG

GCAAGAAGATCGCGGCGGGGCTGTCGCGTCTGCTCGCCGATACGTACACGCTGTACCTGA 3300
CGTTCTTCTAGCGCCGCCCCGACAGCGCAGACGAGCGGCTATGCATGTGCGACATGGACT

AGACGCACAATTTCCACTGGAACGTGACCGGCCCGATGTTCAACACGCTGCACCTGATGT 3360
TCTGCGTGTTAAAGGTGACCTTGCACTGGCCGGGCTACAAGTTGTGCGACGTGGACTACA

TCGAGGAGCAGTACAACGAACTGTGGCTCGCCGTCGATCTCGTCGCGGAGCGCATCCGCA 3420
AGCTCCTCGTCATGTTGCTTGACACCGAGCGGCAGCTAGAGCAGCGCCTCGCGTAGGCGT

CGCTCGGGGTCGTCGCGCCGGGCACGTATCGCGAATTC                        3480
GCGAGCCCCAGCAGCGCGGCCCGTGCATAGCGCTTAAG
                                  EcoRI
```

Figure 2.1. continued.

propagation. For double-stranded DNA sequencing, usually plasmid DNA isolated from JM109 were used. The catalase negative strain UM262 was used for expression of the recombinant BpKatG protein and its variants.

2.3. Media, growth conditions and storage of cultures

E. coli cultures were grown in Luria-Bertani (LB) media containing 10 g/L tryptone, 5 g/L yeast extract, and 5 g/L NaCl. Solid LB media contained 15 g/L agar. Ampicillin was added to a concentration of 100 μg/ml for selection of plasmid containing cells. For the strain CJ236, 40 μg/ml of chloroamphenicol was also added. Long term storage of cultures containing pBpG variants and subclones was accomplished by adding 24 % dimethylsulfoxide before freezing at -60 °C. The bacteriophage R408 was stored at 4 °C in LB supernatant.

2.4. DNA manipulation

2.4.1. Preparation of synthetic oligonucleotides

The oligonucleotides used for site-directed mutagenesis (Table 2.2) were purchased from Invitrogen Canada Inc. in non-phosphorylated form. Oligonucleotide concentration was determined spectrophotometrically at 260 nm, where 1 unit of absorbance approximately equals 20 μg/mL of single-stranded DNA (Sambrook *et al*, 1989).

The oligonucleotides were phosphorylated at the 5'-end using T4 kinase according to the procedure of Ausubel *et al* (1989). Approximately 100 ng of oligonucleotide DNA, 1 mM ATP and 10 units of T4 kinase in a volume of 25 μL were incubated in appropriately diluted buffer supplied by the manufacturer at 37

°C for 30 minutes. The reaction was terminated by incubating at 65 °C for 5 minutes.

2.4.2. Site-directed mutagenesis strategy

The desired base changes to the recombinant *B. pseudomallei katG* were generated according to the *in vitro* mutagenesis protocol described by Kunkel *et al* (1987). Subclones were constructed from parts of the chromosomal insert containing the *katG* gene; a simplified restriction map of the *BpkatG* gene indicating the locations of the individual subclones is shown in Fig. 2.2. The subclone rather than the whole gene was mutated in order to limit the extent DNA sequencing required to confirm the mutation before and after reinsertion into the *BpkatG* gene.

Codons for mutagenesis were selected from the *BpkatG* gene sequence and the oligonucleotide sequence and location are described in Table 2.2. Mutagenesis was performed by annealing the phosphorylated oligonucleotides containing the desired base changes to single-stranded uracil-containing DNA templates from the appropriate subclone. The complementary DNA strand was synthesized *in vitro* by unmodified T7 DNA polymerase using the annealed oligonucleotide as a primer. The completed complementary strand was ligated with T4 DNA ligase in the reaction mixture. After a 3 hour incubation at 37 °C the mixture was transformed into NM522 cells where the uracil-containing templates were degraded. Plasmids recovered from NM522 were subsequently transformed into JM109 because better quality DNA for sequencing was obtained from this strain than from NM522. Plasmids isolated from JM109 were used to

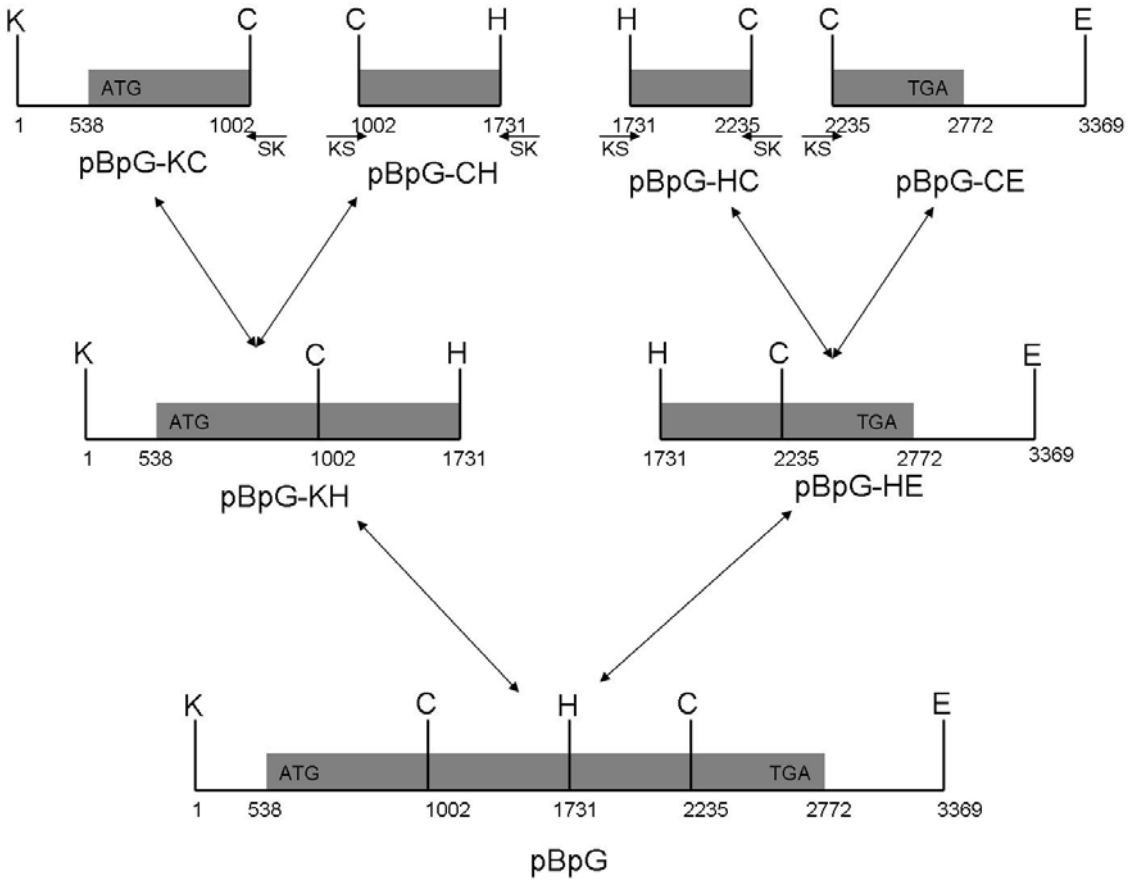

Figure 2.2. Subcloning and sequencing strategy for *Burkholderia pseudomallei katG* (note: K, C, H, and E are the restriction enzymes: *KpnI*, *ClaI*, *HindIII*, and *EcoRI* respectively. SK and KS are the DNA sequencing primers used with each subclone). The grey box represents the *katG* open reading frame as part of the whole chromosomal insert.

Table 2.2. Sequence of oligonucleotides and subclone used for site-directed mutagenesis of *B. pseudomallei katG*.

Primer	Oligonucleotide sequence[a]	Subclone
W111F	CGCATGGCA**TTT**CACAGCGCG	pBpG-KC
W111H	CGCATGGCA**CAC**CACAGCGCG	pBpG-KC
Y238A	GGCCTCATC**GCC**GTGAATCCG	pBpG-CH
Y238F	GGCCTCATC**TTC**GTGAATCCG	pBpG-CH
M264A	TTCGCGCGC**GCG**GACGGCGCG	pBpG-CH
M264L	TTCGCGCGC**CTG**GACGGCGCG	pBpG-CH
W330F	GAAGTCACG**TTC**ACGACGACG	pBpG-CH
R426A	CTTACGCAC**GCC**GACATGGGC	pBpG-HC
R426E	CTTACGCAC**GAG**GACATGGGC	pBpG-HC
R426K	CTTACGCAC**AAG**GACATGGGC	pBpG-HC
R426L	CTTACGCAC**CTC**GACATGGGC	pBpG-HC

[a]The sequences in bold are the codons that have been changed.

screen for the desired mutation by DNA sequencing. Typically, 4 to 6 isolates were screened and, if the desired mutation was not found, the oligonucleotide was re-phosphorylated and the site-directed mutagenesis procedure was repeated.

Once the correct mutation was identified, the complete subclone was sequenced to ensure no other mutations were incorporated during the procedure. The mutated subclone was then used to reconstruct the complete BpkatG gene, which was then sequenced over the region containing the mutation for final conformation.

2.4.3. Reconstruction of mutated subclones into the complete *BpkatG* gene

Reconstruction of the mutant *katG* gene involved 2 steps. A general outline for reconstruction is illustrated in Fig. 2.1. First, the subclone containing the desired mutation (either pBpG-KC, pBpG-CH, pBpG-HC, or pBpG-CE) was cut with the appropriate restriction enzymes and ligated into pBpG-KH or pBpG-HE subclone that were also cut with the same restriction enzymes. Next, the pBpG-KH or pBpG-HE subclones containing the desired mutation were similarly cut and ligated into the whole BpKatG gene to generate the final mutated whole gene. At each step the constructs were checked by restriction endonuclease digestion and agarose gel electrophoresis to ensure proper ligation into the desired clone.

2.4.4 DNA isolation and purification

Plasmid DNA was isolated according to Sambrook *et al* (1989). All procedures were carried out at room temperature. Plasmid containing cells were picked from isolated colonies and grown overnight in 5 mL LB cultures from

which approximately 3 mL were pelleted by centrifugation and resuspended in 200 µL of glucose-EDTA-RNase buffer (25 mM Tris-HCl, pH 8.0, 1 % glucose, 10 mM Na-EDTA, and 0.35 mg/mL RNase). The cells were then lysed with 400 µL of a solution of 1 % SDS and 0.2 M NaOH. After a 10 minute incubation, 300 µL of 6.3 M ammonium acetate was added and the mixture was centrifuged twice to remove all precipitate. Plasmid DNA was then precipitated by the addition of 550 µL isopropanol. After a 15 minute incubation, plasmid DNA was pelleted by centrifugation, washed twice with 70 % ethanol, and dried under vacuum. The DNA pellet was resuspended in either water or TE buffer (10 mM Tris, pH 8.0, 1 mM Na-EDTA) and stored at -20 °C until needed.

Template, single-stranded DNA for site-directed mutagenesis was prepared according to Vieira and Messing (1987). Plasmid containing cells were grown in 5 mL LB broth to early exponential phase and then infected with 50 µL of helper phage R408 and 50 µL of 1 M $MgSO_4$ and grown overnight. Approximately 3 mL of culture were divided into 2 microtubes and centrifuged to remove cells and debris. A solution of 300 µL of 1.5 M NaCl, 20 % PEG 6000 was then added to each tube and incubated at room temperature for 15 minutes and centrifuged to pellet the phage particles. The phage particles were resuspended in TE buffer and pooled into 1 tube. The resuspended phage particles were then extracted with an equal volume of phenol, followed by an equal volume of water saturated chloroform. Single-stranded DNA was finally precipitated by the addition of an equal volume of 7.5 M ammonium acetate, pH 7.5 and 4 volumes of ice-cold 95 % ethanol followed by incubation at -20 °C for a

minimum of 30 minutes. The single-stranded DNA was then pelleted by centrifugation and washed once with 95 % ethanol and twice with 70 % ethanol. The dried pellet was stored at -20 °C until needed.

2.4.5. Restriction endonuclease digestion of DNA

Restriction digestions were performed at 37 °C for 2-5 hours in a total volume of 10 µL, containing 1 µL of 10X of the appropriate buffer provided by the supplier, 1-5 µg DNA, and 0.5-1 µL of the appropriate endonuclease(s).

2.4.6. Agarose gel electrophoresis

Electrophoresis of the restriction endonuclease digested DNA was performed according to Sambrook *et al* (1989). Agarose gels containing 1 % agarose and 0.1 µg/mL ethidium bromide were prepared in TAE buffer (40 mM Tris-acetate and 1 mM EDTA, pH 8.0) and cast in Bio-Rad Mini Sub Cell Plexiglass horizontal electrophoresis trays (6.5 cm x 10 cm). Samples of 10 µL volumes were mixed with 2 µL stop buffer (40 % glycerol, 10 mM EDTA pH 8.0, 0.25 % bromophenol blue). 1 Kb DNA Ladder or 1 Kb Plus DNA Ladder from Invitrogen Canada Inc. served as molecular weight size standards. Electrophoresis was carried out at 40-60 mA constant current in TAE buffer until the bromophenol blue dye marker front had migrated approximately two-thirds the length of the gel. The DNA bands were visualized with ultraviolet light and recorded using a Gel Doc 1000 image capture system (Bio-Rad).

2.4.7. Ligation

The DNA fragments to be ligated were excised from agarose gels and purified using the Ultraclean™ 15 DNA purification kit from Bio/Can Scientific

Inc. according to the instructions supplied by the manufacturer. Ligation of DNA fragments was carried out according to the procedure of Sambrook *et al* (1989). Purified DNA fragments were mixed in a ratio of 2-3 of mutant insert to vector in 10 μL volumes, containing 1 unit of T4 DNA ligase, and the manufacturer's supplied buffer at the appropriate concentration. The ligation mixtures were incubated overnight at 15 °C before being transformed into NM522. A mixture without the mutant insert DNA was used as a control.

2.4.8. Transformation

Transformation of *E. coli* cells with plasmid DNA was done according to Chung *et al* (1989). The appropriate strain of *E. coli* cells was grown to exponential phase (typically 2-4 hours) in 5 mL LB cultures, harvested by centrifugation and rendered competent by resuspension in 500 μL of ice-cold 0.1 M $CaCl_2$. After a minimum incubation on ice of 30 minutes 2-10 μg of plasmid DNA was added to 100 μL of the cell suspension, followed by a further 30 minute incubation on ice, and a 90 second heat shock at 42 °C. Ice-cold LB medium (900 μL) was then added to the cell suspension and incubated at 37 °C for 1 hour. The mixture was either spread, or in the case of ligation mixtures, mixed with 3 mL of molten R-top LB agar and poured onto ampicillin containing LB plates.

2.4.9. DNA sequencing

Initially, manual sequencing was carried out with double-stranded DNA templates according to the method of Sanger *et al* (1977) using either primers supplied with the pKS- vector or other primers, as appropriate for the particular mutant of interest. For preparation of the double-stranded DNA template, 5 μg

plasmid DNA was resuspended and denatured in a 40 µL volume of 2 M NaOH freshly prepared. This mixture was incubated for 10 minutes at 37 °C, and the DNA was precipitated by addition of 10 µL of 3 M sodium acetate, pH 4.8 and 140 µL of ice-cold 95 % ethanol. Following incubation at -20 °C for a minimum of 30 minutes, the DNA pellet was recovered by centrifugation, and washed once with 1 mL of ice-cold 95 % ethanol, and twice with 70 % ice-cold ethanol, and dried under vacuum. Annealing and sequencing reactions were carried out using a T7 Sequencing Kit according to the manufacturer's specifications using 10 µCi [α-^{35}S] dATP (Amersham Biosciences). Reaction mixtures were separated and resolved on 8 % polyacrylamide vertical slab gels (7 M urea, 0.13 M Tris, 0.13 M boric acid, and 10 mM EDTA). Electrophoresis was carried out using 10-24 mA constant current in TBE buffer (90 mM Tris, 89 mM borate, and 2.2 mM EDTA) for 2-5 hours as required for the mutant of interest. Gels were mounted on 3 mm Whatman paper and dried at 80 °C for 1 hour in a slab gel drier vacuum (Savant). The dried gels were exposed to X-ray film (Kodak X-OMAT AR) for a minimum of 48 hours. The X-ray film was then developed in order to visualize and record the DNA bands.

In the later half of this thesis work, manual sequencing was replaced by automated sequencing. Automated sequencing was carried out on an Applied Biosystems model 3130 Genetic Analyzer. The DNA to be sequenced was isolated and purified as described above except the DNA pellet was resuspended in water instead of TE buffer as recommended by the instructions in the BigDye® Terminator v1.1 Cycle Sequencing Kit (Applied Biosystems). The sequencing

reaction mixture contained approximately 200 ng of DNA with 3 pmol of the appropriate primer and sequencing was cared out according to the instructions in the BigDye® Terminator v1.1 Cycle Sequencing Kit (Applied Biosystems) in a final volume of 20 µL. The PCR cycle program for the sequencing reaction included a preheat step for 1 minute followed by 25 cycles of denaturing, annealing and extension steps respectively at 96 °C for 10 seconds, 50 °C for 5 seconds, and 64 °C for 4 minutes, followed by cooling to 4 °C. The DNA was then purified by precipitation by the addition of 2 µL of 125 mM EDTA, 2 µL of 3 M sodium acetate, pH 4.8, 60 µL of 95 % ethanol and gently mixed by inversion. After 15 minute incubation at room temperature, the DNA was recovered by centrifugation at 4 °C for 15 minutes. The supernatant was carefully removed by pipetting and 60 µL of 70 % ice cold ethanol was added and centrifuged at 4 °C for 15 minutes. The supernatant was again removed by pipetting and the final pellet was dried for a minimum of 30 minutes under vacuum. Finally, the purified DNA pellet was denatured by addition of 20 µL of Hi-Dye formamide, thoroughly mixed by vortexing and incubated at 94 °C for 5 minutes before being loaded into the sample plate for automated sequencing.

2.5. Purification of BpKatG and its variants

Before large scale purification, plasmid-containing UM262 cells were grown in small 30 mL flasks of LB medium at both 28 °C and 37 °C for 16-20 hours to test for optimal expression of the variant protein. Whole cells were tested for catalase activity and protein expression profile by electrophoresis on sodium dodecyl sulfate polyacrylamide gels (SDS-PAGE).

For large scale purifications of BpKatG and its variants, UM262 cells transformed with the plasmid expressing the desired protein were grown in 8 liters of LB media in 2 liter shake flasks (500 mL per flask) supplemented with 100 µg/mL of ampicillin and 40 µg/mL hemin, for 16-20 hours with good aeration. Cells were grown at either 28 °C or 37 °C based on the results of small scale test for each variant. Isolation of BpKatG and its variants were done according to the procedure of Loewen and Switala (1986) with modifications. All purification steps were carried out at 4 °C. Cells were harvested from the growth medium by centrifugation and the cell pellet was stored at -60 °C if purification was not started immediately.

The cell pellet was resuspended in 50 mM potassium phosphate buffer, pH 7 containing 5 mM EDTA in a ratio of 75 g cells to 400 mL buffer. The cells were disrupted by a single pass through a French pressure cell at 20,000 psi. Unbroken cells and debris were removed by centrifugation, yielding the crude extract, to which streptomycin sulfate was added to a final concentration of 2.5 %. The resulting precipitates were removed by centrifugation and discarded. Solid ammonium sulfate was added starting at a concentration of 35 %, incrementally increasing by 5 % up to 50 %, removing each precipitate by centrifugation at each step. BpKatG and its variants were found to precipitate at 40-45 % ammonium sulfate saturation. Pellets from ammonium sulfate precipitations were resuspended in 10-20 mL of 50 mM potassium phosphate, pH 7.0. Presence of the desired protein in the pellets was confirmed by assays for catalase activity and in the case of inactive variants visualized by SDS-PAGE gels. Resuspensions

were centrifuged to remove any remaining precipitates, and dialyzed overnight using a 12,000-14,000 molecular weight cutoff membrane, against 2 liters of 50 mM potassium phosphate, pH 7.0.

The dialyzed resuspensions were centrifuged again and loaded onto a 2.5 cm x 23 cm column of DEAE-cellulose A-500 (Cellufine, Amicon) equilibrated with 50 mM potassium phosphate, pH 7.0. The loaded column was washed with 50 mM potassium phosphate until the absorbance at 280 nm was below 0.025. The protein was then eluted with a linear gradient of 0-400 mM NaCl in 50 mM potassium phosphate with a total volume of 1 liter. Approximately 5 mL fractions were collected off the column. Purity of the recovered fractions was based on the ratio between the absorbance at 407 nm and 280 nm. Only fractions with the highest ratio were pooled and concentrated under nitrogen in a stirred pressure cell (model 8050, Amicon) using an YM-30 membrane to a protein concentration of about 20 mg/mL. The concentrated sample was dialyzed against 1 liter of 50 mM potassium phosphate, pH 7.0 overnight. The final dialyzed protein was checked for purity and health by measuring catalase activity and heme to protein ratio, visualized using SDS-PAGE, and absorption spectra were recorded. Purified protein samples were aliquoted into microtubes in 500 µL volumes and stored at -60 °C until needed.

2.6. Sodium dodecy sulfate-polyacrylamide gel electrphoresis (SDS-PAGE)

Denaturing SDS-PAGE was carried out according to Weber *et al* (1972). Discontinuous 4 % stacking and 8 % separating polyacrylamide gels were cast as vertical slabs of dimensions 10 x 10 cm and 0.5 mm thickness. Samples loaded

onto the gels usually contained 5-10 μg of protein. Samples were mixed with equal volumes of reduced sample buffer (3.4 mg/mL NaH_2PO_4, 10.2 mg/mL Na_2HPO_4, 10 mg/mL SDS, 0.13 mM 2-mercaptoethanol, 0.36 g/mL urea and 0.15 % bromophenol blue) and boiled for 3 minutes before loading. Gels were run with 150 volts, constant voltage, until the dye reached the bottom, in a vertical BIO-RAD Mini-Protean II electrophoresis system, using a running buffer containing 14 g/L glycine, 3 g/L Tris base, and 1 g/L SDS. Gels were stained with a solution containing 0.5 g/L Coomassie Brilliant Blue R-250, 30 % ethanol and 10 % acetic acid for 1 hour, and destained with repeated changes of destaining solution containing 15 % methanol and 7 % acetic acid until the background was clear. The gels were then soaked in a solution containing 7 % acetic acid and 1 % glycerol for 30 minutes before being mounted on 3 mm Whatman paper, covered with clear plastic film, and dried at 80 °C for 1 hour on a slab gel drier under vacuum.

2.7. Enzymatic assays and protein quantification

2.7.1. Protein concentration

Purified protein concentrations (mg/mL) were estimated spectrophotometrically (Sambrook *et al*, 1989) based on the absorbance at 280 nm calculated as: (A_{280} x 79198)/138870, where the molar extinction coefficient of BpKatG is 138870 based on the amino acid composition and molecular weight of 79198 g/mol. During protein purification, the Warburg-Christian method was used to estimate protein concentration (Warburg and Christian, 1941, and Layne, 1957).

2.7.2. Catalase activity

Catalase activity was determined by the method of Rørth and Jensen (1967) in a Gilson oxygraph equipped with a Clark electrode. One unit of catalase is defined as the amount of enzyme that decomposes 1 μmol of hydrogen peroxide in 1 minute in 60 mM H_2O_2 at pH 7.0 and 37 °C. Typically, 1.8 mL of 50 mM potassium phosphate buffer, pH 7.0 was added to the reaction chamber followed by the addition of 50 μL of hydrogen peroxide to the final concentration of 60 mM. Once the oxygraph had stabilized, the appropriately diluted enzyme or cells were added. Catalase activity (units/mL) was determined from the slope of oxygen evolution. Specific catalase activity was expressed as units/mL-mg purified protein. Specific catalase activity of whole cells (units/mg dry cell weight) was determined using a Loewen laboratory protocol involving the conversion of cell turbitiy values at 600 nm to Klett values and applying a previously determined factor that equates Klett value to dry cell weight.

2.7.3. Peroxidase activity

Peroxidase activity was determined spectrophotometrically using 2,2'-azinobis(3-ethylbenzothiazolinesulfonic acid) (ABTS) (Childs and Bardsley, 1975) and o-dianisidine (Claiborne and Fridovich, 1979). Typically, assays were carried out at room temperature in 1 mL final volume in 50 mM sodium acetate buffer pH 4.5 containing 1 mM hydrogen peroxide, either 0.34 mM o-dianisidine or 0.4 mM ABTS, and aliquots (5-10 μL) of the appropriately diluted enzyme to start the reaction. Peroxidase specific activity was determined monitoring the change in absorbance over 2 minutes. In the case of o-dianisidine the absorbance

was measured at 460 nm, using a molar extinction coefficient of $\varepsilon = 11300\ M^{-1}cm^{-1}$. In the case of ABTS the absorbance was measured at 405 nm, using a molar extinction coefficient of $\varepsilon = 36800\ M^{-1}cm^{-1}$. In both cases peroxidase activity was determined by the ΔA/min (change in absorbance per minute) over periods of 2 minutes and expressed as units/mL-mg purified protein calculated as (ΔA/min)/(ε x mg enzyme/mL reaction mixture). One unit of peroxidase activity is defined as the amount that decomposes 1 μmol of electron donor (ABTS or o-dianisidine) in 1 minute at pH 4.5 and room temperature.

2.7.4. Michaelis-Menten kinetics

Kinetic parameters for the reactions catalyzed by both the catalase and peroxidase reactions were determined using the program SigmaPlot (Systat Software Inc.) by fitting initial velocities at varying substrate concentrations to the Michaelis-Menten equation using non-linear regression. The parameters were determined at the optimal pH for each reaction, namely pH 4.5 for the peroxidase reaction and pH 7.0 for the catalase reaction. In the case of the peroxidase reaction, constants were determined for both substates hydrogen peroxide and ABTS. When determining the K_M of ABTS, the concentration of hydrogen peroxide was fixed at a concentration well above its K_M value, and similarly when determining the K_M of hydrogen peroxide the concentration of ABTS was fixed at a concentration well above its K_M value.

2.8. Absorption spectroscopy

Manual mixed time course enzyme assays were carried out using a Pharmacia Ultrospec 4000 or Biochrom Ultrospec 3100 pro spectrophotometer.

Manual mixed absorption spectra were recorded on a Milton Roy MR300 Spectrphotometer. In all cases experiments were performed at room temperature in 1 mL quartz, semi micro cuvettes. Unless otherwise stated proteins were diluted in 50 mM potassium phosphate buffer, and the same buffer was used as a reference.

Stopped-flow absorption spectra and single wavelength measurements were recorded on a SX20 Stopped-Flow Spectrometer (Applied Photophysics) equipped with a 1 cm, 20 μL observation cell, with a dead time of 1.1 ms. Absorption spectra were recorded using enzyme pretreated with a 10-fold excess of peroxyacetic acid and returned to resting state by numerous washes with buffer to ensure a complete Met-Tyr-Trp cross-link was formed. Typically, absorption spectra for the wild-type and variant enzymes were recorded at room temperature with a final protein concentration of 4 μM for 10-20 seconds in at least duplicate. The resulting absorption spectral data sets were fit by global-analysis with the Pro-Kineticist software (Applied Photophysics). Concentration dependence with peracetic acid and 3-chloroperoxybenzoic acid was verified by single wavelength measurements at 409 nm with 4 μM protein and increasing amounts of acid. Rates were determined simultaneously by fitting the time trace at 409 nm to a double exponential equation (in the case of the wild-type enzyme) and a single exponential equation (in the case of the W330F variant) for the various peroxyacetic acid and 3-chloroperoxybenzoic acid concentrations using the curve fitting application in the Pro-Data Viewer software (Applied Photophysics).

2.9. BpKatG crystallization and structure determination

Crystals were obtained in 4 to 10 days at 20 °C by the vapor-diffusion, hanging drop method with 2 μL of a 10 mg/mL purified protein solution and 1 μL of the reservoir solution containing 16-20 % polyethylene glycol (PEG-4K), 20 % 2-methyl-2,4-pentanediol (MPD), 70 mM NaCl, and 100 mM sodium citrate pH 5.6 (Carpena *et al*, 2002 and 2003). Diffraction data were obtained from crystals cooled with a nitrogen cryo-stream. Diffraction data sets were collected from an in-house X-ray source (RA-Micro7 HFM tabletop rotating anode X-ray generator and R-AXIS IV^{++} CE detector; Rigaku Corporation) and from a synchrotron at the Canadian Light Source at the University of Saskatchewan, beamline CMCF1. The diffraction data sets were processed using the program MOSFLM and scaled with the program SCALA (Otwinowski and Minor, 1996). Structure determination was carried out using the program REFMAC (Murshudov *et al*, 1997), and the graphics programs O (Jones *et al*, 1991) and Coot (Emsley and Cowtan, 2004). All figures containing protein structures were prepared with either VMD (Humphrey *et al*, 1996) or PyMOL (DeLano, 2002).

Structures of bound INH, NAD^+, AMP, or ADP were obtained by incubating a 7.5 mg/mL or 10.0 mg/mL protein solution in 25 mM of the appropriate substrate in 50 mM potassium phosphate buffer at pH 7.0 at 37 °C for approximately 30 minutes prior to spotting on crystallization trays. Additionally, 100 mM INH or 10 mM NAD^+, AMP, or ADP was added to the crystallization reservoir solution. Otherwise, identical crystallization conditions to unbound enzyme were used.

3. THE ROLE OF ARG426 AND THE MET264-TYR238-TRP111 COVALENT ADDUCT IN MODULATING THE CATALASE REACTION

3.1. Introduction

The catalase and peroxidase reactions involve a common path of oxoferryl formation (compound I), but differ in the path for compound I reduction back to resting state. Catalases reduce compound I via a single 2 electron transfer from hydrogen peroxide, whereas peroxidases reduce compound I through 2 sequential 1 electron transfers utilizing various biomolecules as electron donors. Catalase-peroxidases are unique members of the class I plant peroxidase family that are capable of performing the catalase reaction despite having a similar active site and overall topology to other monofunctional peroxidases.

The recent success in crystallization of catalase-peroxidases from *Haloarcula marismortui* (Yamada *et al*, 2002), *Burkholderia pseudomallei* (Carpena *et al*, 2003b), *Synechococcus* PCC7942 (Wada *et al*, 2002) and *Mycobacterium tuberculosis* (Bertrand *et al*, 2004) revealed a unique covalent cross-link joining the side chains of Met264, Tyr238, and Trp111. This covalent linkage involves the indole ring of the active site Trp111 and the sulfur of Met264 joined to the ortho positions of Tyr238. Changes to the active site Trp111 resulted in a compete loss of catalase activity with little or no effect on peroxidase activity (Hillar *et al*, 2000, and Regelsberger *et al*, 2000) suggesting a possible catalase-specific role of this cross-link. Similarly, changes to either Met264 or Tyr238 also resulted in complete loss of catalase activity with little or no affect on peroxidase activity (Jakopitsch *et al*, 2003a, Jakopitsch *et al*, 2004, and Yu *et al*,

2003b). Thus, it is clear that this adduct is somehow crucial for catalase activity and it has been speculated that it could play a role in stabilizing the enzyme, anchoring the active site Trp111 in place to allow for optimal reactivity, and/or potentially providing a conduit for electrons to travel to and from the heme active site (Carpena *et al*, 2003b). The crystal structures also revealed a conserved arginine (Arg426) that is in ionic association with Tyr238 of the covalent cross-link. Removal of this residue also resulted in enzymes with catalase activity of only 5 % of the wild-type enzyme without effecting peroxidase activity (Jakopitsch *et al*, 2004).

3.2. Results

3.2.1. Purification and characterization of BpKatG and its variants

BpKatG and variants of residues involved in the Met-Tyr-Trp adduct, namely W111F, W111H, Y238A, Y238F, M264A, and M264L were purified as outlined in the material and methods and analyzed by SDS-PAGE as shown in Fig. 3.1, Panel A. The wild-type enzyme and all variants have similar electrophoretic mobility and a predominant band with an apparent molecular mass of roughly 79 kDa. The larger bands at approximately 160 kDa and higher are most likely dimer and larger aggregates which are not reduced with either β-mercaptoethanol or dithiothreitol added to the sample buffer. Purified variants of R426, namely R426A, R426E, R426K, and R426L were also analyzed by SDS-PAGE (Fig. 3.1 B) revealing similar electrophoretic mobility to those of the variants involved in the Met-Tyr-Trp cross-link. The absorption spectra of the purified wild-type enzyme along with those of the variants are shown in Fig 3.2

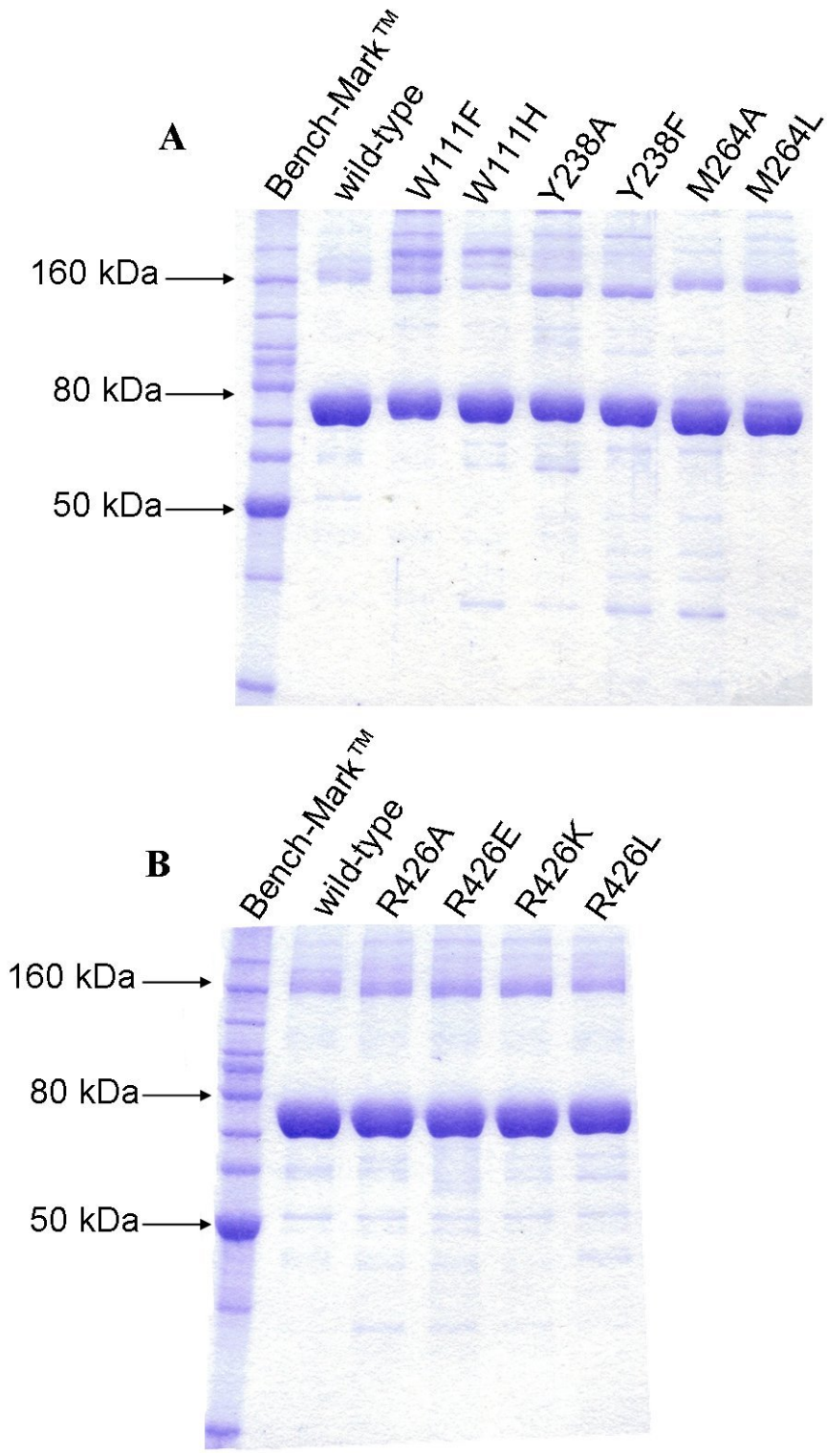

Figure 3.1. SDS-polyacrylamide gel electrophoretic analysis of purified wild-type BpKatG and its variants. Approximately 3.0 μg of protein were separated on an 8% polyacrylamide gel and stained with Coomassie brilliant blue. Panel A: variants involved in the Met-Tyr-Trp cross-link. Panel B: variants of R426.

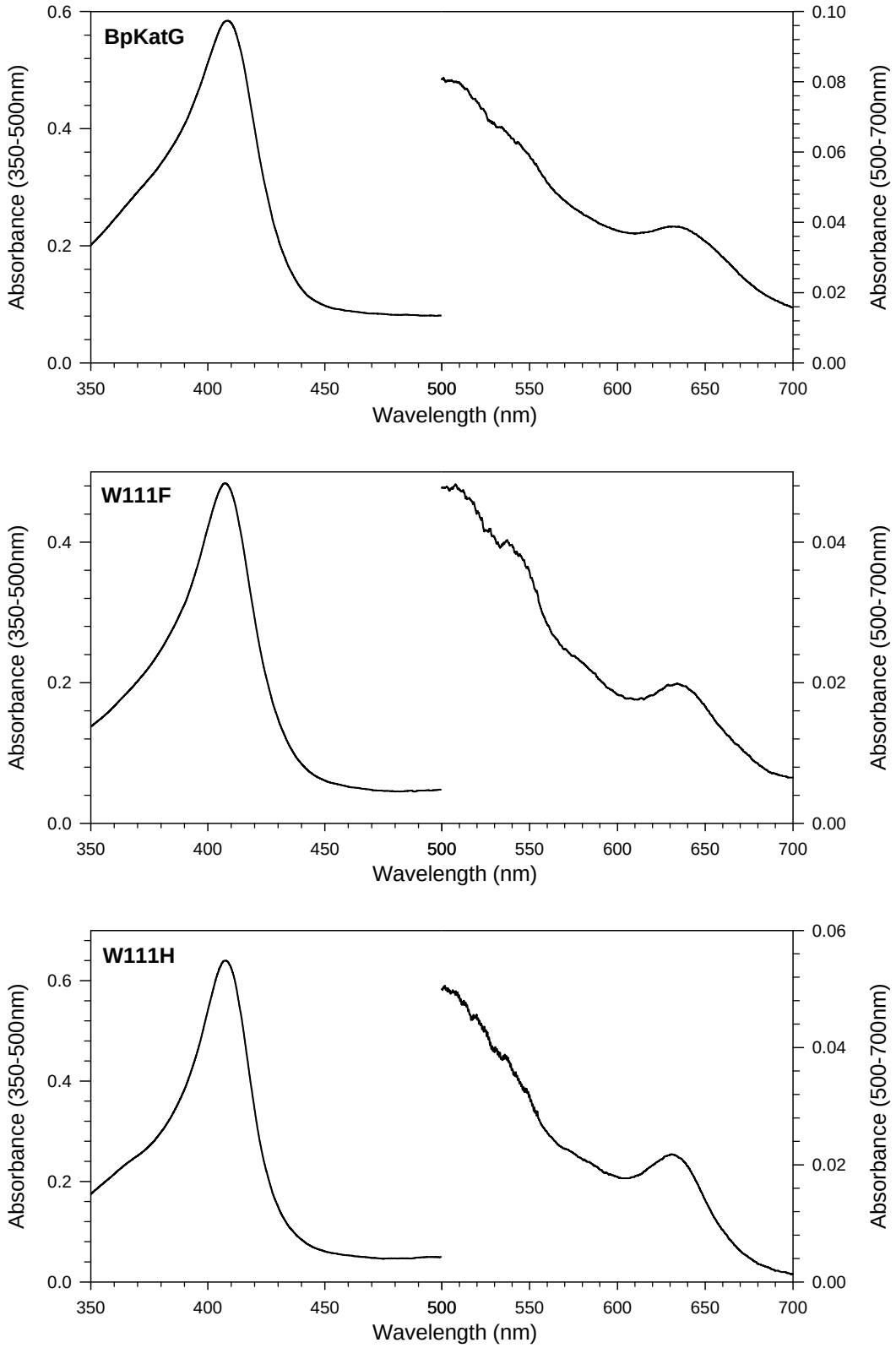

Figure 3.2. Ferric resting-state absorption spectra of purified wild-type BpKatG and its variants.

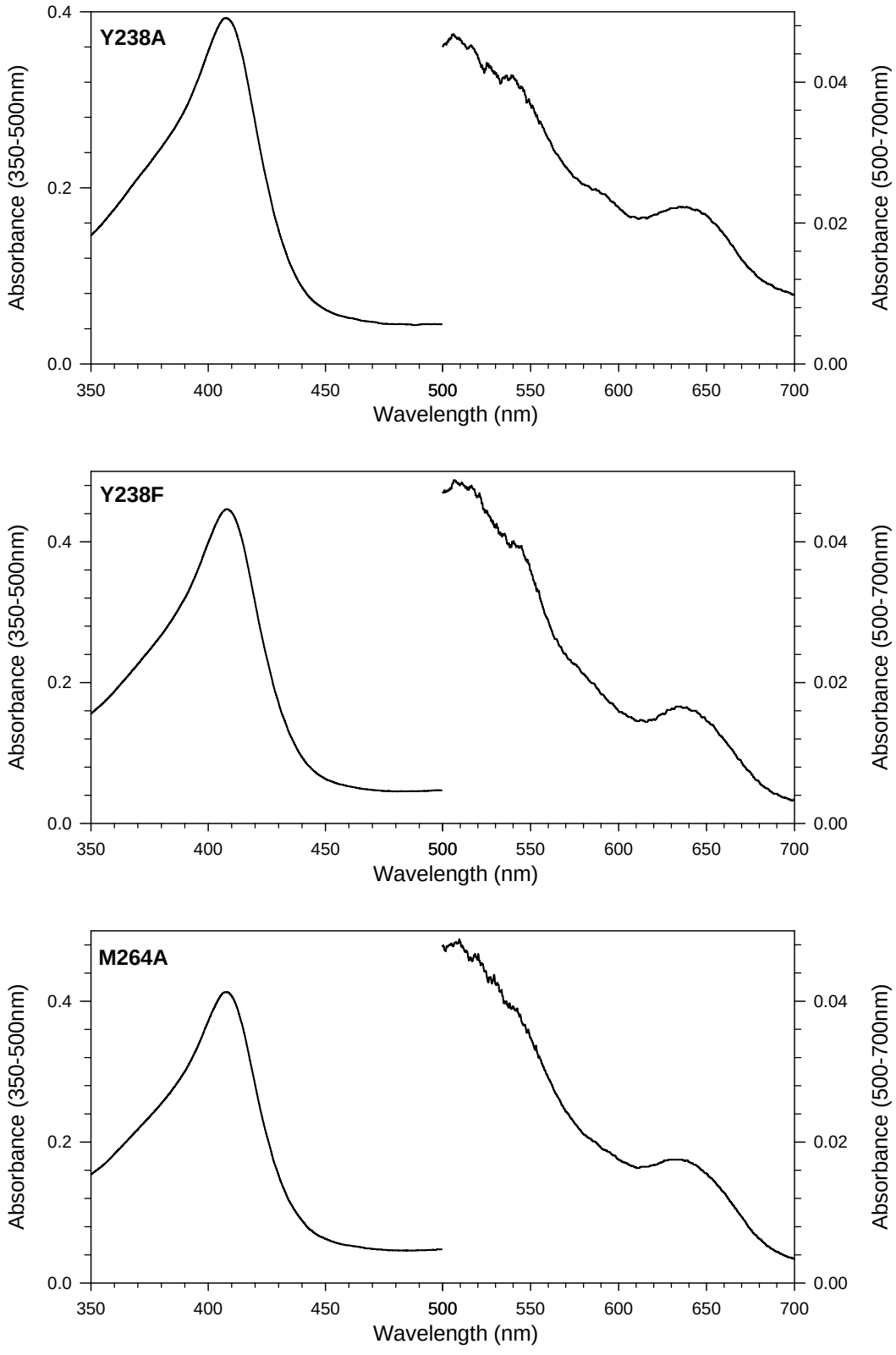

Figure 3.2. continued.

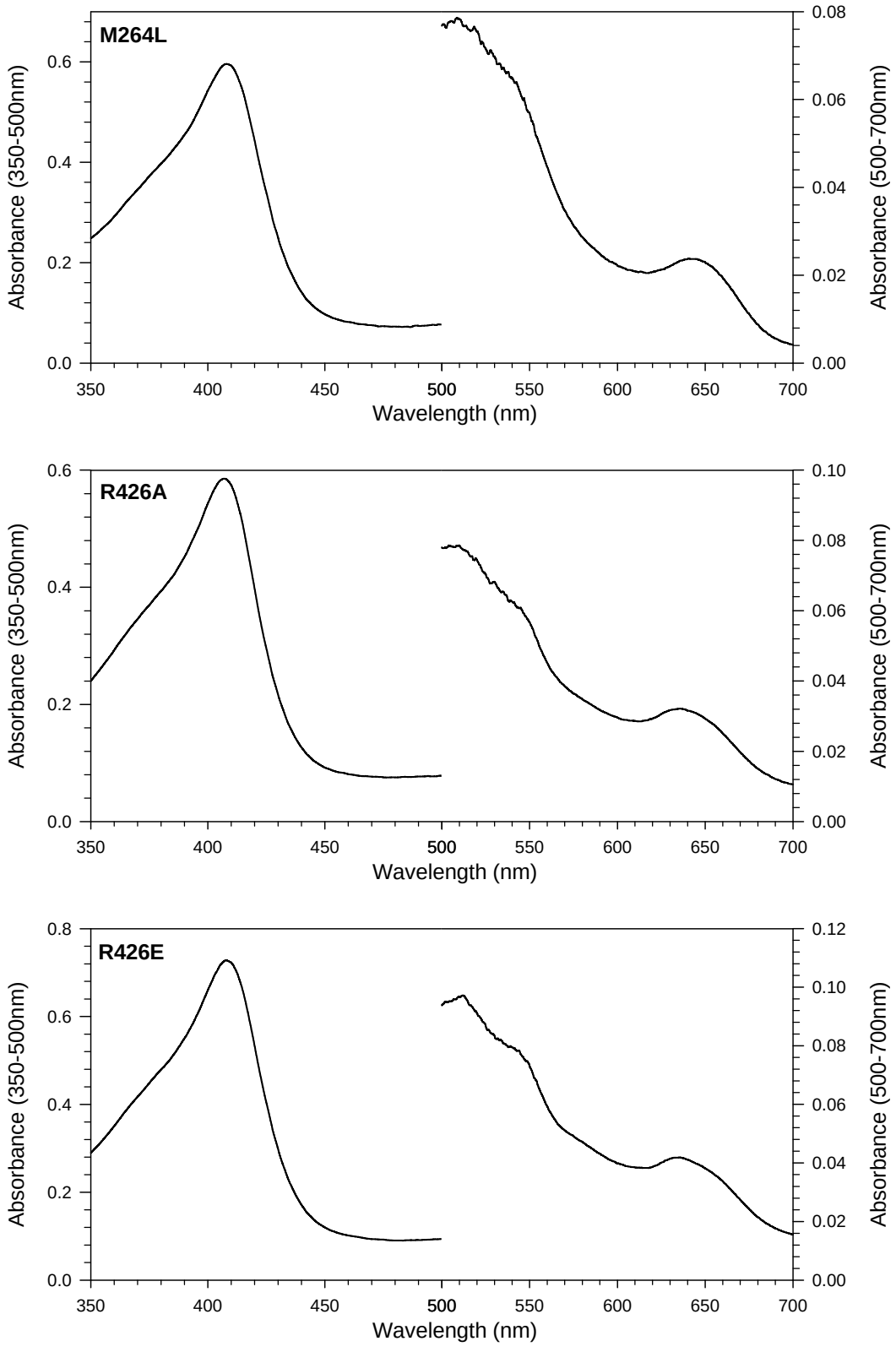

Figure 3.2. continued.

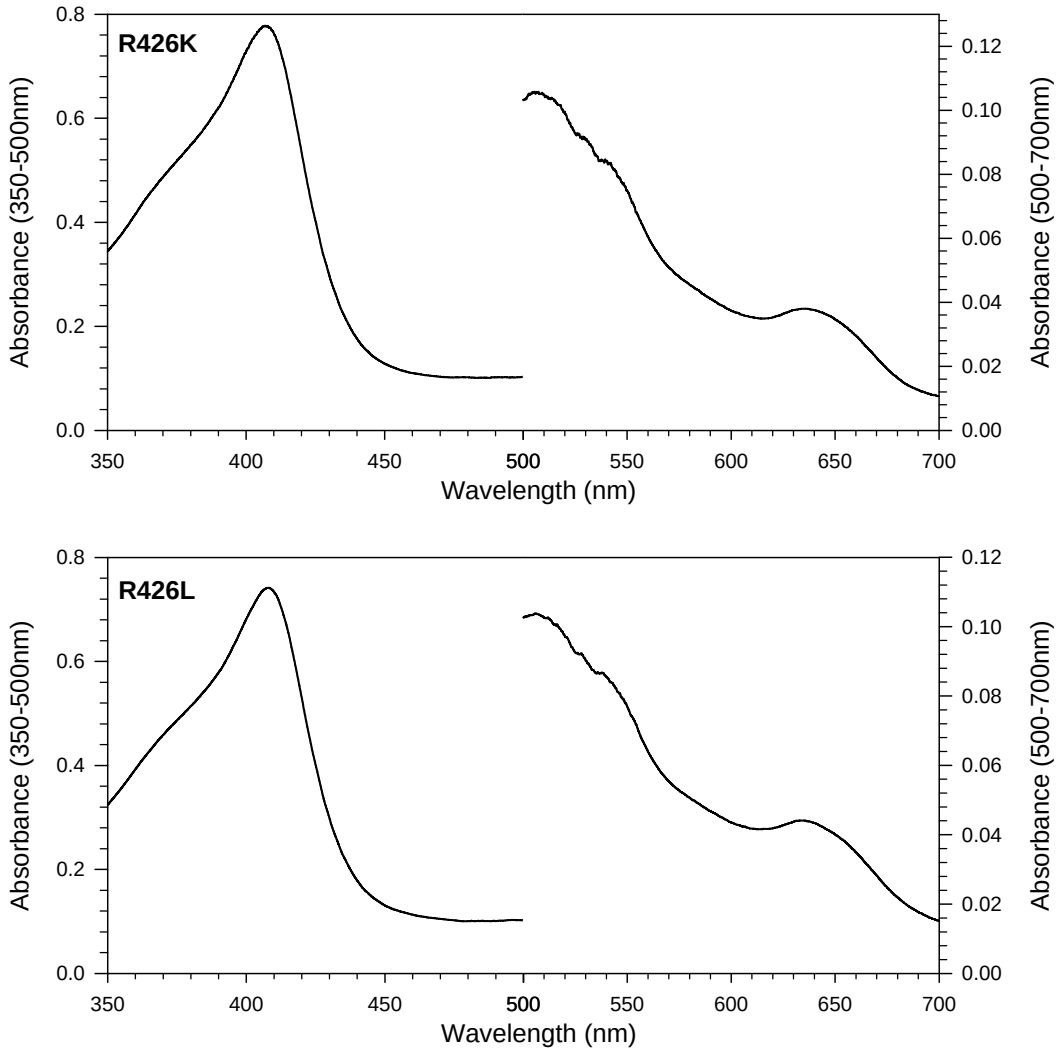

Figure 3.2. continued.

for comparison and Table 3.1 summarizes the positions of the absorption maxima and heme to protein ratios ($A_{407/280}$). In every case the absorption maxima of the Soret band is within 1 nanometer of 407 nm seen in the wild-type enzyme. Except for the wild-type enzyme and variants of Trp111, all show the presence of a shoulder around 375 nm attributed to the presence of a small amount of 6-coordinated heme. Also, subtle differences in the spectra are seen in the 500-700 nm region ranging from a slight shoulder around 550 nm in the case of R426 variants to an increased absorbance peak around 650 nm in the case of W111H, and are generally indicators of changes to the hydrogen bonding network in the vicinity of the heme. Purified wild-type BpKatG and variants consistently had an $A_{407/280}$ ratio between 0.56 and 0.62 with the exception of M264L which was noticeably lower at 0.47, and W111H which was quite a bit higher at 0.84 suggesting a change in the absorption properties of the heme and/or the protein in those 2 variants.

Table 3.2 summarizes the catalase and peroxidase activities of wild-type BpKatG and its variants. Remarkably, changes to residues involved in the Met264-Tyr238-Trp111 cross-link reduced catalase activites to 0.1-0.8 % of wild-type enzyme levels. Peroxidase activity was measured using 2 different 1 electron donors; ABTS and o-dianisidine, and rates were also reduced compared to wild-type enzyme levels ranging from 20-80 %. Interestingly, the W111H variant displayed peroxidase activity roughly 4 times greater then that of the wild-type enzyme when ABTS was used and roughly 3 times greater when o-dianisidine was used. Changing Arg426 to an alanine, glutamate, or leucine also

Table 3.1. Observed optical absorbance maxima and $A_{407/280}$ ratio for purified wild-type BpKatG and its variants.

Enzyme	Soret maximum (nm)	$A_{407/280}$ ratio[a]	% Heme Occupancy[b]
wild-type	407	0.62	86.1
W111F	407	0.56	77.8
W111H	408	0.84	117
Y238A	407	0.57	79.2
Y238F	407	0.60	83.3
M264A	407	0.57	79.2
M264L	408	0.48	66.7
R426A	407	0.56	77.8
R426E	408	0.57	79.2
R426K	407	0.62	86.1
R426L	408	0.61	84.7

[a]The theoretical $A_{407/280}$ ratio is 0.72.
[b]Based on the theoretical $A_{407/280}$ maximum of 0.72.
ε at 280 nm is calculated based on ε_{Trp} = 5500 $M^{-1}cm^{-1}$ and ε_{Tyr} = 1490 $M^{-1}cm^{-1}$ and for the heme at 407 nm ε = 100,000 $M^{-1}cm^{-1}$.

Table 3.2. Catalase and Peroxidase activities of purified BpKatG and its variants.

Enzyme	Catalase[a]	Peroxidase	
		ABTS[b]	o-dianisidine[c]
wild-type	4300 ± 300	10.9 ± 1.4	8.0 ± 0.5
W111F	4.6 ± 0.3	2.5 ± 0.6	2.3 ± 0.1
W111H	4.8 ± 0.3	39.9 ± 1.7	19.2 ± 0.6
Y238A	7.7 ± 0.4	3.7 ± 1.7	5.6 ± 0.4
Y238F	19.0 ± 0.3	2.2 ± 0.2	4.1 ± 0.3
M264A	35.0 ± 2.0	3.7 ± 0.3	5.2 ± 0.1
M264L	26.0 ± 1.3	3.1 ± 1.4	5.1 ± 0.2
R426A	190 ± 6.0	10.8 ± 1.4	3.3 ± 0.1
R426E	214 ± 9.2	10.3 ± 0.8	4.4 ± 0.2
R426K	3000 ± 240	10.6 ± 0.4	10.1 ± 0.1
R426L	170 ± 5.6	11.0 ± 2.4	4.6 ± 0.1

[a]Expressed as μmole H_2O_2•min^{-1}•mg^{-1} metabolized.
[b]Expressed as μmole ABTS•min^{-1}•mg^{-1} reduced.
[c]Expressed as μmole o-dianisidine•min^{-1}•mg^{-1} reduced.

resulted in a dramatic loss of catalase activity to approximately 4.5 % of wild-type enzyme levels. However, changing Arg426 to the similar, but 1 carbon atom shorter lysine maintained catalase activity at 70 % of wild-type enzyme levels. Peroxidase activites as measured with ABTS were identical to that obtained for the wild-type enzyme in all 4 cases. However, when measured with o-dianisidine, peroxidase activity was reduced to about 50 % except for R426K which was actually about 20 % greater than the wild-type enzyme, suggesting that ABTS and o-dianisidine have different binding sites.

3.2.2. Steady-state kinetic characterization of BpKatG and its variants

Kinetic parameters for the reactions catalyzed by both the catalase and peroxidase reactions were determined using the program SigmaPlot (Systat Software Inc.) by fitting initial velocities at varying substrate concentrations to the Michaelis-Menten equation using non-linear regression. The effects of hydrogen peroxide concentration on the catalase reaction for the wild-type and variants enzymes are shown in Fig. 3.3, along with their kinetic constants. As shown in Table 3.3, the K_M value for hydrogen peroxide is approximately 4.0 mM for the wild-type enzyme and this is increased 10 to 100-fold in combination with a decrease in the turnover rate to less than 1% of wild-type enzyme levels for all of the Met, Tyr and Trp variants. Similarly, removal of positively charged Arg426 that is in ionic association with Tyr238 of the cross-link also resulted in a 10-fold increase in the K_M values in combination with a turn-over of less than 5 % of the wild-type enzyme. Additionally, in all cases the k_{cat}/K_M values were lower by at

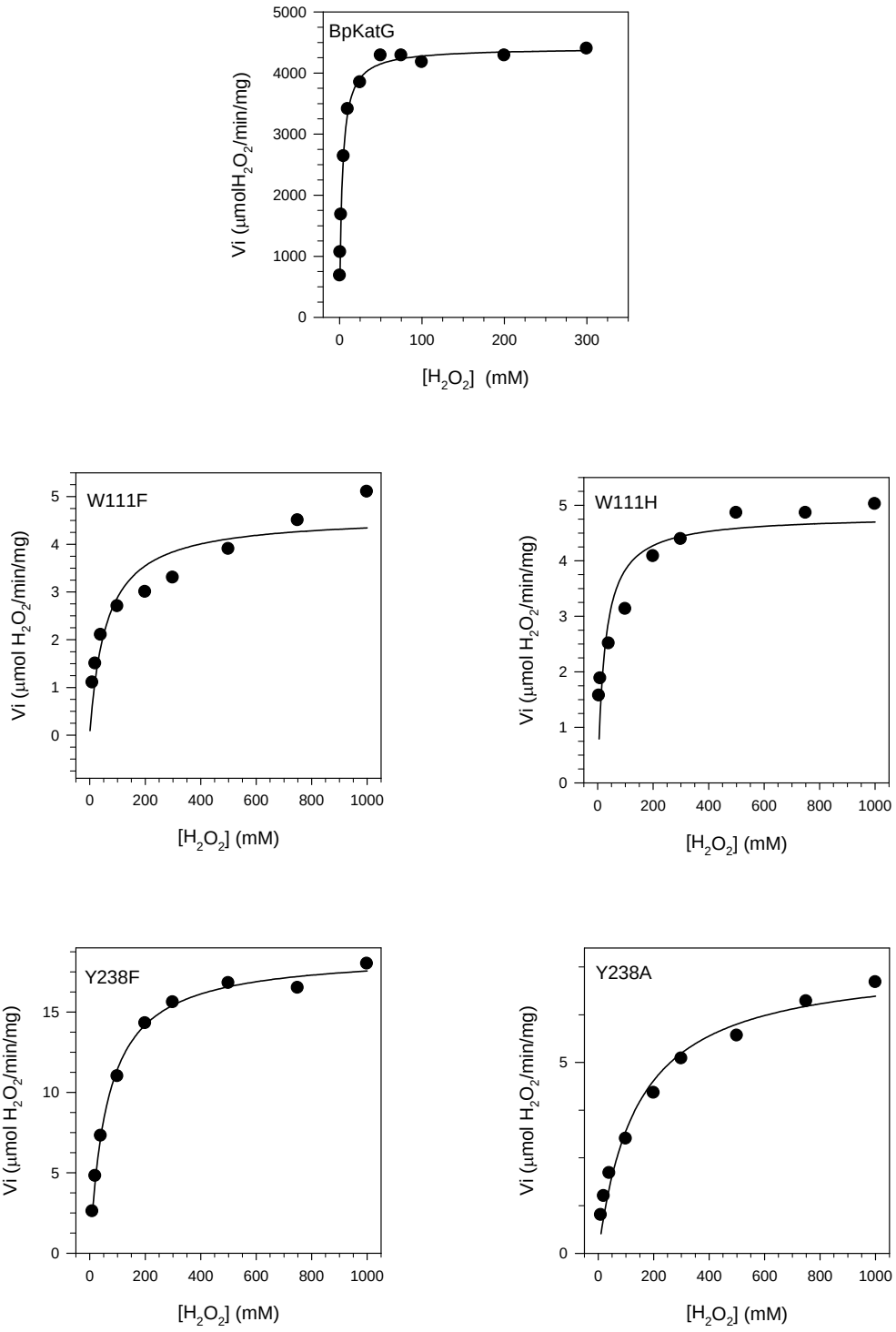

Figure 3.3. Effect of H_2O_2 concentration on the initial catalatic velocities of purified wild-type BpKatG and its variants. The solid line represents the best fit of the data to the Michaelis-Menten equation.

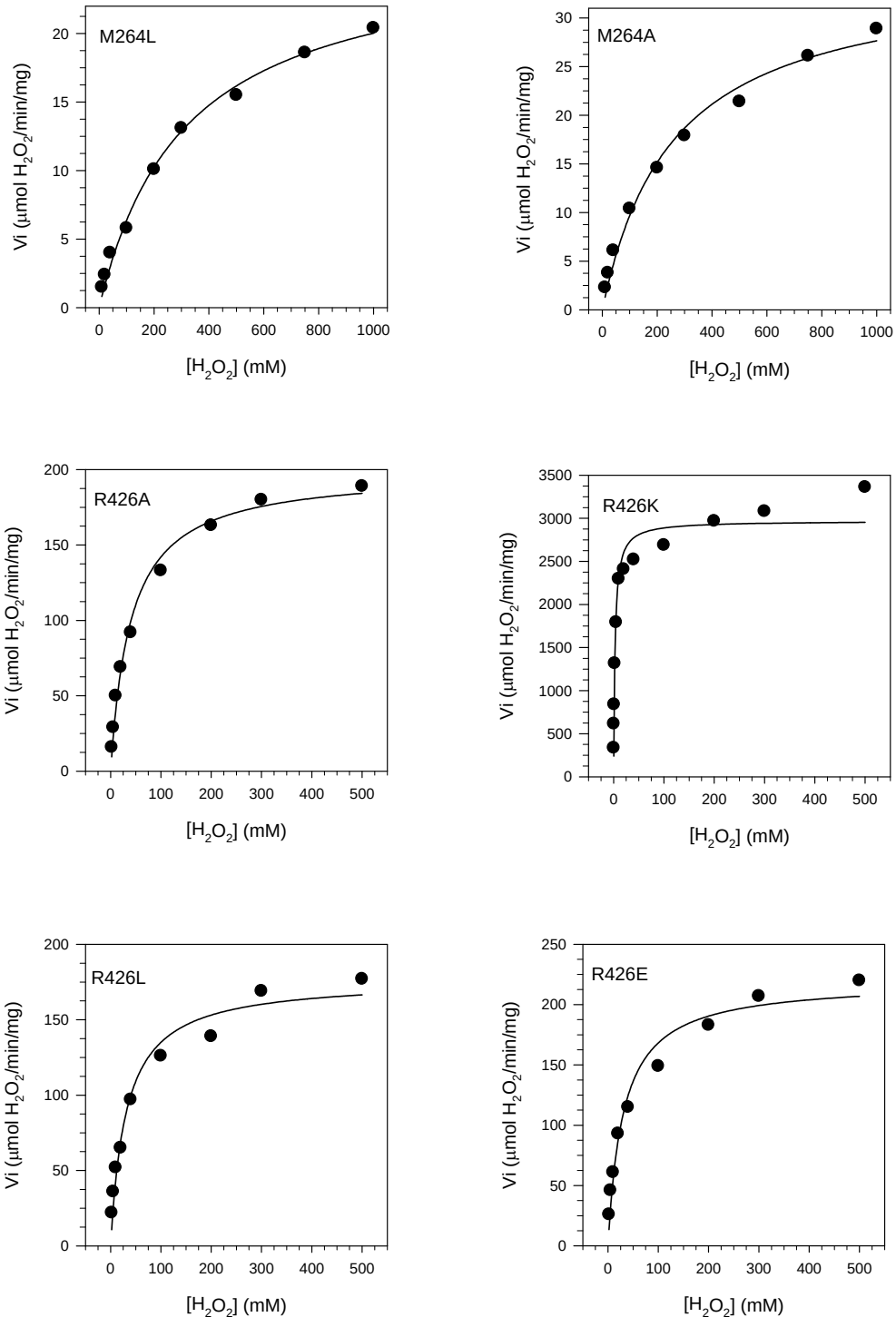

Figure 3.3. continued.

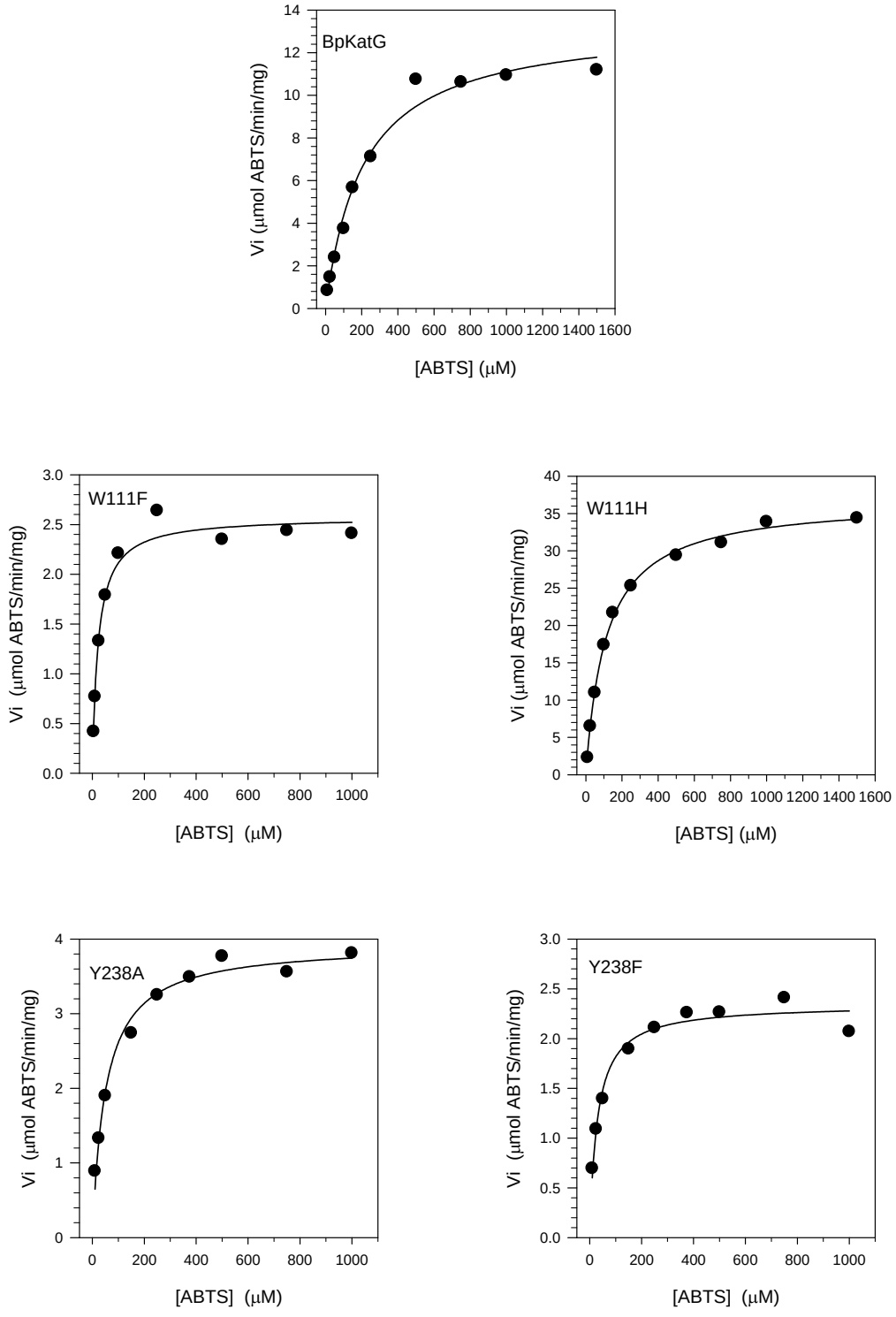

Figure 3.4. Effect of ABTS concentration on the initial peroxidatic velocities of purified wild-type BpKatG and its variants. The solid line represents the best fit of the data to the Michaelis-Menten equation.

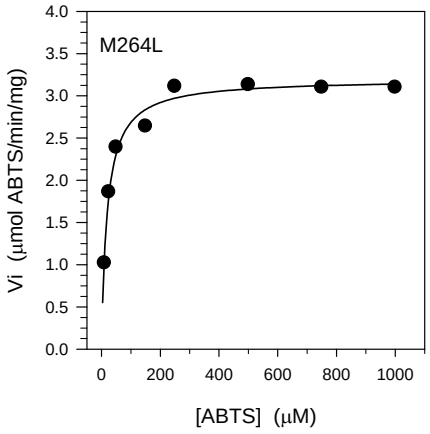

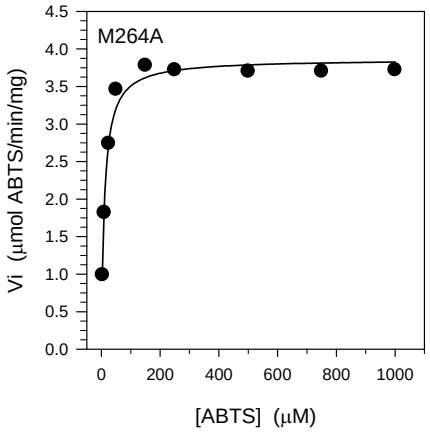

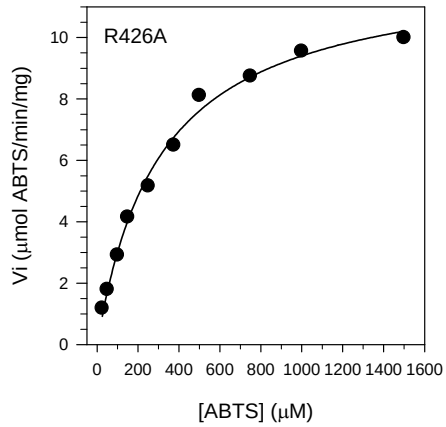

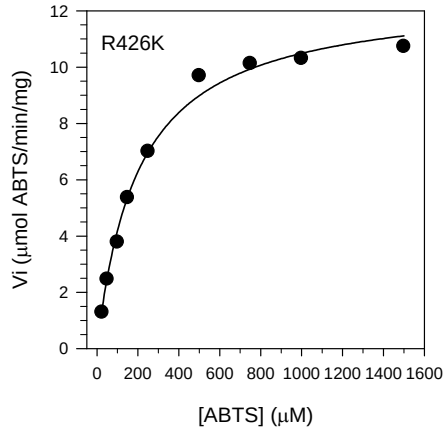

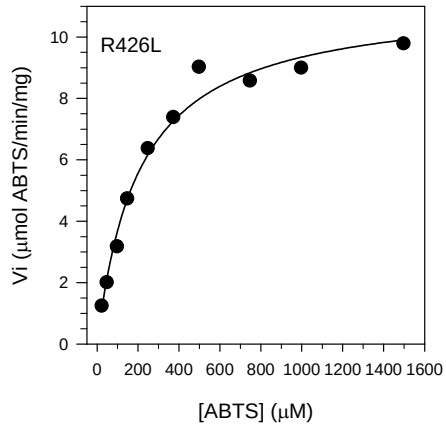

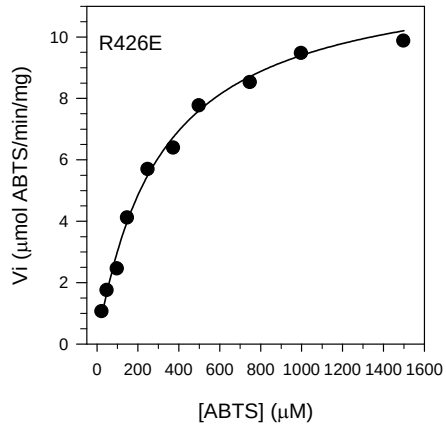

Figure 3.4. continued.

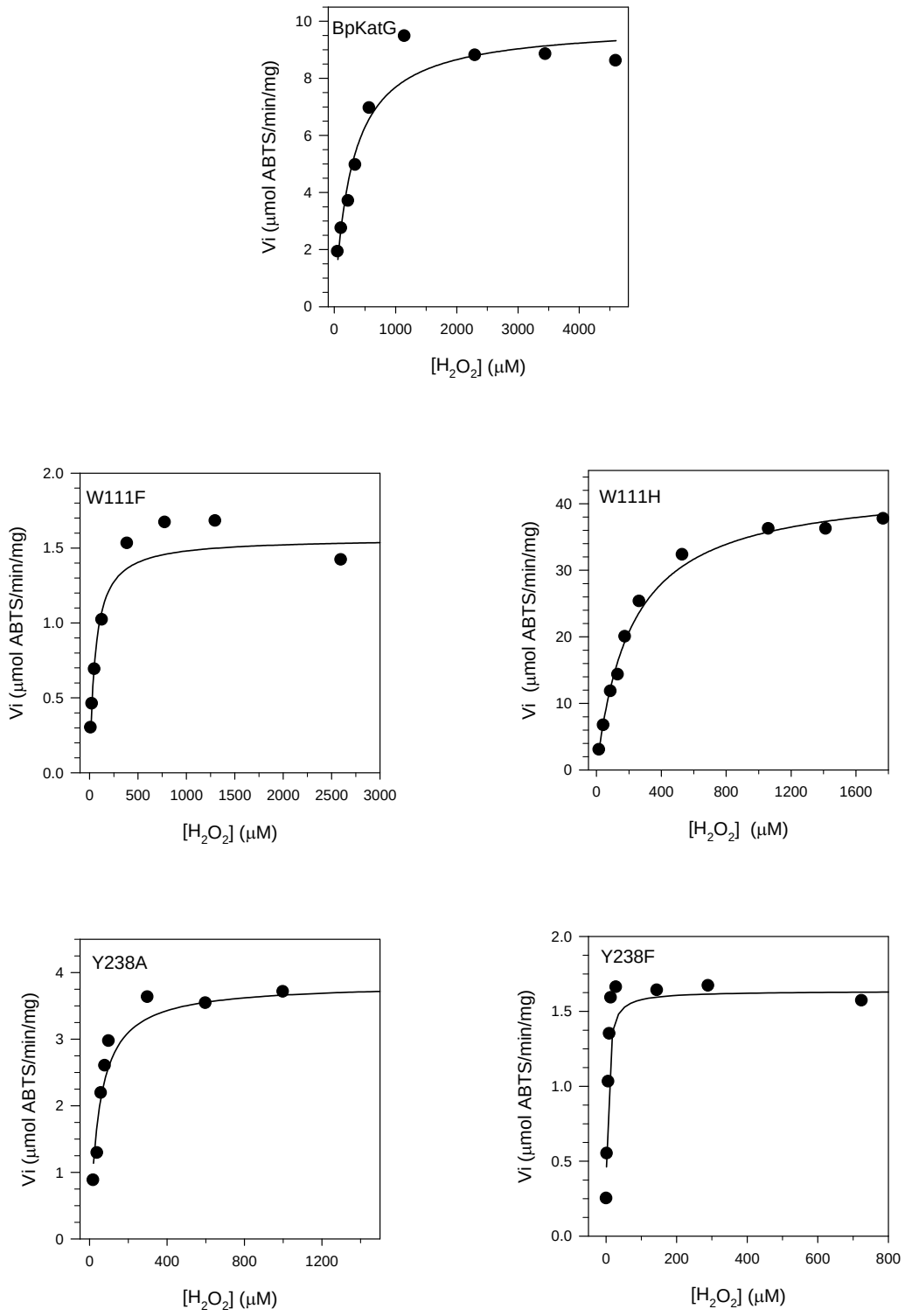

Figure 3.5. Effect of H_2O_2 concentration on the initial peroxidatic velocities of purified wild-type BpKatG and its variants. The solid line represents the best fit of the data to the Michaelis-Menten equation.

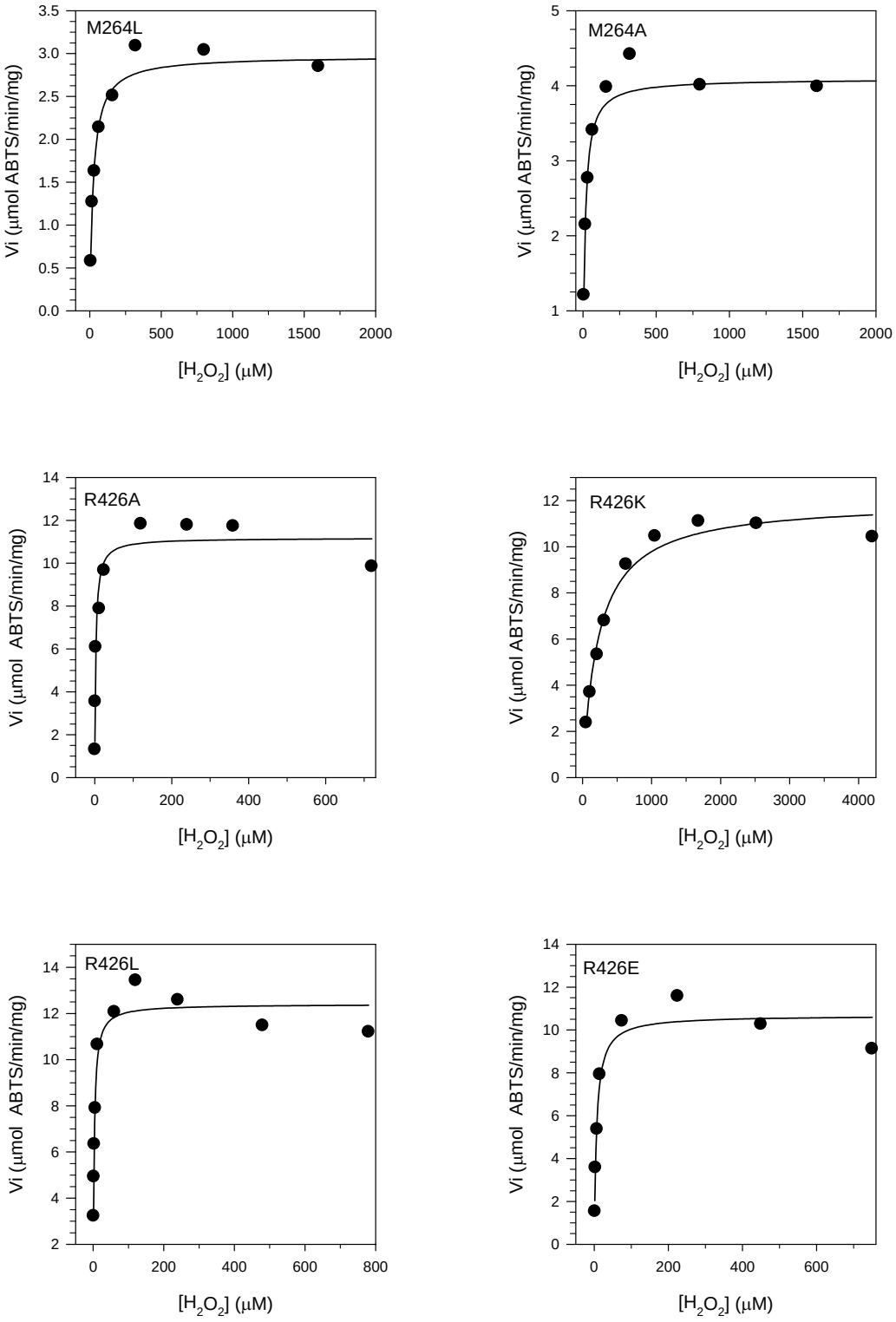

Figure 3.5. continued.

Table 3.3. The observed catalatic kinetic constants of purified BpKatG and its variants using H_2O_2 as a substrate.

Enzyme	**k_{cat} (sec^{-1})**	**K_M (app) (mM)**	**k_{cat}/K_M ($sec^{-1}M^{-1}$)**
wild-type	5700 ± 400	3.7 ± 0.9	1.5×10^6
W111F	6.0 ± 0.4	59 ± 20	1.0×10^2
W111H	6.3± 0.4	26 ± 8.7	2.4×10^2
Y238A	10.1 ± 0.5	140 ± 27	0.7×10^2
Y238F	24.7 ± 0.4	63 ± 4.2	3.9×10^2
M264A	46.0 ± 2.6	260 ± 41	1.7×10^2
M264L	35.0 ± 1.7	310 ± 40	1.1×10^2
R426A	240 ± 8.4	36 ± 1.7	6.8×10^3
R426E	280 ± 12	30 ± 2.5	9.4×10^3
R426K	3000 ± 300	3.3 ± 0.6	1.2×10^6
R426L	230 ± 7.4	30 ± 1.7	7.6×10^3

Table 3.4. The observed peroxidatic kinetic constants of purified BpKatG and its variants using ABTS as a substrate.

Enzyme	k_{cat} (sec^{-1})	K_M (app) (μM) H_2O_2	k_{cat}/K_M ($sec^{-1}M^{-1}$) H_2O_2	K_M (app) (μM) ABTS	k_{cat}/K_M ($sec^{-1}M^{-1}$) ABTS
wild-type	14.4 ± 1.8	310 ± 13	46 x 10^3	140 ± 5.0	100 x 10^3
W111F	3.3 ± 0.8	62 ± 2.9	52 x 10^3	19 ± 1.5	170 x 10^3
W111H	52.7 ± 2.2	220 ± 19	240 x 10^3	110 ± 5.6	460 x 10^3
Y238A	4.9 ± 2.2	3.9 ± 0.3	1200 x 10^3	45 ± 2.5	110 x 10^3
Y238F	2.9 ± 0.3	5.3 ± 0.3	550 x 10^3	27 ± 2.5	110 x 10^3
M264A	4.9 ± 0.4	16 ± 2.1	300 x 10^3	11 ± 1.0	440 x 10^3
M264L	4.1 ± 1.8	24 ± 4.7	170 x 10^3	20 ± 0.5	210 x 10^3
R426A	14.3 ± 1.8	2.5 ± 0.5	5700 x 10^3	200 ± 15	70 x 10^3
R426E	13.6 ± 1.1	7.5 ± 0.5	1800 x 10^3	200 ± 5.0	70 x 10^3
R426K	14.0 ± 0.5	190 ± 10	74 x 10^3	140 ± 5.8	100 x 10^3
R426L	14.5 ± 3.2	3.0 ± 0.5	4800 x 10^3	150 ± 8.7	100 x 10^3

least 1 order of magnitude. However, when Arg426 was replaced with a similarly positively charged residue lysine, values near the wild-type enzyme were retained.

The effects of ABTS concentration on the peroxidase reaction for wild-type BpKatG and its variants are shown in Fig. 3.4, with their kinetic constants summarized in Table 3.4. Changing any residues involved in the Met-Tyr-Trp cross-link resulted in a turn-over of approximately 35 % of the wild-type enzyme with about a 10-fold decrease in the K_M value for ABTS. Interestingly, the variant W111H had a turn-over of approximately 4 times greater and a K_M value only slightly lower than the wild-type enzyme. Changes to Arg426 had virtually no effect on the peroxidase turn-over compared to the wild-type enzyme with only a slight increase in the K_M value for ABTS being noticed for R426A and R426E.

Both the catalase and peroxidase reactions require hydrogen peroxide for the initial reaction to form compound I. In order to determine the effect of hydrogen peroxide on the peroxidase reaction, and thus the kinetic constants for compound I formation during the peroxidase reaction, initial velocities of peroxidase activity with ABTS were determined with varying concentrations of hydrogen peroxide. The results are shown in Fig. 3.5 and are summarized in Table 3.4. For the wild-type enzyme, the K_M for hydrogen peroxide for the peroxidase reaction is 310 μM, approximately 1 order of magnitude lower than the K_M value measured for the catalase reaction. Changes to any residues in the Met-Tyr-Trp cross-link or Arg426 resulted in a 10 to 100-fold decrease in the K_M for hydrogen peroxide and a 10 to 100-fold increase in the k_{cat}/K_M values. The

R426K and W111H variants maintained a K_M for hydrogen peroxide close to the wild-type enzyme value.

In summary, a general trend emerges: amino acid replacements of residues associated with the Met-Tyr-Trp cross-link result in variants that are virtually inactive and have a 10 to 100-fold increase in the K_M value for hydrogen peroxide in the catalase reaction and a 10 to 100-fold decrease in the K_M value for hydrogen peroxide in the peroxidase reaction with only slightly reduced peroxidase activity. The same trend is seen for variants of Arg426; they exhibit less than 5 % catalase activity with a 10-fold increase in the K_M value for hydrogen peroxide in the catalase reaction, and a 100-fold decrease in the K_M value for hydrogen peroxide for the peroxidase reaction with no affect on peroxidase turn-over. Near wild-type enzyme values are measured when Arg426 is replaced with a similar positively charged lysine.

3.3. Discussion

Catalase-peroxidases contain a peroxidase core that is very similar in both sequence and structure to monofunctional plant peroxidases. Unlike plant peroxidases however, KatGs are capable of performing the catalase reaction, and the structural basis for this activity has been the source of much debate. The recent success in crystallization and structure refinement has led to the identification of some catalase-specific features. Invariant to all class I plant peroxidases are the 3 active site residues on the distal side of the heme, including Arg108, Trp111, and His112 (BpKatG numbering is used throughout). However, specific to catalase-peroxidases is the unusual Met264-Tyr238-Trp111 adduct that

includes the conserved active site tryptophan, an arginine (Arg426) that is associated with Tyr238, and an aspartate (Asp141) located at the entrance to the heme active site.

Aided by the recent crystal structures, these catalase-specific features in KatGs have been the focus of several recent studies. Prior to the availability of these structures, the catalase-specific role of Trp111 was demonstrated (Hillar *et al*, 2000, and Regelsberger *et al*, 2000). Subsequently, changes to either the adjacent Tyr238 or Met264 involved in the adduct, and even Arg426 associated with Tyr238, inhibited the catalase reaction with little or no effect on the peroxidase reaction (Jakopitsch *et al*, 2003a and 2004, Yu *et al*, 2003b, and Singh *et al*, 2004). A mechanism attempting to explain how these residues impart catalase activity to a peroxidase core has been postulated (Mo *et al*, 2004), but is not compatible with recent data.

The crystal structure of BpKatG, crystallized at pH 5.6 revealed the Arg426 side chain adopting 2 conformations: 30 % in ionic association with Tyr238 (conformation Y) and 70 % flipped away from Tyr238 to a region containing 2 other arginine residues (conformation R) (Carpena *et al*, 2003b). Interestingly, the amount of the Y conformation varied from 0 % in MtKatG, crystallized at pH 4.5, to 80 % in SyKatG crystallized at pH 6.3 (Wada *et al*, 2002), and 100 % in HmKatG, crystallized at pH 8.0 (Yamada *et al*, 2002) suggesting a potential correlation between the position of this residue and pH. This apparent correlation was confirmed with crystals of native BpKatG containing less than 10 %, 30 %, 50 %, 75 %, and greater than 95 % Y

conformation of Arg426 when soaked at pH 4.5, 5.6, 6.5, 7.5, and 8.0 respectively prior to X-ray diffraction data collection (Carpena *et al*, 2005 and 2006) (Fig. 3.6). Also the apparent facile movement of Arg426 is consistent with the absence of any hindering residues in the cavity that may interfere with its movement (Fig. 3.6 D) and a switch-like movement is suggested from it being limited to just 2 conformations; providing the settings for the oxidation and reduction of the heme.

Crystals of BpKatG soaked with peroxoacetic acid to generate compound I prior to X-ray diffraction data collection show the continuous electron density extending from the heme iron consistent with the formation of an oxoferryl species (Carpena *et al*, 2005) and the side chain of Arg426 predominately adopting the R conformation (analogous to Fig. 3.6 A). Remarkably, even crystals soaked with peroxyacetic acid at pH 8.0 resulted in the oxoferryl species and Arg426 adopting the R conformation compared to it predominately adopting the Y conformation when crystals were soaked at that pH without peroxyacetic acid (Carpena *et al*, 2005). This strongly suggests that the conformation of the side chain of Arg426, though well removed from the heme, is sensitive to the oxidation state of the heme, and this must be modulated through the Met-Tyr-Trp adduct. By toggling between conformations R and Y, Arg426 is modulating inductive effects in the adduct, and because Trp111 is stacked 3.4 Å above ring II of the heme, also in the heme. Thus, when Arg426 is in conformation Y, associated with Tyr238, electrons in the adduct will be pulled towards the tyrosine effectively lowering electron density on Trp111 and the heme, thereby making heme oxidation more difficult, but reduction easier. Similarly, when Arg426 is in

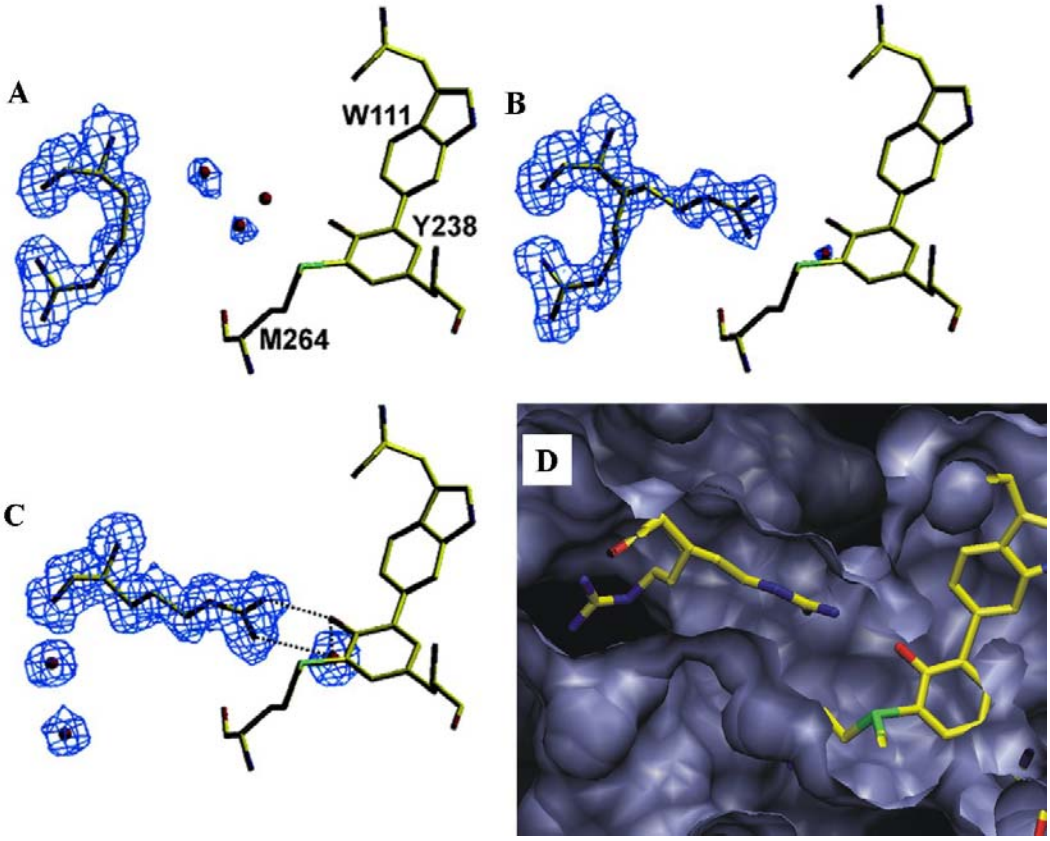

Figure 3.6. Change in the conformation of Arg426 with pH. The $2F_o - F_c$ electron density maps (blue mesh) are at $\sigma = 1.0$. Panel A: position at pH 4.5. Panel B: position at pH 6.5. Panel C: position at pH 8.5. Panel D: the cavity containing Arg426. Modified from Carpena *et al*, 2005 and 2006.

conformation R, flipped away from Tyr238, electrons will move away from the tyrosine towards Trp111 and the heme making oxidation easier but hindering compound I reduction (Fig. 3.7). The idea of Arg426 influencing heme reactivity is supported by changes in K_M values for H_2O_2 among variants of Arg426 and adduct residues (Tables 3.3 and 3.4). Replacing Arg426 with residues other than the similarly positively charged lysine result in a 100-fold decrease in the K_M for the H_2O_2 (Table 3.4) that is only used for compound I formation in the peroxidase reaction, a result of enhanced electron density on the heme that favours compound I formation. At the same time, the enhanced electron density on the heme hinders compound I reduction which is consistent with a 10-fold increase in the K_M for the H_2O_2 (Table 3.3) in the catalase reaction. The role of the adduct in combination with Arg426 is to modulate electron availability on the heme in such a way that the H_2O_2 can act as a reductant of compound I. As seen in the similar kinetic constants, disrupting the adduct by changing Trp111, Tyr238, or Met264 acts similarly to changing Arg426 itself, facilitating compound I formation and hindering its reduction. Thus, Arg426 acts as a molecular switch that favours compound I formation when toggled in the R conformation, away for Tyr238, and favours compound I reduction when toggled to the Y conformation, in association with Tyr238. A scheme depicting the resonance delocalization of electrons in the adduct under the influence of Arg426 is shown in Fig. 3.8. When Arg426 is in the Y conformation, electrons are pulled out of the indole ring of Trp111 resulting in a negative charge on the tyrosinate and when Arg426 is in the R conformation electrons are released and the electron density on the indole ring of Trp111 is

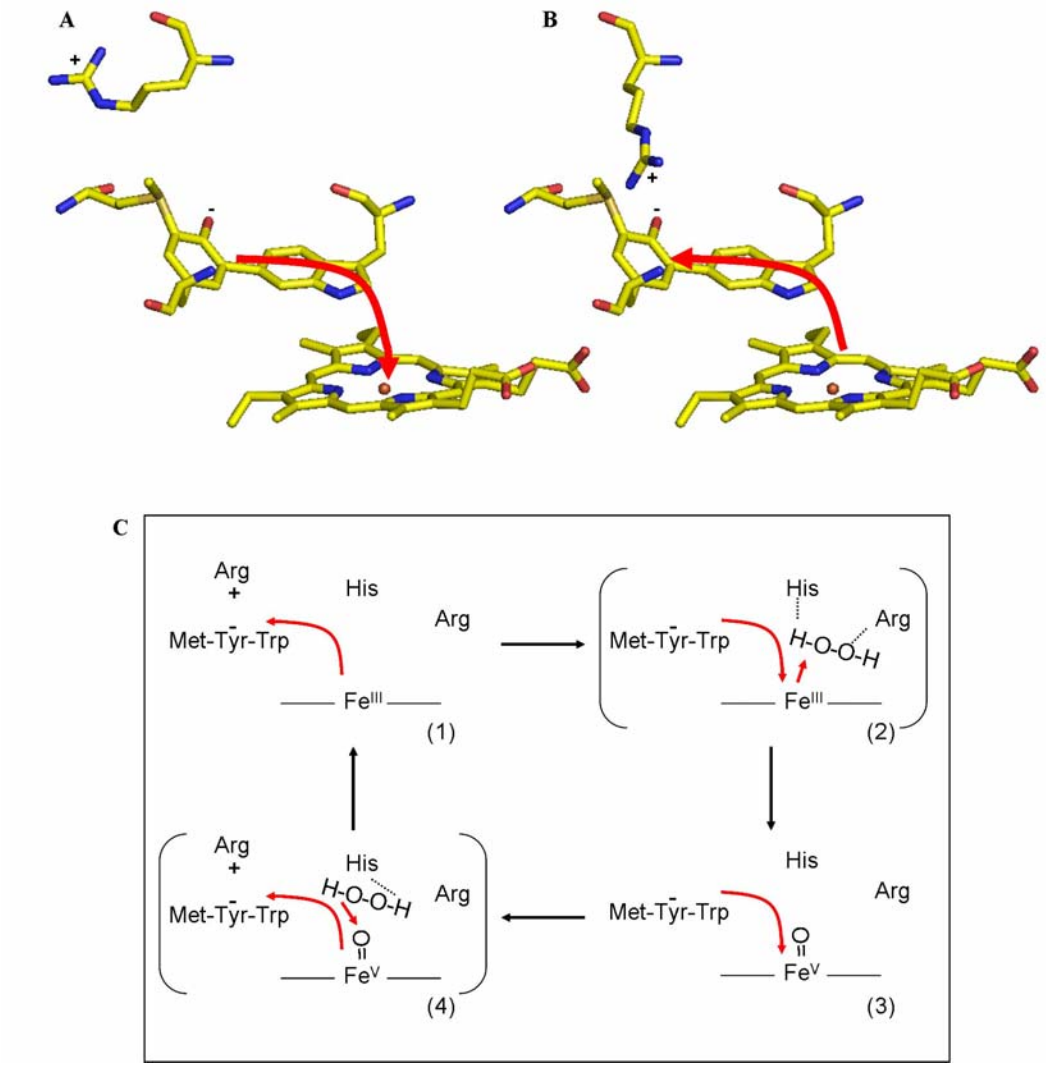

Figure 3.7. Scheme showing changes in electron flux in the cross-link and heme under the influence of Arg426. Panel A: conformation R. Panel B: conformation Y. Panel C: scheme describing the influence of electron flux on compound I formation and reduction for the catalase reaction. See text for details.

enhanced. This enhancement of electron density is also supported by unusual modifications to the active site of BpKatG, including a perhydroxy modification on the heme (Carpena *et al*, 2003b) and on the indole nitrogen of Trp111 in the variant S324T (Deemagarn *et al*, 2004a). Further support for this enhanced reactivity lies in the perhydroxy modification of the indole nitrogen of Trp111 which is also seen in crystals soaked at pH 8.5 (when Arg426 is predominately in the Y conformation) before X-ray data collection (Carpena *et al*, 2006). Thus these modifications of the BpKatG active site are consistent with there being an element of hyper-reactivity, which maybe modulated by the movement of Arg426.

Disruption of the adduct itself has a much more dramatic effect of rendering the enzyme completely catalase incompetent with less than 0.1 % activity being measured compared to the wild-type enzyme (Table 3.3). Even peroxidase activity, when measured at its optimum pH of 4.5 is reduced. This is likely due to a secondary effect of disruption to the KatG specific hydrogen bonding network when the adduct is disrupted (Santoni *et al*, 2004) and not a direct role in the peroxidase reaction itself. This could be supported by the kinetic constant k_{cat}/K_M for ABTS for all the variants of the adduct being nearly at wild-type enzyme levels even though the actual turn-over number is reduced suggesting that the adduct is not required for peroxidase activity. Additionally, when Trp111 is replaced with histidine, which possesses increased hydrogen-bonding capabilities, peroxidase activities with both ABTS and o-dianisidine are increased by a factor of 4 and 3, respectively, with still virtually no measureable

catalase activity (Table 3.2). In fact, the 5 % catalase activity detected for the Arg426 variants can be further rationalized by the positive charge of the methionine side chain of the adduct having a weak inductive effect (Fig 3.8). Mass spectral analysis has confirmed a completely formed adduct in variants of Arg426 (Jakopitsch *et al*, 2004, Ghiladi *et al*, 2005a and 2005b) and thus the positive charge on the methionine side chain of the adduct could be acting in a similar fashion to the arginine itself, but with a much weaker effect resulting in only 5 % activity.

The apparent correlation between the conformation of Arg426 and pH can also explain the characteristic pH optima for the peroxidase (pH 4.5) and catalase (pH 6.5) reactions (Dunford, 1999, and Singh *et al*, 2004) of KatGs. The peroxidase reaction, only requiring compound I formation with hydrogen peroxide is facilitated at acidic pH, where Arg426 in conformation R favours heme oxidation to compound I, but not its reduction. The catalase reaction, requiring both compound I formation and reduction with hydrogen peroxide is facilitated close to neutral pH where Arg426 in an apparent equilibrium between the R and Y conformations, allows both the formation and reduction of compound I with hydrogen peroxide. The neutral pH allows for optimal toggling of Arg426 between both conformations needed in the catalase reaction.

At physiological pH, Tyr238 most likely exists as a tyrosinate ion stabilized through the resonance charge delocalization in a zwitterion type structure with the adjacent positively charged sulfur of Met264 (Fig. 3.8). This suggests a much lower than normal pKa for Tyr238, explained at least in part by

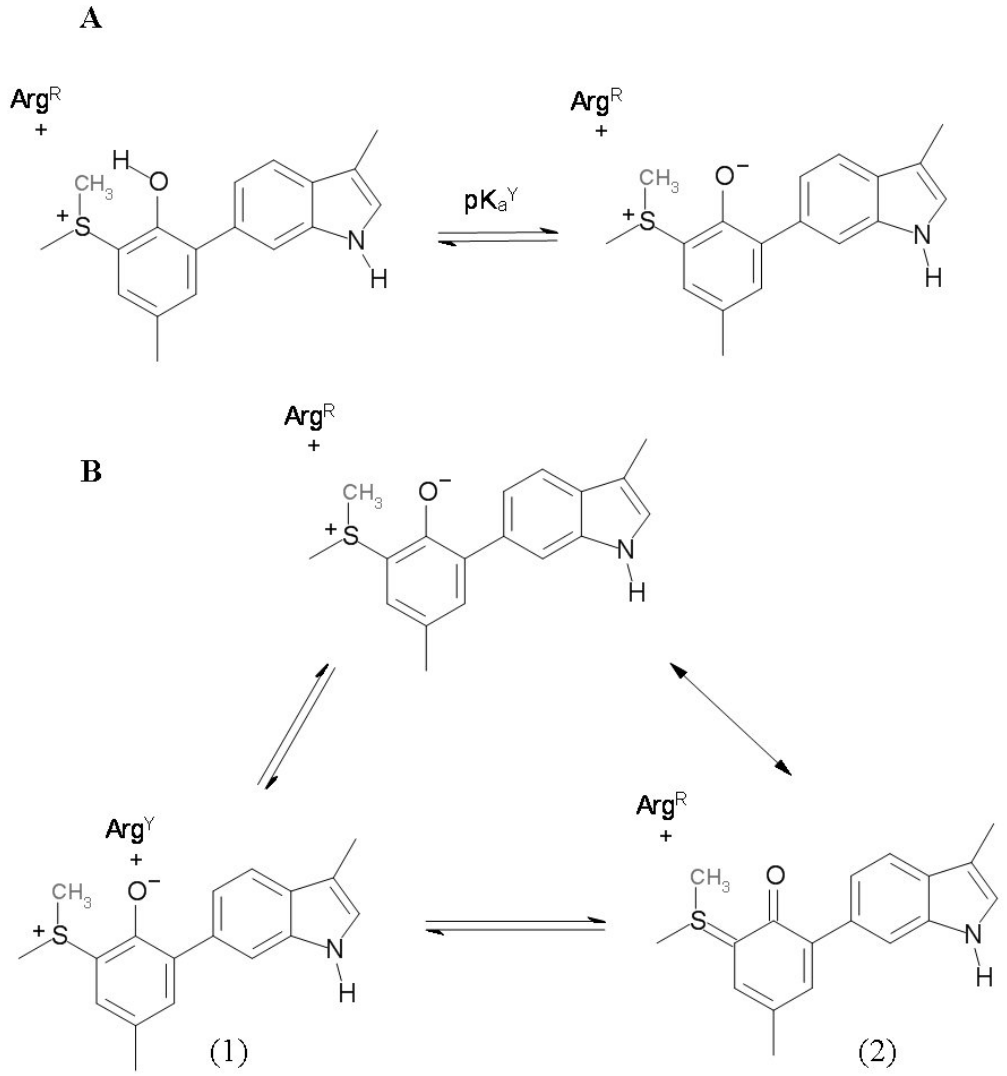

Figure 3.8. Scheme depicting the ionization of Tyr238 and possible resonance stabilization within the adduct. Panel A: ionization of Tyr238 at its pKa. Panel B: possible resonance stabilization within the adduct. (1) Arg426 is in the Y orientation lowering the electron density on Tyr-Trp. (2) Arg426 is in the R orientation increasing the electron density on Tyr-Trp. This figure was prepared using Symyx Draw 3.2. (www.symyx.com).

the delocalization of electrons to Met264 to reduce the negative charge on the tyrosinate oxygen and allow association of Arg426. This explanation is consistent with a recent quantum and molecular mechanics study on the electronic structure of compound I (Vidossich *et al*, 2007). The lower than normal pKa of Tyr238 is also reflected in the variants of Met264 that are completely catalase incompetent despite still containing the Tyr-Trp portion of the adduct (Jakopitsch *et al*, 2003b, Ghiladi *et al*, 2005a and 2005b). Although Arg426 is still present, it is no longer capable of association with Tyr238 as its pKa is now closer to that of a normal tyrosine, since delocalization of electrons with the sulfur of Met264 is no longer possible.

The lower pKa for Tyr238 places it in the same range as the other ionizable residue in the active site, the distal His112, whose pKa in the compound I of *Corinus cinereus* peroxidase is between 6 and 7, compared to 5 in the native state (Abelskov *et al*, 1997). This then allows for both hydrogen peroxide binding between His112 and Trp111, and Arg426 toggling to the Y conformation required for the catalase reaction to proceed. Other influences such as protein radical and peroxidatic substrate binding location overlay this to generate the final pH optima.

3.4. Conclusion

The switch like movement of Arg426 imparting inductive effects to the heme reaction centre through the Met-Tyr-Trp adduct can explain many aspects of the multifunctionality of catalase-peroxidases. This molecular switch can modulate the reactivity by shifting electrons into the active site and favouring oxidation to compound I when Arg426 is toggled in the R conformation, away for

Tyr238, and pulling electrons out of the active site and favouring compound I reduction when toggled to the Y conformation, in association with Tyr238. This can be seen in the reactivity towards hydrogen peroxide in variants of the Met264-Tyr238-Trp111 adduct and Arg426 itself. Disruption to the Met264-Tyr238-Trp111 adduct or removal of Arg426 via site-directed mutagenesis resulted in a 10 to 100-fold increase in the K_M value for hydrogen peroxide in the catalase reaction and a 10 to 100-fold decrease in the K_M value for hydrogen peroxide in the peroxidase reaction. The Arg426 is able to influence the heme reaction centre via ionic association with Tyr238 of the Met264-Tyr238-Trp111. This ionic association is made possible by a pKa for Tyr238 that is much closer to physiological pH than normally seen for a typical tyrosine residue.

In summary, as shown in Fig 3.7 C, the resting state active site with Arg426 in conformation Y polarizes electrons away from the active site towards Tyr238 (Fig 3.7 C(1)). As a molecule of hydrogen peroxide enters the active site Arg426 toggles towards conformation R allowing electron flux towards the heme, promoting oxidation to compound I (Fig 3.7 C(2 and 3)). Compound I forms via the Poulos-Kraut-like mechanism similar to monofunctional peroxidases with hydrogen peroxide binding between His112 and Arg108 (Hillar *et al*, 2000, and Regelsberger *et al*, 2000) or between His112 and Trp111 Deemagarn *et al*, 2007). Once compound I has formed (Fig 3.7 C(3)) a second molecule of hydrogen peroxide enters the active site, binds between His112 and Trp111 and Arg426 toggles to the Y conformation reducing electron density on the heme (Fig 3.7 C(4)) promoting compound I reduction back to the resting state. Independent of

the influences of Arg426, the incoming hydrogen peroxide is directed to either the His112-Arg108 or Trp111-His112 binding site by Asp141 for compound I formation and reduction (Deemagarn *et al*, 2007).

4. KINETIC AND SPECTRAL ANALYSIS OF THE REACTION BETWEEN BPKATG AND PEROXYACETIC ACID

4.1. Introduction

The reaction cycles of both catalases and peroxidases share a common first step with the oxidation of the heme to form an oxyferryl porphyrin cation radical species, $Por^{\bullet+}\ Fe^{IV}=O$, commonly called compound I. Catalases then utilize a second molecule of hydrogen peroxide in the catalase reaction as a 2 electron donor in the second step to reduce the $Por^{\bullet+}\ Fe^{IV}=O$ back to the ferric resting state with the release of molecular oxygen and water. Peroxidases on the other hand utilize 1-electron organic electron donors in 2 sequential reduction steps, passing through a second intermediate known as compound II, to reduce compound I back to the resting state. Peroxidases such as ascorbate peroxidase (Patterson *et al*, 1995) and horseradish peroxidase (Veitch, 2004) and the majority of monofunctional catalases form the $Por^{\bullet+}\ Fe^{IV}=O$ upon oxidation to compound I (Nicholls *et al*, 2001). However, in some monofunctional peroxidases such as cytochrome *c* peroxidase (Sivaraja *et al*, 1989) and lignin peroxidase (Blodig *et al*, 1999) an alternate compound I is formed via intramolecular electron transfer between the porphyrin and a tryptophan within the protein to generate a tryptophan based radical ($Por\ Fe^{IV}=O\ Trp^{\bullet+}$). These radical locations generally correlate with the binding site of the reducing substrate. For example, in the case of cytochrome *c* peroxidase, the reducing substrate is another protein cytochrome *c*, that binds on the surface in close proximity to the Trp191 the location of the protein based radical (Sivaraja *et al*, 1989). In the case of ascorbate peroxidase

and monofunctional catalases, the reducing substrates ascorbate and hydrogen peroxide, respectively, react directly with the heme, bypassing the need for any protein based radicals (Patterson *et al*, 1995, and Nichols *et al*, 2001). Catalase-peroxidases, as their name implies are capable of behaving as catalases in the presence of only hydrogen peroxide or as peroxidases when also in the presence of available organic reducing substrates and thus, not surprisingly, have been shown to utilize both porphyrin and protein based radicals (Singh *et al*, 2007).

While hydrogen peroxide is the natural oxidizing substrate, other organic peroxyacids such a peroxyacetic and 3-chloroperoxybenzoic acid can also oxidize the heme to form compound I, and are often substituted in place of hydrogen peroxide to avoid its overwhelming catalase activity in order to trap and study the reaction intermediates. The reaction intermediates of peroxidases and KatG have characteristic UV-visible spectra that make possible their identification, and several studies have focused on the reaction of KatGs with various oxidizing agents with the object of understanding the reaction pathway on a millisecond timescale (see Smulevish *et al*, 2006 for a review).

The most common spectral feature upon reaction with an oxidizing substrate such as peroxyacetic acid is a decrease in intensity of the Soret band accompanied by changes in the charge transfer bands, consistent with the rapid, 1-step formation of $Por^{\bullet+}$ Fe^{IV}=O and other oxoferryl species (Smulevich *et al*, 2006). However, there has been a report of a 2-step process in MtKatG involving an initial species exhibiting a marked increase in the Soret band and a 10 nm shift of the ferric charge transfer bands (Ghiladi *et al*, 2005a). This 2-step pathway

was rationalized by the first species being a highly unusual ferric heme with an amino acid radical (Fe^{III} $AA^{\bullet}$, compound II), followed by the formation of a $Por^{\bullet+}$ Fe^{IV}=O $AA^{\bullet}$ species. A similar 2-step reaction has also been reported for the KatG from *Burkholderia pseudmallei* upon treatment with peroxyacetic acid (Jakopistch *et al*, 2007), but other than the initial observation of an intermediate preceding the formation of compound I, the identity and kinetics of formation were not addressed.

4.2. Results

4.2.1. Purification and characterization of BpKatG and W330F

BpKatG and the variant of the proximal active site tryptophan, W330F were purified as outlined in the material and methods and analyzed by SDS-PAGE as shown in Fig. 4.1. They both have similar electrophoretic mobility and a predominant band with an apparent molecular mass of roughly 79 kDa. The larger bands at approximately 160 kDa and higher are most likely dimer and larger aggregates which are not reduced with either β-mercaptoethanol or dithiothreitol added to the sample buffer.

Fig. 4.2 compares the resting ferric absorption spectra and the resulting spectra approximately 30 seconds after the addition of a 10-fold excess of peroxyacetic acid to the purified wild-type enzyme and W330F, and Table 4.1 summarizes the positions of the absorption maxima and heme to protein ratios ($A_{407/280}$) in the ferric resting enzymes. As shown in Fig. 4.2 (solid trace), the resting state of both the wild-type enzyme and the W330F variant show the characteristic spectra of a ferric enzyme with the Soret and charge transfer (CT)

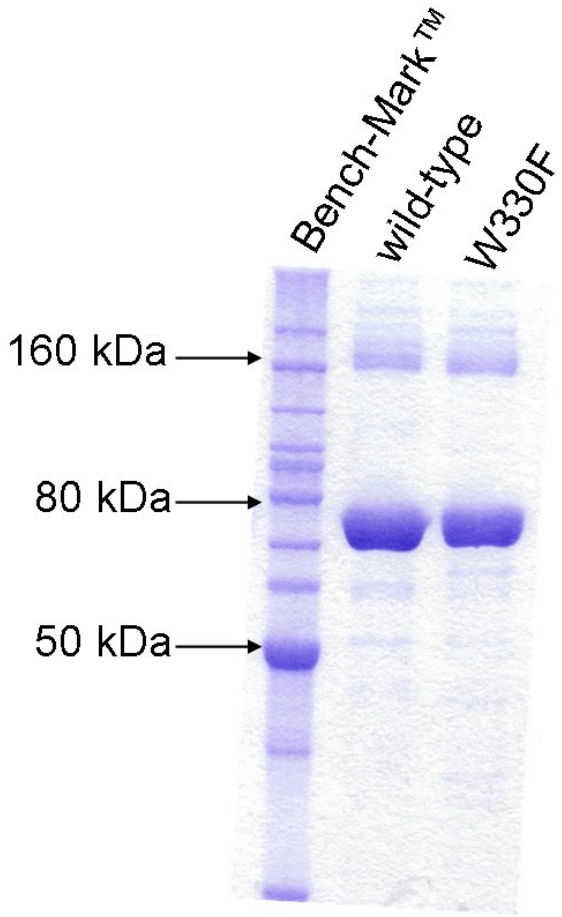

Figure 4.1. SDS-polyacrylamide gel electrophoretic analysis of purified wild-type BpKatG and W330F. Approximately 3.0 μg of protein were separated on an 8 % polyacrylamide gel and stained with Coomassie brilliant blue.

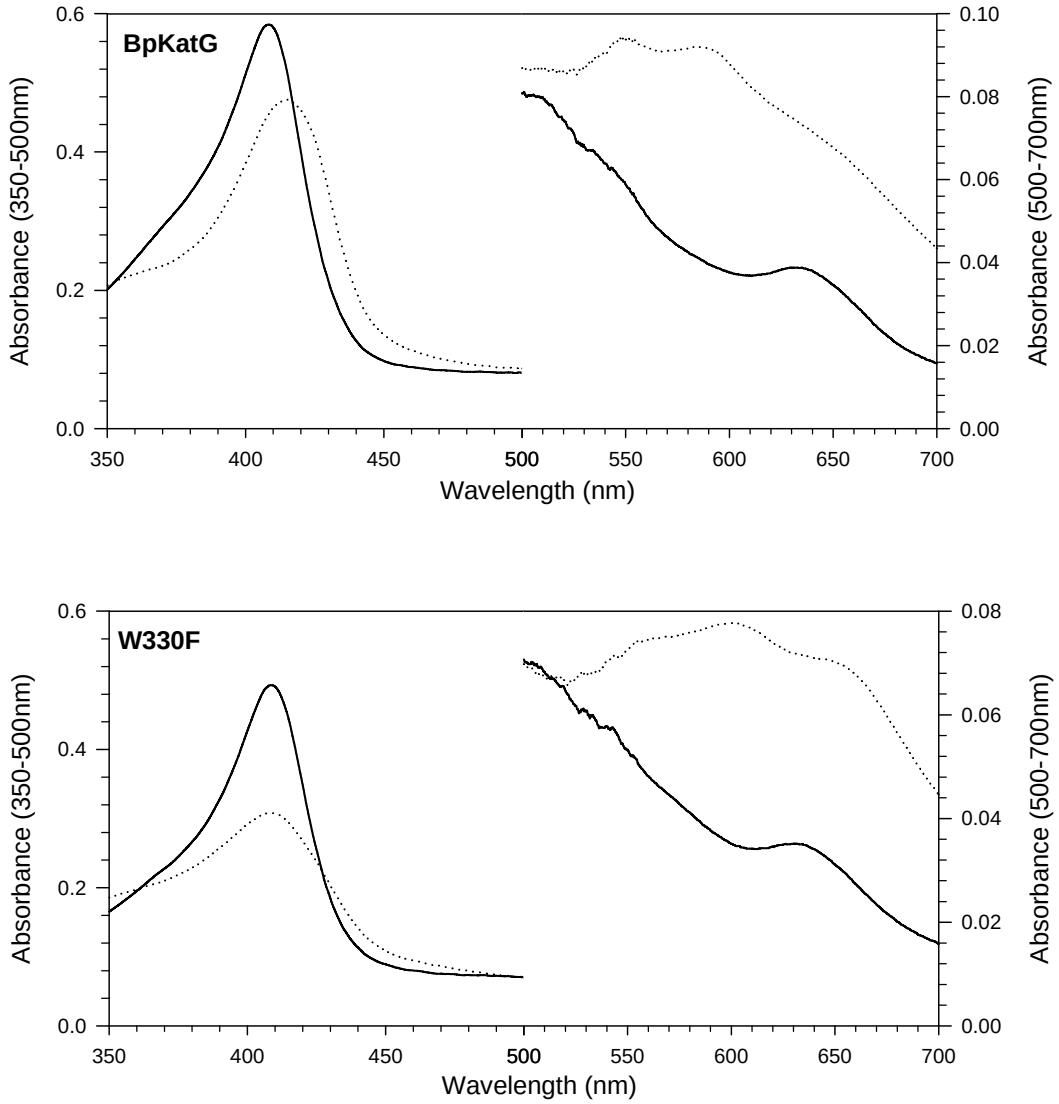

Figure 4.2. Manually mixed absorption spectra of purified wild-type BpKatG and W330F in 50 mM potassium phosphate buffer, pH 7.0. Solid line represents ferric resting-state and dotted line represents resulting spectra approximately 30 seconds after treatment with a 10-fold excess of peroxyacetic acid.

band at 407 and 635 nm respectively. In the case of the wild-type enzyme, the resulting spectrum after addition of peroxyacetic acid (Fig. 4.2 (dotted trace)) resulted in a 20 % decrease in absorbance, a slight broadening and shift to 415 nm of the Soret, and the concomitant appearance of 2 bands at 545 and 585 nm consistent with an oxoferryl intermediate, but not a typical porphyrin cation radical Compound I. By contrast, the spectra resulting from the addition of peroxyacetic acid to W330F showed the characteristic spectral features of a $Por^{\bullet+}$ Fe^{IV}=O species with a marked decrease in the absorbance (roughly 40 %), of the Soret with virtually no shift, and the concomitant appearance of a strong broad band around 655 nm, features typical of a porphyrin cation radical.

Table 4.2 summarizes the catalase and peroxidase activities of the wild-type enzyme and W330F. Remarkably, despite the difference in the oxoferryl intermediate of W330F compared to the wild-type enzyme, the catalase and peroxidase activities are very similar with the W330F catalase activity being 70 % of wild-type enzyme levels and the peroxidase activity being 50 % and 70 % of wild-type enzyme levels when measured with ABTS and o-dianisidine respectively.

4.2.2. Steady-state kinetic characterization of BpKatG and W330F

Kinetic parameters for the reactions catalyzed by both the catalase and peroxidase reactions were determined using the program SigmaPlot (Systat Software Inc.) by fitting initial velocities at varying substrate concentrations to the Michaelis-Menten equation using non-linear regression. The effects of hydrogen

Table 4.1. Observed optical absorbance maxima and $A_{407/280}$ ratio for purified wild-type BpKatG and W330F.

Enzyme	Soret maximum (nm)	$A_{407/280}$ ratio[a]	% Heme Occupancy[b]
wild-type	407	0.62	86.1
W330F	407	0.64	88.9

[a]The theoretical $A_{407/280}$ ratio is 0.72.
[b]Based on the theoretical $A_{407/280}$ maximum of 0.72.
ε at 280 nm is calculated based on ε_{Trp} = 5500 $M^{-1}cm^{-1}$ and ε_{Tyr} = 1490 $M^{-1}cm^{-1}$ and for the heme at 407 nm ε = 100,000 $M^{-1}cm^{-1}$.

Table 4.2. Catalase and Peroxidase activities of purified BpKatG and W330F.

Enzyme	Catalase[a]	Peroxidase	
		ABTS[b]	o-dianisidine[c]
wild-type	4300 ± 300	10.9 ± 1.4	8.0 ± 0.5
W330F	2900 ± 180	5.7 ± 0.2	5.6 ± 0.4

[a]Expressed as μmole H_2O_2•min^{-1}•mg^{-1} metabolized.
[b]Expressed as μmole ABTS•min^{-1}•mg^{-1} reduced.
[c]Expressed as μmole o-dianisidine•min^{-1}•mg^{-1} reduced.

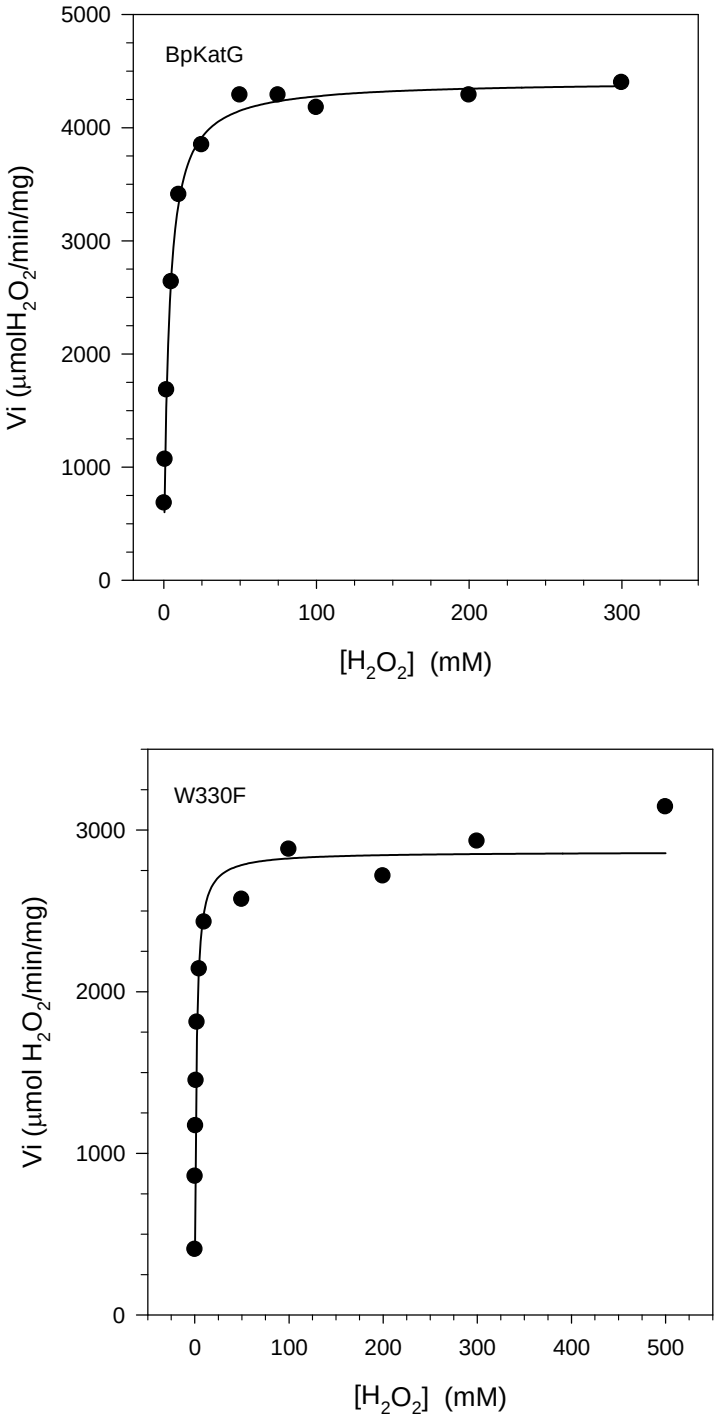

Figure 4.3. Effect of H_2O_2 concentration on the initial catalatic velocities of purified wild-type BpKatG and W330F. The solid line represents the best fit of the data to the Michaelis-Menten equation.

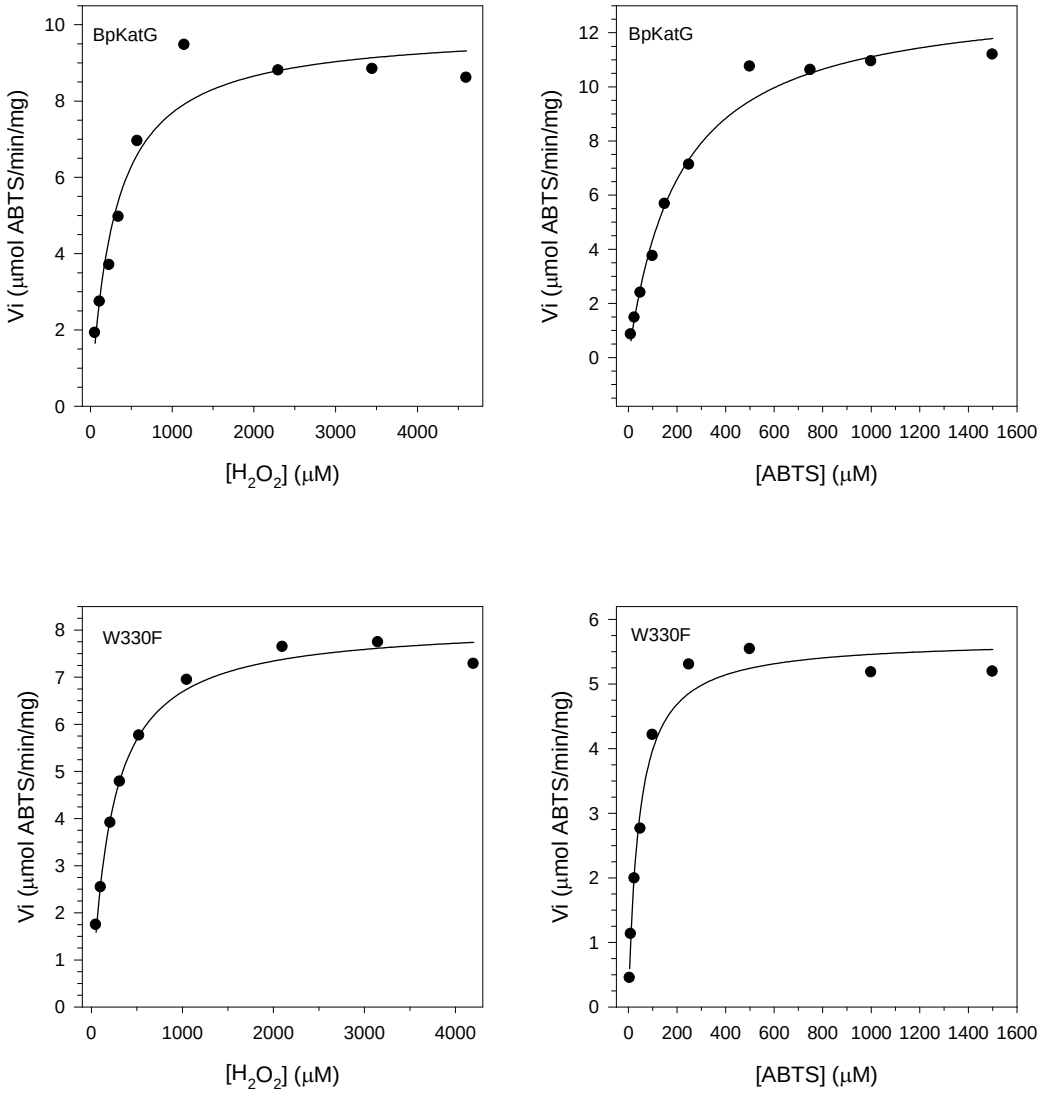

Figure 4.4. Effect of H_2O_2 and ABTS concentration on the initial peroxidatic velocities of purified wild-type BpKatG and W330F. The solid line represents the best fit of the data to the Michaelis-Menten equation.

Table 4.3. The observed catalatic kinetic constants of purified BpKatG and W330F using H_2O_2 as a substrate.

Enzyme	**k_{cat} (sec^{-1})**	**K_M (app) (mM)**	**k_{cat}/K_M ($sec^{-1}M^{-1}$)**
wild-type	5700 ± 400	3.7 ± 0.9	1.5×10^6
W330F	3800 ± 240	1.5 ± 0.2	2.5×10^6

Table 4.4. The observed peroxidatic kinetic constants of purified BpKatG and W330F using ABTS as a substrate.

Enzyme	**k_{cat} (sec^{-1})**	**K_M (app) (µM) H_2O_2**	**k_{cat}/K_M ($sec^{-1}M^{-1}$) H_2O_2**	**K_M (app) (µM) ABTS**	**k_{cat}/K_M ($sec^{-1}M^{-1}$) ABTS**
wild-type	14.4 ± 1.8	310 ± 13	46×10^3	140 ± 5.0	100×10^3
W330F	7.5 ± 0.3	220 ± 18	34×10^3	43 ± 6.6	180×10^3

peroxide concentration on the catalase reaction for the wild-type enzyme and W330F are shown in Fig. 4.3, with the kinetic constants summarized in Table 4.3. As shown in Table 4.3, changing Trp330 to the non-oxidizable phenylalanine had virtually no effect on the enzyme's affinity for hydrogen peroxide in the catalase reaction as the K_M value was only marginally decreased compared to the wild-type enzyme and there was only a 30 % reduction in turnover rate. The effects of ABTS and hydrogen peroxide concentration on the peroxidase reaction for the wild-type enzyme and W330F are shown in Fig. 4.3, with the kinetic constants summarized in Table 4.4. Similar to the catalase reaction, the K_M for hydrogen peroxide for the peroxidase reaction for W330F was only slightly decreased compared to the wild-type enzyme, and this was accompanied by a 50 % reduction in peroxidase turnover rate. The K_M value for ABTS, on the other hand, was reduced to approximately 40 μM in W330F compared to 140 μM in the wild-type enzyme.

4.2.3. Stopped-flow UV-visible absorption characterization of the reaction of BpKatG with peroxyacetic acid

Fig. 4.5 shows the changes in the absorption spectrum of wild-type BpKatG at pH 7.0 upon reaction with a 50-fold excess of peroxyacetic acid as a function of time. The resting enzyme shows the Soret band at 407 nm and the charge transfer band at 635 nm typical of a ferric oxidation state. After mixing with peroxyacetic acid, an initial 10 % increase in the absorbance and narrowing of the Soret band with the concomitant shift of the charge transfer band to 625 nm are observed within 30 ms (Fig. 4.5, panel A, red traces). After 400 ms, the Soret

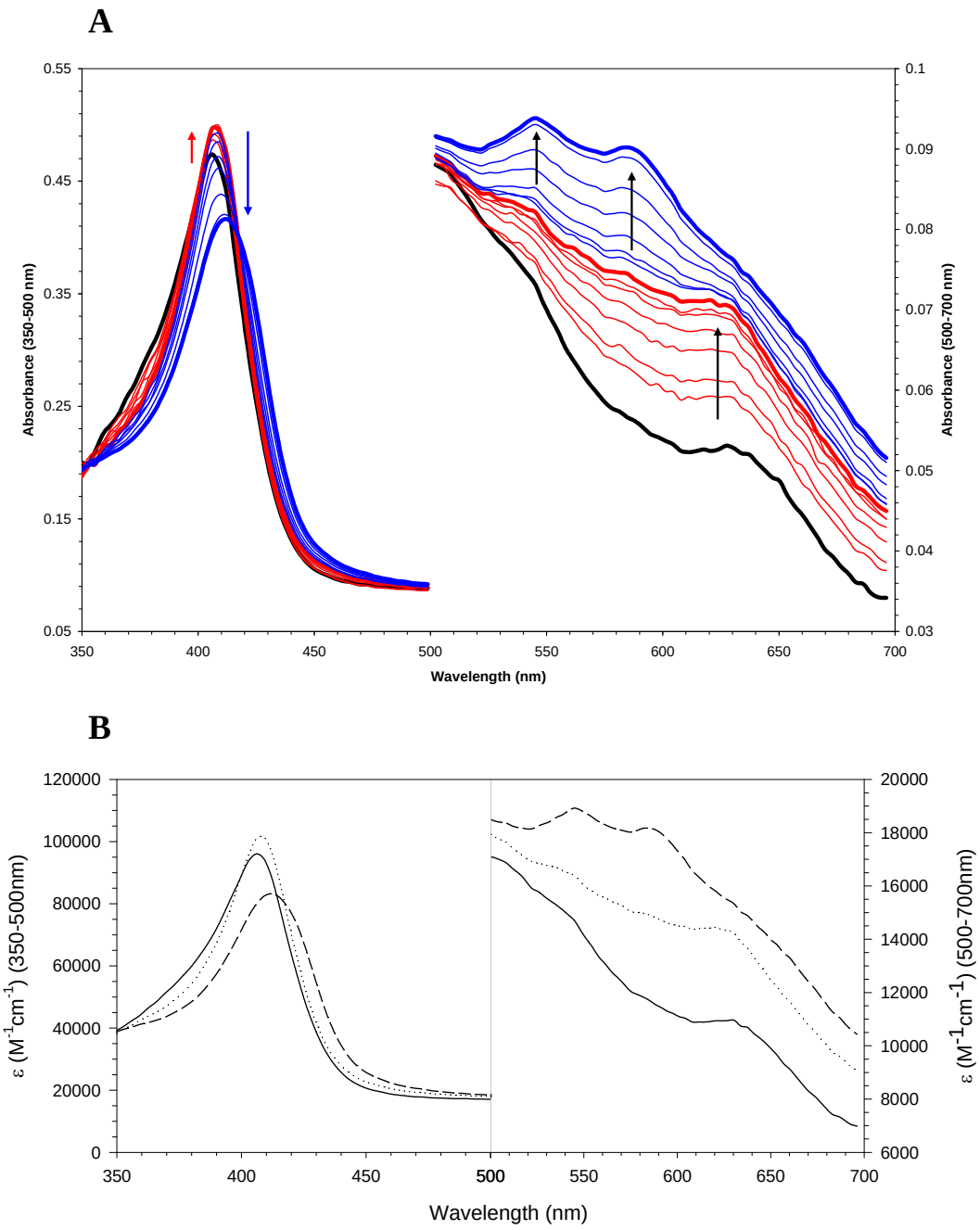

Figure 4.5. Rapid-scan absorption spectra of the reaction of wild-type BpKatG mixed with a 50-fold excess of peroxyacetic acid at pH 7.0. Panel A: the bold black trace represents the first spectrum acquired (1.3 msec) after mixing. The red spectra (at 14, 30, 50, 75, 100, 125, and 150 msec after mixing) reveal an initial 10 % increase and narrowing in the Soret, before transition to the oxoferryl-like spectra (blue spectra at 250 msec, 400 msec, 1 sec, 2 sec, 5 sec, and 10 sec after mixing). Panel B: the resulting fitted absorption spectra. The model consists of ferric enzyme (solid line) followed by a rapidly formed ferric-like Species X (dotted line), followed by the formation of compound I (dashed line).

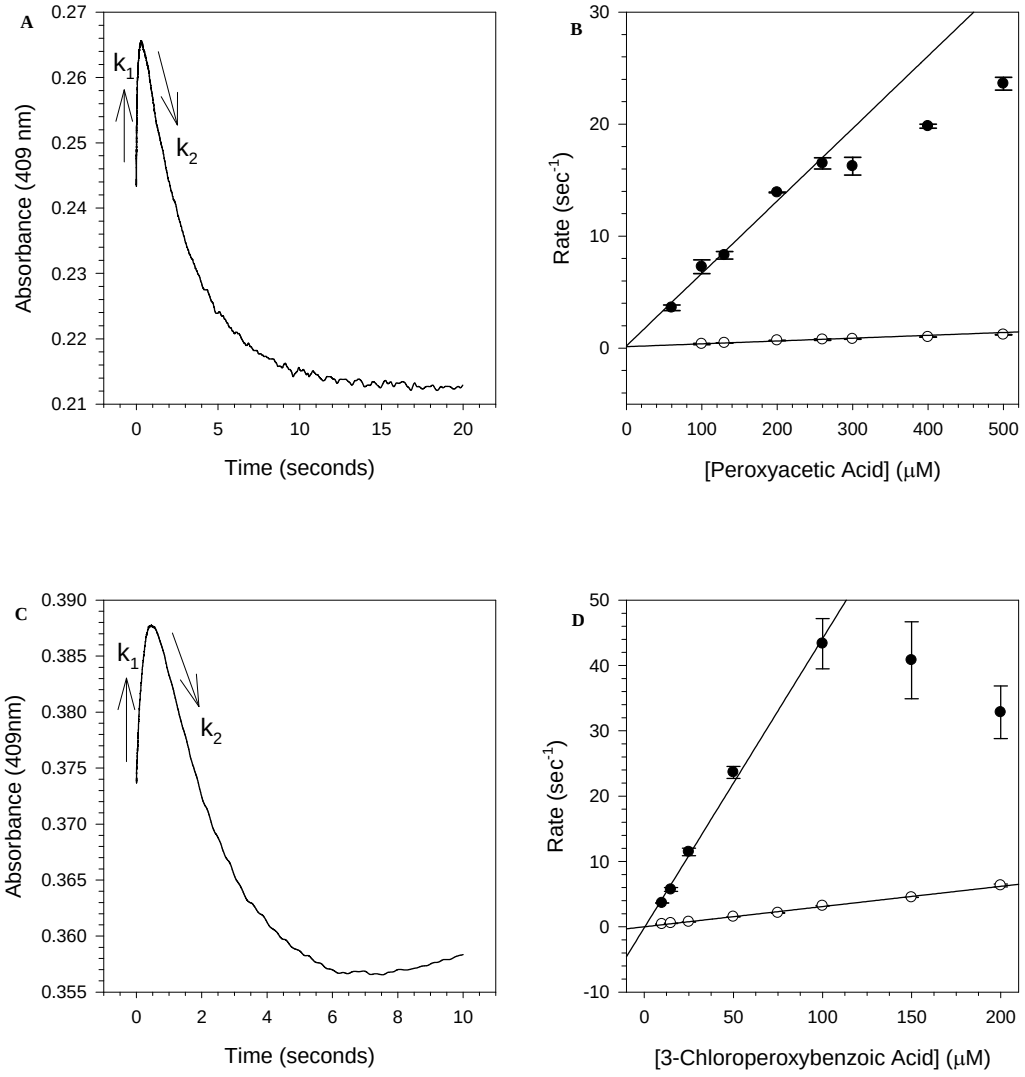

Figure 4.6. Change in absorbance at 409 nm for the reaction of wild-type BpKatG with peroxyacetic acid (Panel A) and 3-chloroperoxybenzoic acid (Panel C) with time. Peroxyacetic acid (Panel B) and 3-chloroperoxybenzoic acid (Panel D) dependence of the transition rates k_1 (closed circles) and k_2 (open circles).

band begins to shift 415 nm with a concomitant 35 % decrease in absorbance (or a 25 % decrease with respect to the resting enzyme) and concomitant appearance of 2 bands at 545 and 585 nm (Fig. 4.5, panel A, blue traces) and a broad ill-defined shoulder around 655 nm.

Spectral analysis of the rapid-scan absorption spectrum of the reaction between BpKatG and a 50-fold excess of peroxyacetic acid produced a good fit to experimental data when using a 3 species, 2 rate model (Fig. 4.5, panel B). This model consists of the resting state enzyme (Fig. 4.5, panel B, solid trace) first transitioning to Species X (Fig. 4.5, panel B, dotted trace) with a rate (k_1) estimated to be 17 sec^{-1}. Species X clearly differs from the ferric resting state with an increase in intensity of the Soret band and a 10 nm blue shift of the charge transfer band to 625 nm. Subsequently, species X then transitions to compound I (Fig. 4.5, panel B, dashed trace) with a rate (k_2) estimated to be 1 sec^{-1}. The spectrum of compound I consists of the Soret band shifted to 415 nm with a 25 % decrease in intensity, and 2 bands at 545 and 585 nm consistent with an oxoferryl-like intermediate.

To further investigate the order of the reaction for the formation of species X and compound I, the concentration of peroxyacetic acid was increased over a range of 50 to 500 μM. The reaction rates k_1 and k_2 for the transition of ferric → species X, and species X → compound I were determined by monitoring the change in absorbance at 409 nm as a function of peroxyacetic acid and fitting it to a double exponential equation as shown in Fig. 4.6, panels A and B. The initial fast step corresponding to an increase in absorbance at 409 nm and subsequent

decrease in absorbance are clearly evident. Summarized in Table 4.5, the initial ferric to species X transition (k_1 = 6.47 x 10^4 $M^{-1}sec^{-1}$) is roughly 10-fold faster then the transition of species X to compound I (k_2 = 2.5 x 10^3 $M^{-1}sec^{-1}$). The same spectral changes and order of reaction were also observed with 3-chloroperoxybenzoic acid (Fig. 4.6, panels C and D) but with reaction rates for k_1 and k_2 roughly 10 times faster (Table 4.5). Surprisingly, both rates show a linear dependence on peroxyacetic or 3-chloroperoxybenzoic acid (Fig. 4.6, panel B and D) suggesting that 2 separate peroxyacetic acid (or 3-chloroperoxybenzoic acid) related events are required for the formation of the oxoferryl species compound I. The fact that there were only subtle changes to the spectrum of Species X compared to the ferric spectrum suggests that the heme iron is still in the ferric oxidation state, with only small changes in the iron coordination.

4.2.4. Influence of specific mutations on the reaction of BpKatG with peroxyacetic acid as monitored by stopped-flow UV-visible absorption spectroscopy

Replacement of the proximal tryptophan (Trp330) in BpKatG resulted in a number of subtle changes that are evident in the kinetic parameters of the W330F variant compared to the wild-type enzyme. The rapid-scan absorption spectra of W330F mixed with a 50-fold excess of peroxyacetic acid resulted in an analogous pattern and reaction order as the wild-type enzyme, with the same 3 species, 2 rate model described for the wild-type enzyme producing a good fit to the experimental data (Fig. 4.7, panel A). However, consistent with the manually mixed spectra shown in Fig. 4.2, the final compound I spectrum of W330F is

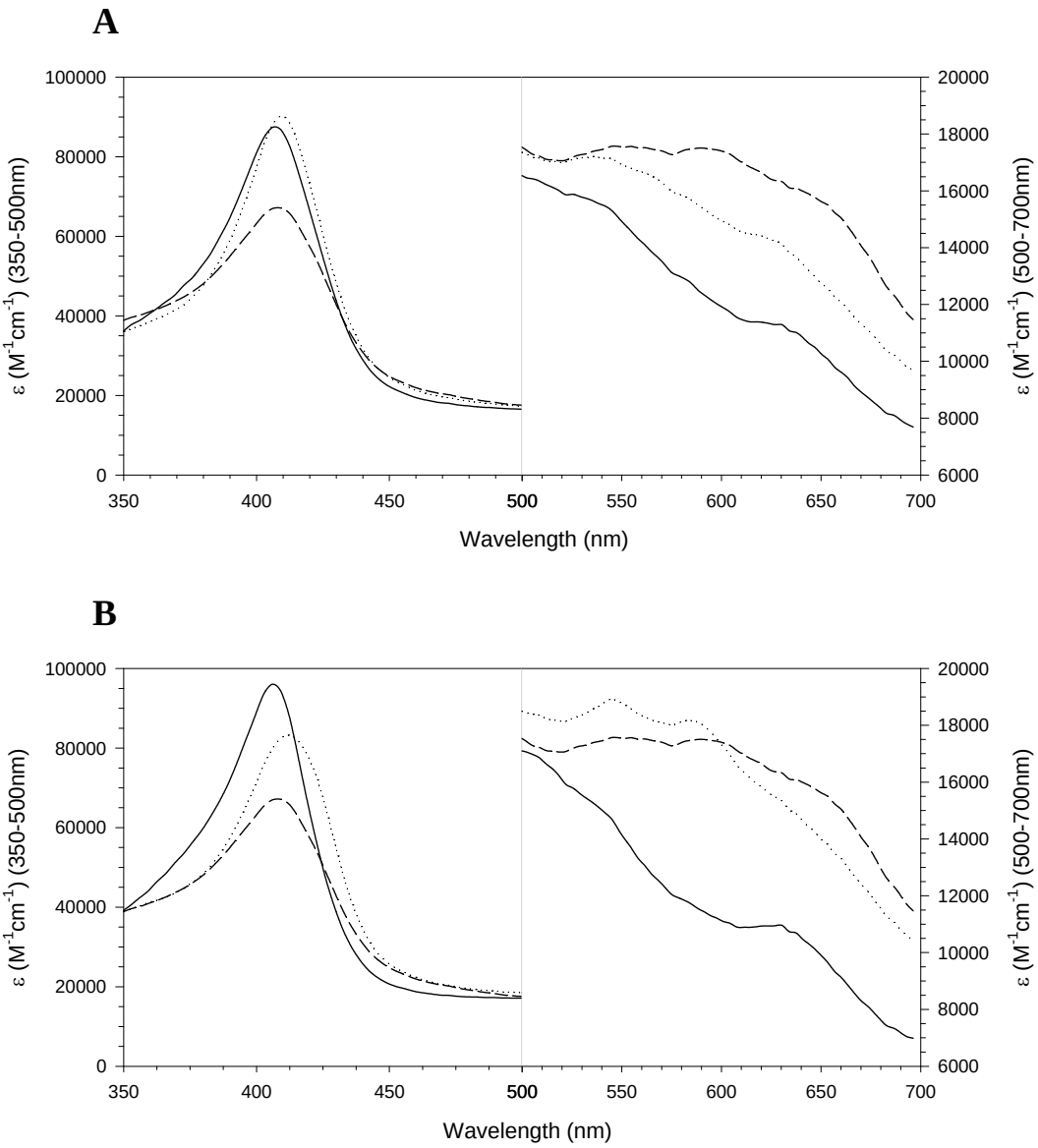

Figure 4.7. The fitted spectra of W330F after mixing with a 50-fold excess of peroxyacetic acid at pH 7.0. Panel A: the model consists of ferric enzyme (solid line) followed by a rapidly formed ferric-like Species X (dashed line), followed by the formation of compound I (dashed line). Panel B: overlay of the final intermediates (compound I) of wild-type BpKatG (dotted line) and W330F (dashed line) when mixed with a 50-fold excess of peroxyacetic acid at pH 7.0. The solid line represents the ferric resting state enzyme.

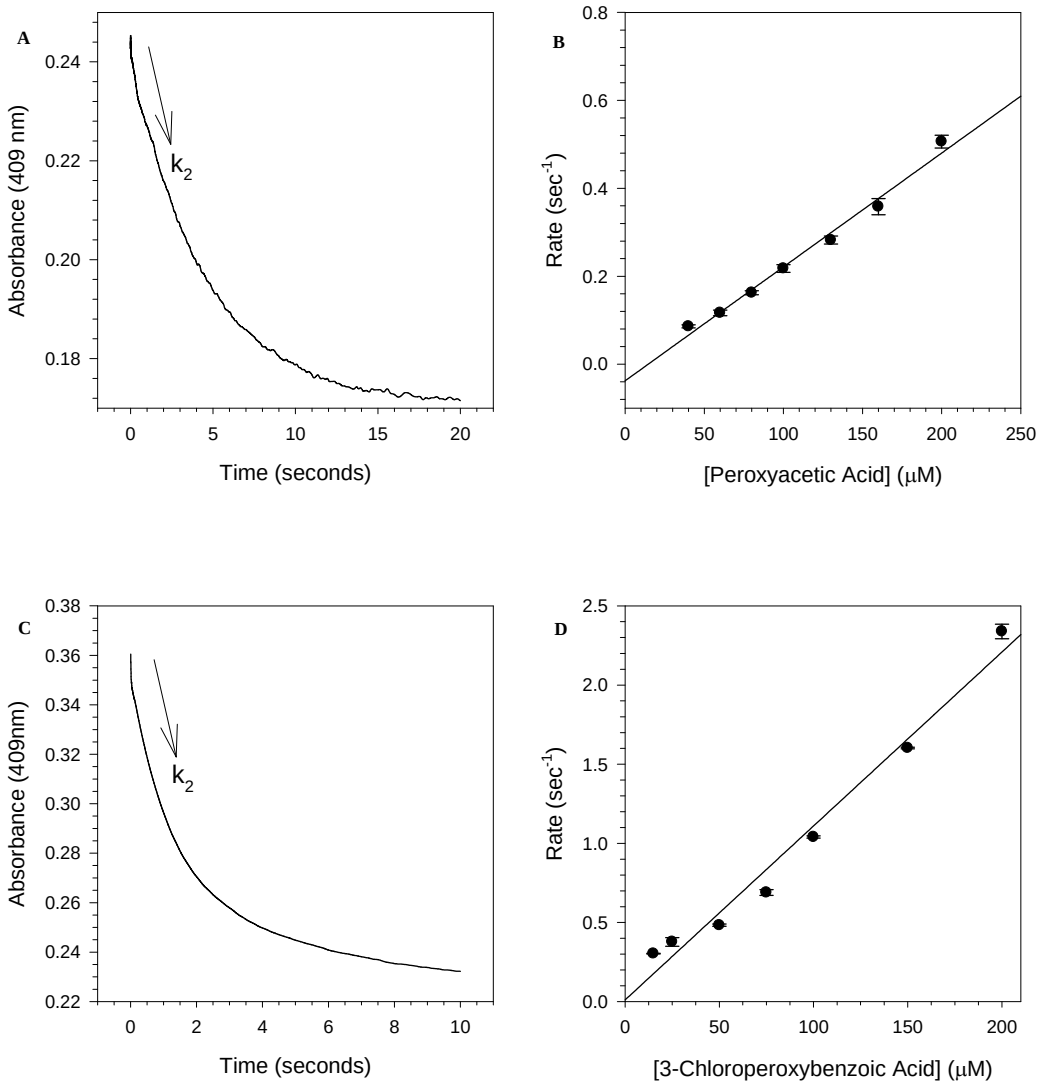

Figure 4.8. Change in absorbance at 409 nm for the reaction of W330F with peroxyacetic acid (Panel A) and 3-chloroperoxybenzoic acid (Panel C) with time. Peroxyacetic acid (Panel B) and 3-chloroperoxybenzoic acid (Panel D) dependence of the transition rate k_2.

Table 4.5. Bimolecular rate constants of k_1 and k_2 for BpKatG and W330F when mixed with either peroxyacetic acid or 3-chloroperoxybenzoic acid.

Substrate	**k_1 ($sec^{-1}M^{-1}$) x 10^4**		**k_2 ($sec^{-1}M^{-1}$) x 10^3**	
	wild-type	**W330F**	**wild-type**	**W330F**
Peroxyacetic acid	6.47 ± 0.45	n.d.[a]	2.50 ± 0.20	2.60 ± 0.10
3-chloroperoxybenzoic acid	44.3 ± 0.16	n.d.	31.0 ± 0.07	11.0 ± 0.07

[a]too rapid to be determined (see text).

characteristic of a $Por^{\bullet+}$ Fe^{IV}=O species with a marked decrease in the absorbance (roughly 40 %) and virtually no shift in the Soret and the concomitant appearance of a strong broad band around 655 nm. Fig. 4.7, panel B shows the striking difference between the compound I of the wild-type enzyme (dotted line) and W330F (dashed line) with the compound I spectrum of the wild-type enzyme containing a slight shoulder at 655 nm compared to the strong broad band of W330F suggesting a much lower proportion of the $Por^{\bullet+}$ Fe^{IV}=O species in the wild-type enzyme compared to W330F.

Similar to the wild-type enzyme, the change in absorbance at 409 nm as a function of peroxyacetic and 3-chloroperoxybenzoic acid was monitored in order to determine the k_1 and k_2 rate constants for the transition of resting enzyme → species X and species X → compound I respectively. Unfortunately, even though species X is present in W330F, the initial transition from resting state to species X (k_1) could not accurately be fit to a double exponential equation (Fig. 4.8). However, the rate of the second transition from species X to compound I (k_2) could be determined by fitting the change in absorbance at 409 nm to a single exponential equation and was similar to the wild-type enzyme with both peroxyacetic and 3-chloroperoxybenzoic acid (k_2 = 2.60 x 10^3 $M^{-1}sec^{-1}$ and 1.10 x 10^4 $M^{-1}sec^{-1}$ respectively) and is summarized in Table 4.5.

Asp141 is positioned at the entrance to the access channel leading to the heme cavity and, with Arg108, is part of an important hydrogen bonding network. It has been previously shown that replacement of both of these residues significantly reduce catalase activity, but have a lesser effect on peroxidase

activity (Deemagarn *et al*, 2007). To test whether these residues affect the formation of species X, rapid-scan absorption spectra were recorded for D141A, R108A, and R108A/D141A mixed with a 50-fold excess of peroxyacetic acid at pH 7.0 (Fig. 4.9). In contrast to the wild-type enzyme and W330F, no spectral changes consistent with species X could be detected in all 3 cases. All 3 variants showed only a decrease in absorbance of the Soret, and changes similar to the wild-type enzyme in the 500-700 nm region consistent with the formation of an oxoferryl, compound I-like intermediate. One interesting difference was the persistence of the charge transfer band around 640 nm throughout the reaction with peroxyacetic acid in all 3 variants suggesting a large contribution of resting enzyme and generally unreactive enzyme. Interestingly, in the case of D141A, the bands at 545 and 585 nm appeared within 80 msec upon mixing with peroxyacetic acid indicating that the reaction proceeded much faster than in the wild-type enzyme. Additionally, in all 3 cases the bands at 545 and 585 nm are much less well defined when compared to the wild-type enzyme suggesting a significant disruption to the hydrogen-bonding network.

Analysis of the time dependent spectral data of D141A mixed with a 50-fold excess of peroxyacetic acid using a 1-step model resulted in an estimated rate of 15 sec^{-1} compared to 1 sec^{-1} in the case of the wild-type enzyme. In the case of the R108A and R108A/D141A variants, the reaction is slower than D141A, as the features of the ferryl species are only detected after 1.7 seconds resulting in transition rates of 0.4 sec^{-1} and 0.9 sec^{-1} respectively. Since no species X can be detected, the transition rates are for the resting state → compound I (or compound

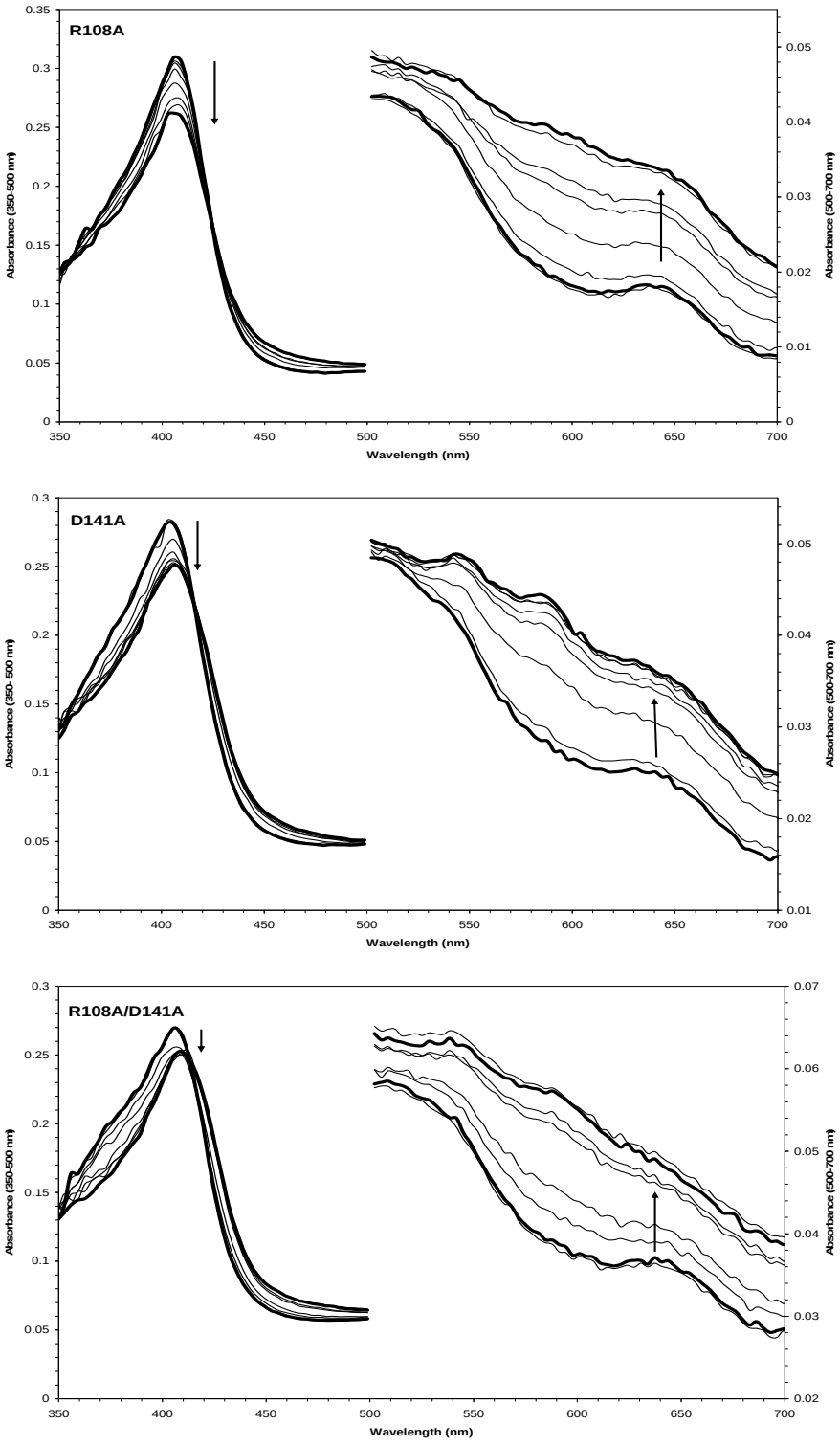

Figure 4.9. Rapid-scan absorption spectra of the reaction of D141A, R108A, and D141A/R108A variants with a 50-fold excess of peroxyacetic acid at pH 7.0. The bold spectra represent the first (1.3 msec) and last (10 sec) after mixing with peroxyacetic acid. The intermediate spectra are at 3.8 msec, 78 msec, 400 msec, 1.7 sec, 3.0 sec, 5.0 sec, and 10 sec.

I like) in R108A, D141A, and R108/D141A compared to species X → compound I in the wild-type enzyme. In conclusion, a stable species X is not detected in the rapid-scan absorption spectra of the single or double variants of Arg108 or Asp141 when mixed with a 50-fold excess of peroxyacetic acid, possibly the result of the absence of residues involved in ligand binding.

4.2.5. Influence of pH on the absorption spectrum of compound I in BpKatG

The spectra of wild-type BpKatG when mixed with a 50-fold excess of peroxyacetic acid at pH 4.5, 7.0, and 8.5 are shown in Fig 4.10. The ferric, resting state spectra are virtually identical at all pHs, with a Soret band absorption maximum at 407 nm and the charge transfer band at 635 nm. At pH 7.0, the resulting spectrum of compound I generated when mixed with peroxyacetic acid exhibited a 25 % decrease in intensity and shift of the Soret band to 415 nm with the concomitant appearance of bands at 545 and 585 nm and an ill-defined shoulder around 655 nm. At pH 4.5, the resulting spectrum when mixed with peroxyacetic acid was similar to that observed at pH 7.0, except the decrease in intensity of the Soret band was only 15 % and the ill-defined shoulder around 655 nm was even less evident with the bands at 545 and 585 nm appearing slightly more defined. Interestingly at pH 8.5, the resulting spectra generated after mixing revealed a 35 % decrease in intensity and shift to only 410 nm of the Soret band with the concomitant appearance of a strong broad band around 655 nm. This spectrum is very similar in appearance to what was observed when W330F was mixed with a 50-fold excess of peroxyacetic acid and is characteristic of a $Por^{\bullet+}$ Fe^{IV}=O oxoferryl intermediate.

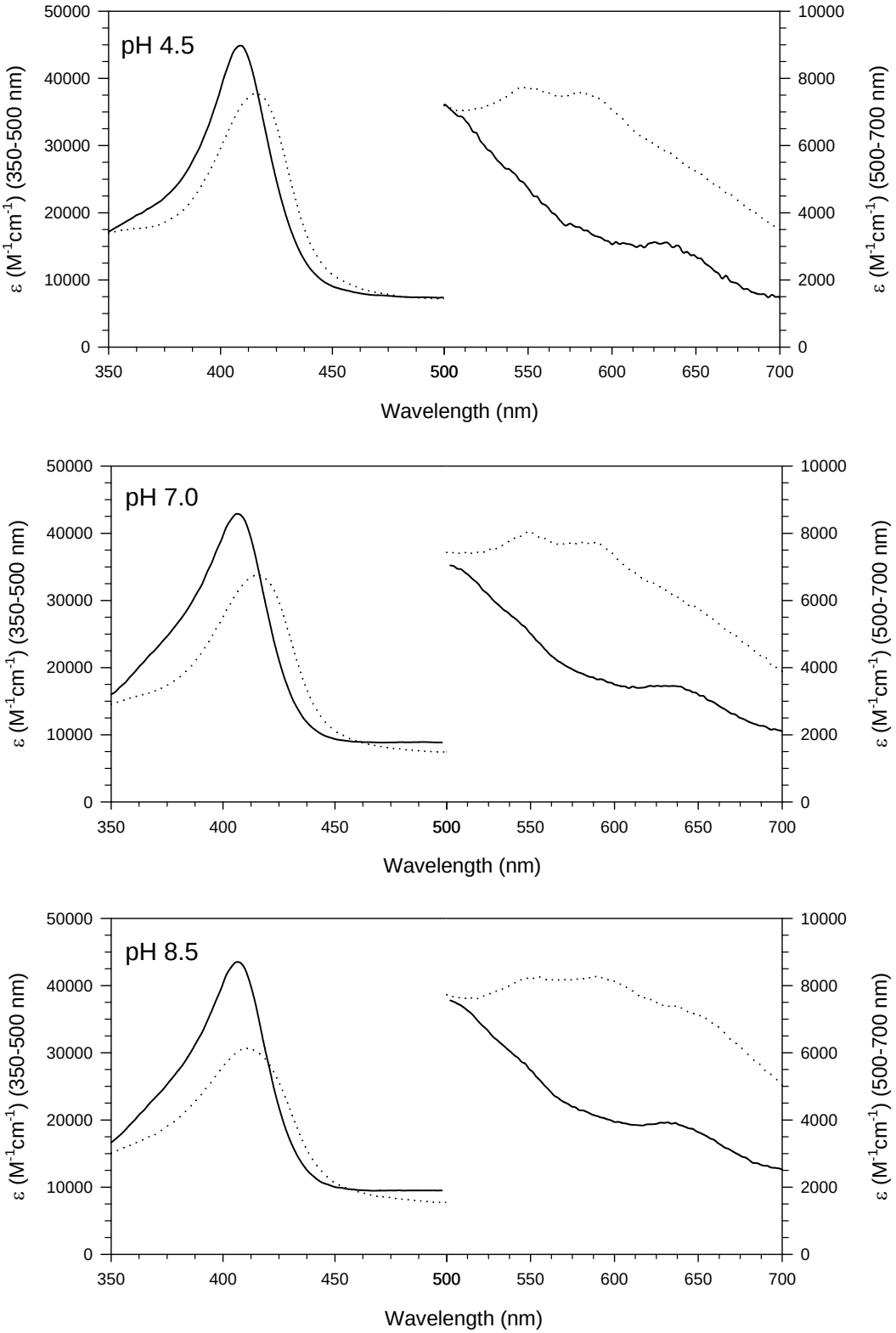

Figure 4.10. Fitted absorption spectra of wild-type BpKatG mixed with a 50-fold excess of peroxyacetic acid at various pHs.

To summarize, the spectra of compound I generated in wild-type BpKatG at pH 4.5, 7.0, and 8.5 show a clear pattern consistent with an increase in the amount of $Por^{\bullet+}$ Fe^{IV}=O as pH increases (Fig 4.12 panel A). Upon reaction with peroxyacetic acid the decrease in intensity of the Soret band increases as pH increases, going from 15 % at pH 4.5 to 35 % at pH 8.5 and this is accompanied by the appearance of a strong, broad band around 655 nm that is quite evident at pH 8.5. The fact that the spectrum generated with peroxyacetic acid at pH 8.5 in the wild-type enzyme is very similar in appearance to the spectrum of the oxoferryl intermediate of W330F is consistent with the formation of a $Por^{\bullet+}$ Fe^{IV}=O intermediate, although the 35 % decease in intensity and slight shift to 410 nm of the Soret band compared to the changes in the W330F spectrum suggest that the proportion of $Por^{\bullet+}$ Fe^{IV}=O is lower in the native enzyme.

4.3. Discussion

There have been several reports analyzing the reaction of KatGs with peroxyacetic acid on a millisecond time scale using stopped-flow rapid scan techniques and at least two of them have reported an intermediate preceding the formation of the typical compound I spectral features seen in peroxidases (Ghiladi *et al*, 2005a, and Jakopitsch *et al*, 2007). Ghiladi *et al* (2005a) present a clear 2-step reaction pathway for the oxidation of the KatG from *Mycobacterium tuberculosis*. The initial species, exhibiting an increase in the Soret band and 10 nm blue shift in the charge transfer region was identified as a compound II intermediate, despite the differences from the typical compound II peroxidase spectrum. This alternate spectrum of compound II was rationalized by the

stacking effects of the Trp portion of the KatG specific Trp-Tyr-Met adduct 3.4 Å above the heme. This interpretation suggested that MtKatG undergoes a rapid 1 electron oxidation to form a Por Fe^{IV}=O $AA^{\bullet}$ species that rapidly equilibrates to form a Por Fe^{III}-OH $AA^{\bullet}$ species. Although such a species could explain the modified ferric spectrum there is no evidence of an oxoferryl-type species in the early spectra and the direct oxidation of the protein prior to heme oxidation is so far unprecedented in heme peroxidases. Jakopistch *et al* (2007) also observed the initial increase in the intensity of the Soret band and up shift in the charge transfer region but no explanation was given.

Characterization of the reaction of BpKatG with peroxyacetic acid by stopped-flow spectrophotometry resulted in the same initial increase in the intensity of the Soret band and small blue shift in the charge transfer region (species X) prior to the formation of the spectrum characteristic of a typical compound I, oxoferryl intermediate (Fig. 4.5). Instead of an initial oxidation of the protein prior to heme oxidation as proposed by Ghiladi *et al*, a more straightforward explanation is the rapid formation of an initial enzyme-substrate complex (Por Fe^{III}-PAA) followed by the actual oxidation of the heme to form the oxoferryl intermediate, compound I. This is in fact not an unexpected outcome for several reasons. First of all, an enzyme-substrate complex is an expected intermediate in all enzymatic reactions and does not require the proposal of new or unusual intermediates. A very similar Por Fe^{III}-H_2O_2 complex has been reported in the R38L variant of horseradish peroxidase (Rodriguez-Lopez *et al*, 1996) providing a precedent for such a species. Second, the ferric-like spectrum

of species X is consistent with a higher proportion of a sixth coordination of the ferric iron in peroxidases that would be expected during the formation of a Por Fe^{III}-PAA complex (Schonbaun, 1973) and the subsequent oxidation reaction does in fact lead to an expected spectrum of a higher valence Fe^{IV} species. Third, very similar changes in the absorption spectrum of horseradish peroxidase have been reported as a result of benzohydroxamic acid binding on the distal heme side and attributed to a greater proportion of 6-coordination (Henriksen *et al*, 1998). Also the absorption spectrum of acetate bound to cytochrome *c* peroxidase shows a similar, albeit much more pronounced increase in the intensity of the Soret and increase in intensity in the charge transfer band (Mathews and Wittenberg, 1979). Finally, the reaction of cytochrome P450cam with peroxyacetic acid monitored by stopped-flow spectrophotometry also showed evidence for an enzyme-PAA complex en route to the formation of compound I (Spotilak *et al*, 2005).

Surprisingly, kinetic characterization of this 2-step pathway showed that both reaction rates k_1 and k_2, for ferric → species X, and species X → compound I respectively, were dependent upon peroxyacetic acid concentration (Fig. 4.6). That is to say, the binding of 2 molecules of peroxyacetic acid (or 3-chloroperoxybenzoic acid) are required for the actual oxidation of the heme to form the ferryl intermediate, compound I. If this was simply peroxyacetic acid binding, followed by intramolecular electron transfer to the heme, then the rate of ferric enzyme ferric → species X (k_1) would increase with peroxyacetic acid concentration and the rate of species X → compound I (k_2) would not be affected by changes in its concentration. However, both rates increase with peroxyacetic

acid concentration suggesting that a second molecule of peroxyacetic acid is required for the species X → compound I transition. The conclusion that an enzyme-substrate complex precedes the formation of the compound I, ferryl species is consistent with well-accepted enzyme theory and is consistent with a model proposed for the binding of hydrogen peroxide to monofunctional peroxidases (Loew and Dupuis, 1996). However, the conclusion that there are 2 separate peroxyacetic acid binding events leading to heme oxidation is new.

The role played by PAA binding in the formation of the enzyme-substrate complex (Por Fe^{III}-PAA) is clear, but the role of the second PAA molecule is not as obvious. The simplest explanation is that the initial Por Fe^{III}-PAA complex has the PAA (PAA1) bound in an orientation that is not conducive to heme oxidation and the binding of the second PAA (PAA2) facilitates the reorientation of PAA1 to allow oxidation. In other words, there are 2 orientations of PAA1 in proximity to the heme that are in equilibrium, $PAA1^{U} \leftrightarrow PAA1^{R}$ (where U and R represent unreactive and reactive conformations respectively), with the equilibrium favoring $PAA1^{U}$ in the absence of PAA2 and favoring $PAA1^{R}$ in the presence of PAA2.

As shown in Fig. 4.11 the heme cavity provides sufficient room to accommodate 2 molecules of PAA. The distal heme active site and the extended hydrogen bonding network is shown in Fig. 4.11, panel A and fitting PAA1 displaces 2 water molecules and shifts W1 to W1' (Fig. 4.11, panel B). As shown in Fig 4.11, panel B, $PAA1^{U}$ alone, binds with its carboxyl oxygen, replacing one of the waters and forming hydrogen bonds with the guanidinium of Arg108 and

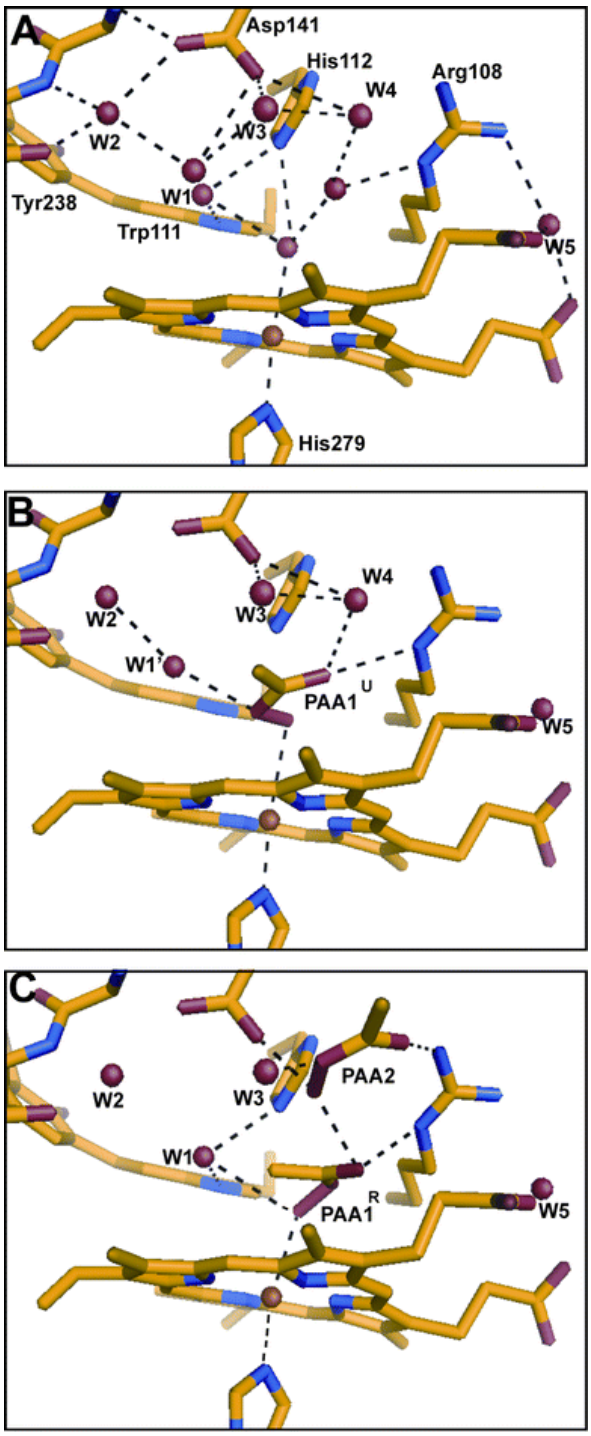

Figure 4.11. Possible binding sites for peroxyacetic acid. Taken from Wiseman *et al*, 2009 with permission. Panel A: heme active site and water matrix without PAA bound. Panel B: potential binding site for the first incoming PAA1. Panel C: potential binding sites of both molecules of PAA together. See text for details. This figure was prepared with coordinates submitted to the protein data bank (PDB id: 1MWV) and bound PAA were inserted manually using the program Coot (Emsley and Cowtan, 2004).

water W4. Also, the hydroxyl oxygen of $PAA1^{U}$ is situated 2.78 Å from the imidazole nitrogen of His112 and 2.86 Å from the heme iron, albeit in a poor geometry for hydrogen bonding. The direct involvement of Arg108 and Asp141 (through W4) in binding is consistent with the apparent absence of the Por Fe^{III}-PAA complex (species X) in the rapid-scan absorption spectra of the D141A, R108A, and R108A/D141A variants. The reorientation of $PAA1^{U}$ to $PAA1^{R}$ then occurs with the binding of PAA (PAA2). As shown in Fig 4.11, panel C the orientation of $PAA1^{R}$ is less stable with only a single hydrogen between the noncarboxyl oxygen and Arg108 having poor geometry. Thus the role of PAA2 is to stabilize $PAA1^{R}$ by forming a hydrogen bond with the carboxyl oxygen of PAA1. This is further stabilized by a hydrogen bond between the carbonyl oxygen of PAA2 and the guanidinium group of Arg108, and hydrogen bonds of the -OOH portion with W3 and Asp141.

Not only is the orientation of PAA1 unreactive but the 0.5 Å shift of W1 to W1' places it in a location where it cannot interact with either His112 or the –OOH of $PAA1^{U}$. However, the reorientation $PAA1^{R}$ allows W1 back into the hydrogen bonding matrix, hydrogen bonding with the –OOH of PAA1 and the imidazole N of His112. In this position, it can participate in a proton transfer process that lowers the energy barrier for proton transfer from the OOH to the imidazole ring (Derat *et al*, 2007).

The resulting spectrum after addition of peroxyacetic acid to resting BpKatG (Fig. 4.2 (dotted trace)) showed a 20 % decrease in absorbance, slight broadening and shift to 415 nm of the Soret and the concomitant appearance of 2

bands at 545 and 585 nm consistent with a compound I-like intermediate. The compound I of ascorbate peroxidase consists of a $Por^{\bullet+}$ Fe^{IV}=O $Por^{\bullet+}$, and its absorption spectrum exhibits a 50 % decrease, but no shift, in the Soret band and an increase in the charge transfer region compared to the ferric enzyme (Patterson *et al*, 1995). On the other hand, the compound I of cytochrome *c* peroxidase consists of a Por Fe^{IV}=O in combination with a protein radical located on the proximal tryptophan (Trp191) instead of the porphyrin ring. Its spectrum exhibits a 10 % increase in absorbance and shift to 420 nm in the Soret band with 2 strong bands at 530 nm and 560 nm (Sivaraja *et al*, 1989). The spectrum of compound I in BpKatG at pH 7.0 appears to be an average between the spectra of compound Is in ascorbate peroxidase and cytochrome *c* peroxidase suggesting a mixture between $Por^{\bullet+}$ Fe^{IV}=O and Por Fe^{IV}=O $Trp^{\bullet+}$ and is consistent with the detection of multiple radical signals in a number of EPR studies on KatGs (Ivancich *et al*, 2003, Jakpitsch *et al*, 2006, Singh *et al*, 2007, and Colin *et al*, 2009).

Mutation of the proximal Trp330 to a phenylalanine resulted in only slightly reduced catalase and peroxidase activities and the variant exhibited similar kinetics upon reaction with peroxyacetic acid as the wild-type enzyme. However, the final compound I exhibited the characteristic spectral features of the $Por^{\bullet+}$ Fe^{IV}=O species. The resulting spectrum is comparable to the compound Is of horseradish peroxidase (Veitch, 2004) and ascorbate peroxidase (Patterson *et al*, 1995), both of which contain an $Por^{\bullet+}$ Fe^{IV}=O species. The compound I of cytochrome *c* peroxidase consists of a tryptophanyl radical located on Trp191, but a spectrum similar to that of W330F is observed in theW191F variant (Erman *et*

al, 1989), where the rapid-scan spectra of the reaction with hydrogen peroxide produced the analogous decrease in intensity of the Soret seen in the W330F variant of BpKatG. Consistent with this is a recent EPR study on BpKatG that revealed the exchange coupled tryptophanyl radical is in fact located on the conserved proximal Trp330 (Colin *et al*, 2009), analogous to cytochrome *c* peroxidase. In other words, BpKatG resembles cytochrome *c* peroxidase, in having the short lived porphyrin π-cation radical quenched by an electron from the adjacent proximal tryptophan, resulting in a radical that is in close contact with the oxoferryl heme iron, an exchange-coupled radical (Colin *et al*, 2009). In the W330F variant this process is blocked (or slowed) resulting in a much higher proportion of the $Por^{\bullet+}$ Fe^{IV}=O species and the corresponding characteristic absorption spectrum of a 50 % decrease in intensity of the Soret band.

Summarized in Fig. 4.12, panel A, the spectra of compound I species generated in the wild-type enzyme at pH 4.5, 7.0, and 8.5 show a clear pattern, suggesting an increase in the amount of $Por^{\bullet+}$ Fe^{IV}=O as pH increases. This is consistent with protein radicals predominating at low pH and the porphyrin radical predominating at high pH (Carpena *et al*, 2006). High resolution crystal structures of compound I of BpKatG generated by soaking crystals in a solution of peroxyacetic acid (soaked at roughly pH 6.0) prior to X-ray data collection revealed an iron-oxygen species with a bond length of 1.88 Å (Carpena *et al*, 2005), a value between the Por Fe=O bond lengths reported for horseradish peroxidase (Berglund *et al*, 2002), but very similar to the 1.87 Å observed in the structure of compound I of cytochrome *c* peroxidase (Bonagura *et al*, 2003). It

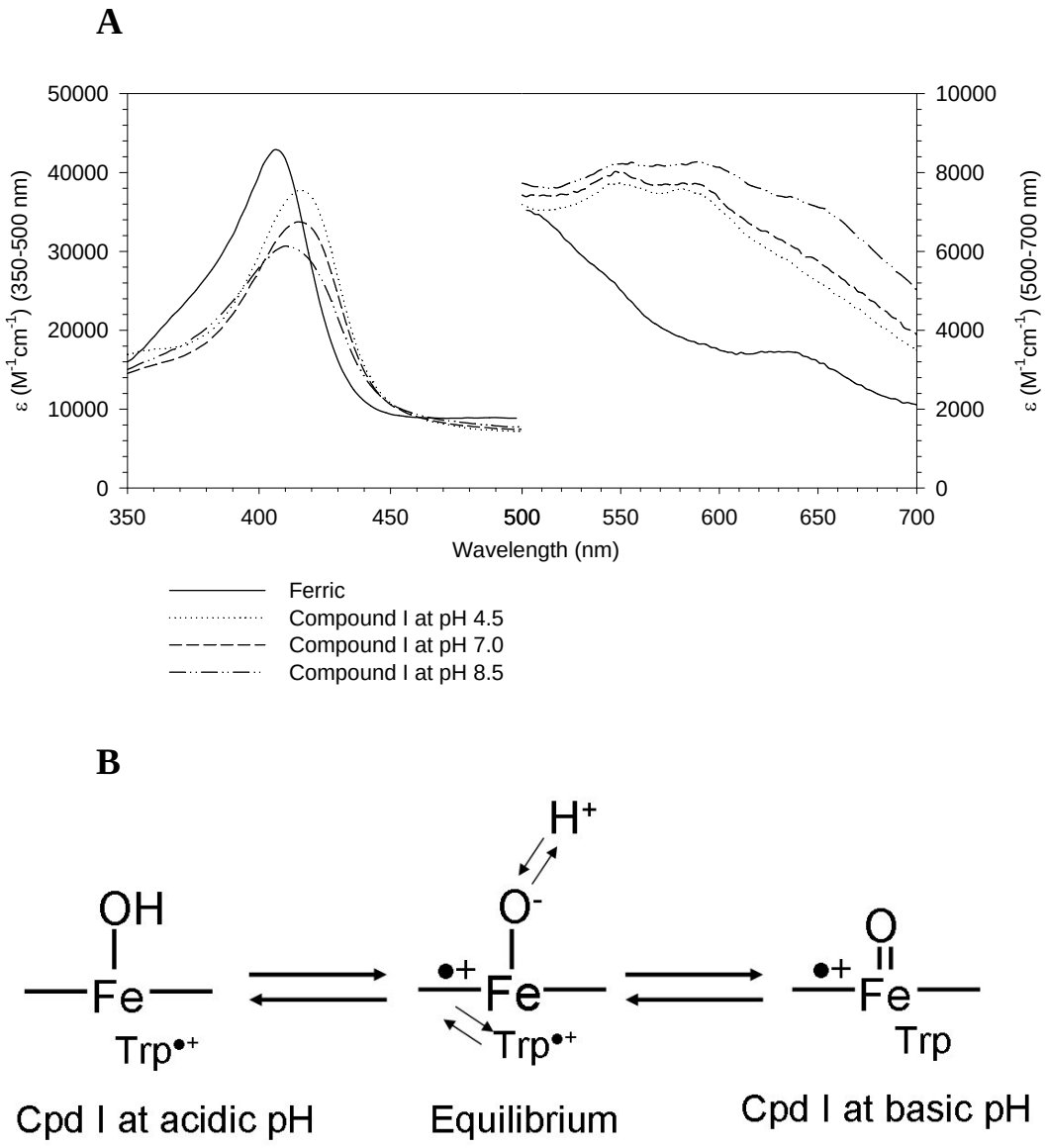

Figure 4.12. Structure of compound I at various pHs. Panel A: overlay of the fitted spectra shown in Fig. 4.10, for clarity only the ferric spectra at pH 7.0 is shown. Panel B: scheme depicting the possible structures of compound I at various pHs.

was suggested that this slightly longer iron-oxygen bond length could be interpreted as the result of reduction of the oxoferryl species by X-ray exposure (Berglund *et al*, 2002) or of compound I having a single Fe-OH bond. The high resolution crystal structures of the compound I in cytochrome *c* peroxidase (Bonagura *et al*, 2003) also suggest that compound I consists of a Fe-O single bond with 1 oxidation equivalent delocalized to Trp191. Both the crystal structure of compound I and the absorption spectra of Compound I species generated at different pHs suggest that the BpKatG Compound I is a mixture in equilibrium between $Por^{\bullet+}$ Fe^{IV}=O and Por Fe^{IV}=O $Trp^{\bullet+}$. As described in Fig. 4.12 panel B, at acidic pH the Fe-O will be protonated with one oxidizing equivalent delocalized to Trp330 and as pH becomes increasingly basic, the Fe-O will become deprotonated and with the oxidizing equivalent remaining on the porphyrin ring.

Modulation between protein and porphyrin radicals as a function of pH can help further explain the characteristic pH profile of catalase-peroxidases which exhibit maximum peroxidase activity at approximately pH 4.5 and maximum catalase activity at pH 6.5. Although the natural peroxidase substrate in KatGs is unknown, the likelihood of a bulky substrate interacting with the heme is low, because the heme active site is much more constricted then in monofunctional peroxidases. Thus at pH 4.5 where the peroxidase reaction is at its maximum, the Fe-O will be protonated and there will be a shift to a higher amount of protein radicals that can facilitate reaction with any large peroxidase substrate that would very likely be bound on the surface of the protein distant

from the heme active site. Conversely, as pH increases (and peroxidase activity decreases) there will be a shift to more porphyrin radical that will not be as easily quenched by bulky groups but which will facilitate the catalase reaction.

4.4. Conclusion

Probably due to the much more restricted active site and a more defined water matrix in catalase-peroxidases compared to monofunctional peroxidases, an enzyme-substrate complex formation step is slow enough to be monitored by stopped-flow absorption spectrophotometry. Upon addition of PAA to BpKatG there is an initial rapid formation of an enzyme-substrate complex within 30 msec, followed by the subsequent formation of an oxoferryl, compound I intermediate within 400 msec. Surprisingly, both steps were determined to be PAA dependent implying that 2 molecules of PAA are required to form a typical compound I intermediate. An analogous 2-step reaction is also observed with 3-chloroperoxybenzoic acid suggesting that this could be a general reaction mechanism for the oxidation of catalase-peroxidases with any peroxy-acid. Mutation of the proximal tryptophan (Trp330) to a phenylalanine resulted in an analogous reaction pathway, except that the final compound I intermediate produced a spectrum characteristic of a $Por^{\bullet+}$ Fe^{IV}=O species consistent with this residue being the location of the tryptophanyl exchanged coupled radical in BpKatG (Colin *et al*, 2009).

The electronic structure of compound I appears to be an equilibrium between protein and porphyrin radicals with a pH dependence. Absorption spectra of the reaction between BpKatG and PAA revealed a clear trend to a

larger proportion of the $Por^{\bullet+}$ Fe^{IV}=O species as the pH increased and a greater proportion of Por Fe^{IV}-OH $Trp^{\bullet+}$ as the pH decreased. Consequently, in the physiological pH range there will be an equilibrium between porphyrin and protein radicals. The variation in compound I electronic structure with pH is also consistent with the observed pH optima for the catalase and peroxidase reactions.

5. CRYSTAL STRUCTURES OF BPKATG WITH INH AND NAD^+

5.1. Introduction

In 1992, catalase-peroxidases gained world wide attention when it was confirmed that the KatG from *Mycobacterium tuberculosis* was responsible for the activation of the anti-tuberculosis drug isoniazid and that mutations to the *katG* gene lead to INH resistance (Zhang *et al*, 1992). Although not fully understood, this 'activation' of INH involves the removal of the hydrazine group, which forms an isonicotinoyl radical that couples with NAD^+ to form the final IN-NAD adduct. The resulting IN-NAD adduct acts as a potent inhibitor of InhA by competitively binding to the active site and preventing NADH binding. The inhibition of InhA results in the accumulation of intermediate length long chain fatty acids and an inhibition of mycolic acid biosynthesis which in turn inhibits cell growth (Vilchèze and Jacobs, 2007).

Despite the availability of 4 KatG crystal structures and the accumulation of a large amount of scientific literature focusing on the cleavage of INH catalyzed by KatGs, no clear mechanism of how KatGs are able to accomplish this has emerged. It has been suggested that INH is somehow activated by KatGs through enzyme intermediates in the peroxidase reaction cycle (Magliozzo and Marcinkeviciene, 1997, and Ghiladi *et al*, 2005c) to generate an isonicotinoyl radical. How the subsequent coupling of the resulting isonicotinoyl radical to NAD^+ occurs is not well understood, but a nonenzymatic event involving a homolytic aromatic substitution reaction (Lei *et al*, 2000) is one possibility. However, it has been shown that KatGs can significantly increase the production

of both the isonicotinyl radical and the IN-NAD adduct (Singh *et al*, 2004) and that they are also capable of binding NAD^+/NADH and actually possess a low level of NADH oxidase activity, producing superoxide as a product (Singh *et al*, 2004). Superoxide can also be produced from molecular oxygen in the presence of INH as an electron donor in KatGs (Shoeb *et al*, 1985b, and Wengenack *et al*, 1999) and horseradish peroxidase (Shoeb *et al*, 1985a and 1985c). How this relates to INH activation or IN-NAD adduct formation remains unclear, but a 60 % slower superoxide diffusion rate from the highly resistant S324T variant of BpKatG compared to the wild-type enzyme has been reported (Demmagarn *et al*, 2005).

Hampering the understanding of this unusual reaction is the fact that the binding sites for both INH and NAD^+ in KatGs remain unknown. A structure of the INH analog benzohydroxamic acid bound to horseradish peroxidase (Henriksen *et al*, 1998) and structures of INH bound to both ascorbate peroxidase and cytochrome *c* peroxidase (Metcalfe *et al*, 2008) show binding near the heme edge in all cases. However, KatGs have a much longer and constricted access channel compared to other peroxidases, and the equivalent region of INH binding in cytochrome *c* peroxidase and ascorbate peroxidase and benzohydroxamic binding in horseradish peroxidase is constricted in KatGs making substrate access not impossible but much more difficult.

The leading cause of INH resistance is mutation to the *katG* gene, with the point mutation S315T (S324T in BpKatG) being found in 60 to 80 % of all clinically isolated strains of *M. tuberculosis*. This residue is located in the main

access channel, at its narrowest point, about 14 Å from the heme iron with the mutant being highly deficient in producing the IN-NAD adduct, yet retaining near wild-type enzyme levels of catalase and peroxidase activities. Structural determination of the S324T variant of BpKatG (Deemagarn *et al*, 2005) and the analogous S315T of MtKatG (Zhao *et al*, 2006) has shown the extra methyl group of the threonine to be pointing directly into the access channel, effectively narrowing it such that even water occupancy is reduced. Although the INH binding site is unknown, the most obvious explanation is that by narrowing the access channel, this mutation prevents INH binding (Deemagarn *et al*, 2005, and Zhao *et al*, 2006).

5.2. Results

5.2.1. Crystal structure of BpKatG with AMP/ADP/NAD^+ bound

BpKatG was crystallized in the presence of AMP, ADP, or NAD^+ as described in section 2.9. Brownish parallelepiped shaped crystals reaching about 0.5 x 0.2 x 0.2 mm in size were obtained within a few days and were indistinguishable from the previously described native crystals (Carpena *et al*, 2002). Like native crystals, crystals of BpKatG complexed with AMP, ADP, or NAD^+ belonged to the orthorhombic space group $P2_12_12_1$ and contained a dimer in the asymmetric unit. The diffraction data sets were refined to 1.90, 2.00, and 1.69 Å respectively (Table 5.1).

A comparison of the calculated electron density maps to those of the native enzyme revealed a region of density in the BpKatG-NAD^+ maps that was not present in the native BpKatG maps. The strongest portion of this density

Table 5.1. Data collection and structural refinement statistics for BpKatG with NAD^+, AMP, and ADP bound.

Data collection statistics	**BpKatG-NAD^+**	**BpKatG-AMP**	**BpKatG-ADP**
Space group	$P2_12_12_1$	$P2_12_12_1$	$P2_12_12_1$
Unit cell parameters			
a (Å)	100.6	100.4	101.1
b (Å)	114.9	114.2	113.0
c (Å)	174.5	174.2	175.6
α, β, γ (°)	90, 90, 90	90, 90, 90	90, 90, 90
Resolution (Å)	38.0-1.69 (1.78-1.69)[a]	35.1-1.90 (2.00-1.90)	33.2-2.0 (2.11-2.00)
Unique reflections	225,404	145,296	136,027
Completeness (%)	99.9 (100.0)	91.6 (87.0)	100.0 (100.0)
R_{sym}[b]	0.084 (0.48)	0.11 (0.72)	0.27 (0.375)
$\langle I/\sigma I \rangle$ (%)	10.3 (2.9)	9.2 (1.9)	4.9 (2.9)
Multiplicity	5.1 (5.0)	3.6 (2.9)	6.3 (6.3)
Model refinement statistics			
No. of reflections	214,061	137,960	129,219
R_{cryst} (%)[c]	15.4	16.6	17.3
R_{free} (%)[d]	18.1	20.8	21.4
Non hydrogen atoms	12,734	12,623	12,628
Water molecules	1508	1475	1408
Average *B*-factor (Å^2)			
Protein	16.4	16.6	10.5
Heme group	12.2	12.8	6.6
Waters	26.4	24.7	18.6
Est. coordinate error (Å)[e]	0.049	0.093	0.092
Rms deviations			
In bonds (Å)	0.028	0.022	0.024
In angles (°)	2.11	1.73	1.78

[a]Values in parentheses correspond to the highest resolution shell.
[b]$R_{sym} = \Sigma_{hkl} \Sigma_j |I_{hkl,j} - \langle I_{hkl} \rangle| / \Sigma_{hkl} \langle I_{hkl} \rangle$.
[c]$R_{cryst} = \Sigma ||F_{obs}| - |F_{calc}|| / \Sigma |F_{obs}|$.
[d]R_{free} is as for R_{cryst} but calculated for a test set of reflections not used in the refinement.
[e]Based on maximum likelihood.

refined very well as ADP whereas the remainder was too weak and variable among data sets for reliable model refinement, presumably because the nicotinamide portion of the molecule is less tightly bound creating disorder in the crystal. The region of the F_o-F_c omit map calculated without ADP in the model satisfies the structure of ADP when superimposed (Fig. 5.1 A). Since STD NMR suggested that the adenosine portion of the dinucleotide could bind to the enzyme (Wiseman *et al*, in preparation), co-crystallization complexes of BpKatG and AMP or ADP were also prepared and analyzed. The corresponding region of the F_o-F_c omit map calculated without AMP fits the structure of AMP perfectly when superimposed into the map (Fig. 5.1 B). The locations of binding of the ADP portion of NAD^+ and of AMP coincide perfectly except for the absence of the second phosphate and a 60 ^{o} rotation of the oxygens on the α-phosphate. Similarly, although the electron density maps were of slightly lower resolution and there was only partial occupancy of ADP, the location of the ADP binding coincides perfectly with the ADP portion of NAD^+ as shown in Fig. 5.1 C.

Surprisingly, the NAD^+ binding site is not in the heme cavity, or even in the access channel leading to the heme cavity, but on the protein surface located approximately 20 Å from the edge of the opening of the channel (Fig. 5.2). The principal interactions controlling the protein-nucleotide binding are identical in the ADP portion of NAD^+ and AMP, including the carboxylate of Asp222 with the N6-amino group of the adenine ring (3.4 Å) and the carboxylate of Asp249 with C2'-OH of the adenosine ribose (2.9 Å). These 2 interactions are supplemented by the guanidinium group of Arg255 situated 3.3 Å from the

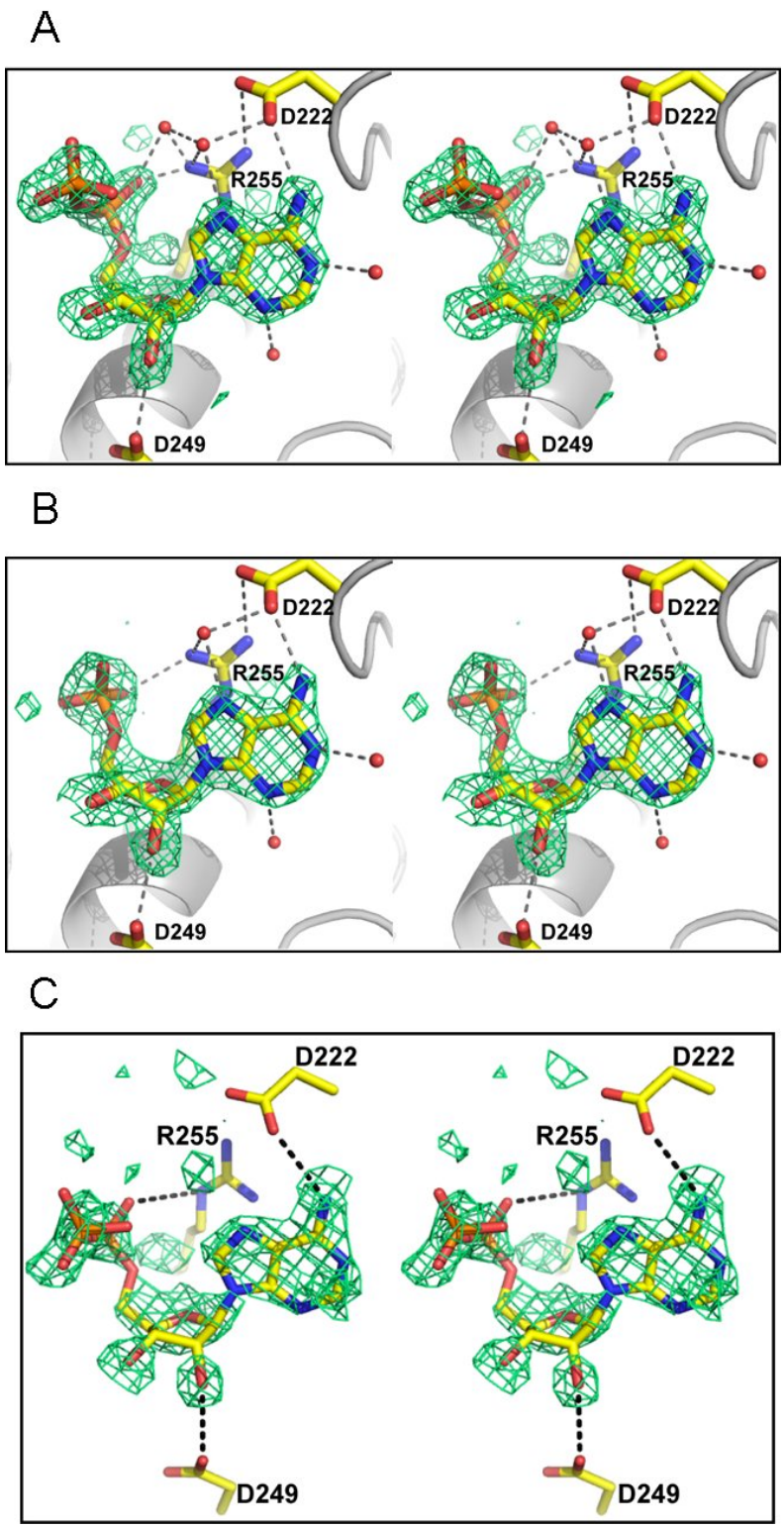

Figure 5.1. Stereo views of the NAD^+ (panel A), AMP (panel B), and ADP (panel C) binding site in BpKatG. The F_o-F_c omit electron density maps were calculated using a model lacking NAD^+, AMP, or ADP and drawn at $\sigma = 3.0$ in green.

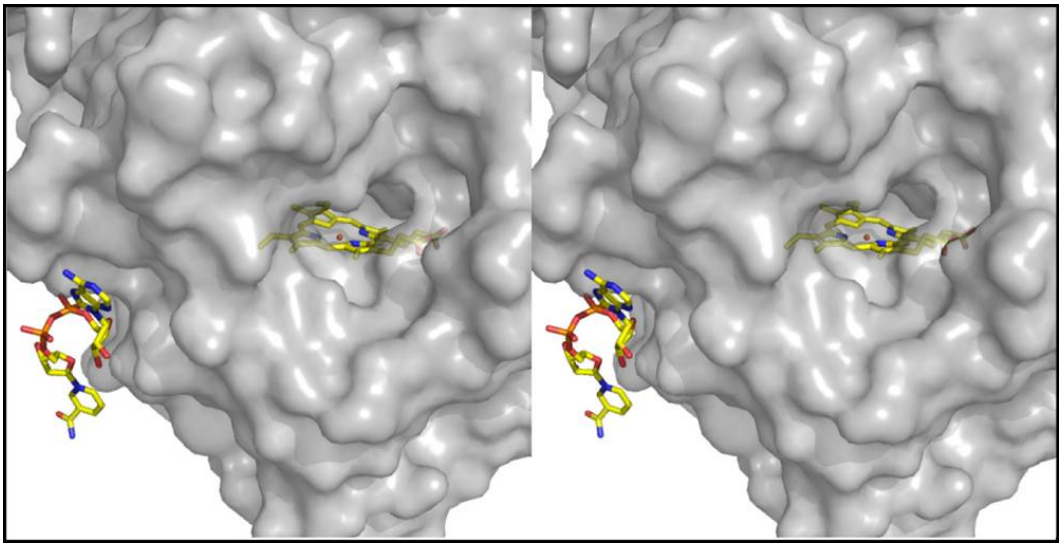

Figure 5.2. Stereo view of the surface of BpKatG and the NAD^+ binding site in relation to the heme active site and substrate access channel. The NAD^+ is modelled using the ADP density shown in Fig. 5.1 and the nicotinamide portion has been fit, but not refined, into a region of poorly defined electron density.

phosphate oxygen and also 3.4 Å from Asp222. In addition, each of N1, N3 and N7 of the adenine ring form strong hydrogen bonds with adjacent waters (2.7, 2.8 and 2.7 Å, respectively) with the water adjacent to N7 also interacting with Arg255 and Asp222. As shown in Fig. 5.1, the orientation of the phosphate in NAD^+ allows 1 additional water to be bound among the phosphate oxygen, the Arg255 guanidinium group and the water associated with N7 that is not present when AMP is bound.

5.2.2. Crystal structure of BpKatG with INH bound

The co-crystallization conditions that were developed that led to BpKatG-INH complexes are described in section 2.9. Brownish parallelepiped shaped crystals reaching about 0.5 x 0.2 x 0.2 mm in size were obtained within a few days and were indistinguishable from the previously described native crystals (Carpena *et al*, 2002). Like native crystals, crystals of the BpKatG-INH complex belonged to the orthorhombic space group $P2_12_12_1$ and contained a dimer in the asymmetric unit. The diffraction data set was refined to 2.09 Å (Table 5.2).

A comparison of the calculated electron density maps to those of the native enzyme revealed 3 regions of density in the BpKatG-INH maps that were not present in the native BpKatG maps. Two of the sites are adjacent to Glu198 in each subunit while the third is present in 1 subunit, adjacent to the NAD^+ binding site, near Arg161 and Arg730, although it is not as well defined and of lower occupancy. It must be noted that not all crystals contained INH when grown under identical co-crystallization conditions with older crystals generally having less or no INH evident (Table 5.3). This was attributed to the degradation

Table 5.2. Data collection and structural refinement statistics for BpKatG with INH bound.

Data collection statistics	**BpKatG-INH**
Space group	$P2_12_12_1$
Unit cell parameters	
a (Å)	100.1
b (Å)	113.3
c (Å)	174.6
α, β, γ (°)	90, 90, 90
Resolution (Å)	33.3-2.09 (2.21-2.09)[a]
Unique reflections	115,829
Completeness (%)	99.4 (96.9)
R_{sym}[b]	0.094 (0.372)
$\langle I/\sigma I \rangle$ (%)	9.9 (3.0)
Multiplicity	4.2 (3.8)
Model refinement statistics	
No. of reflections	109,936
R_{cryst} (%)[c]	15.9
R_{free} (%)[d]	19.7
Non hydrogen atoms	12,381
Water molecules	1205
Average *B*-factor (Å^2)	
Protein	18.2
Heme group	14.1
Waters	26.1
Est. coordinate error (Å)[e]	0.101
Rms deviations	
In bonds (Å)	0.022
In angles (º)	1.69

[a]Values in parentheses correspond to the highest resolution shell.
[b]$R_{sym} = \Sigma_{hkl} \Sigma_j |I_{hkl,j} - \langle I_{hkl} \rangle| / \Sigma_{hkl} \langle I_{hkl} \rangle$.
[c]$R_{cryst} = \Sigma ||F_{obs}| - |F_{calc}|| / \Sigma |F_{obs}|$.
[d]R_{free} is as for R_{cryst} but calculated for a test set of reflections not used in the refinement.
[e]Based on maximum likelihood.

Table 5.3. Comparison of data collection, structural refinement statistics and INH occupancy for a number of BpKatG crystals with INH bound or INH and NAD^+ bound together.

	INH 01	**INH 02**	**INH 03**	**NAD^+ INH 01**	**NAD^+ INH 02**	**NAD^+ INH 03**
Age	4 days[a]	14 days	>30 days	6 days	13 days	>30 days
E198 INH occupancy	80 % A[b] 100 % B[b]	30 % A 60 % B	<10 % A <10 % B	20 % A 80 % B	<10 % A 20 % B	<10 % <10 %
INH at R161	yes [1][c]	yes [1]	yes [2]	no	yes [1] weak	yes [2]
Resolution (Å)	33.3-2.09 (2.21-2.09)[d]	34.9-2.09 (2.21-2.09)	38.6-1.92 (2.02-1.92)	34.9-1.90 (2.00-1.90)	28.6-2.00 (2.11-2.00)	38.6-1.60 (1.69-1.60)
Completeness (%)	99.4 (96.9)	99.4 (97.7)	99.9 (99.9)	99.3 (98.3)	99.8 (99.9)	100.0 (100.0)
R_{merge}	0.094 (0.372)	0.148 (0.652)	0.113 (0.582)	0.108 (0.591)	0.104 (0.314)	0.091 (0.505)
$\langle I/\sigma I \rangle$ (%)	9.9 (3.0)	9.1 (2.2)	9.0 (2.6)	9.4 (2.3)	11.4 (4.8)	10.7 (3.1)
Multiplicity	4.2 (3.8)	5.0 (4.3)	4.6 (4.5)	4.8 (4.3)	5.7 (5.3)	5.3 (5.2)

[a]The length of time from crystal drops being spotted to the crystal being picked and frozen in liquid N_2.
[b]Refers to the protein subunits A and B.
[c]One or 2 conformation of INH as described in Fig. 5.5 B and C.
[d]Values in parentheses correspond to the highest resolution shell.

of INH which would occur over time reducing its effective concentration. In addition, this reaction might also be responsible for the slightly poorer data collection and refinement statistics of crystals grown in the presence of INH.

The first INH binding site, present in both subunits, is adjacent to Glu198 and Gln622 at the end of a funnel shaped channel close to the sodium ion binding site, essentially on the opposite side of the subunit from the heme entrance channel. A number of side chain adjustments have occurred to accommodate the insertion of a negatively charged ion, most likely a chloride, and INH. The key adjustment is the new conformation of the Glu198 side chain which allows the chloride ion to bind where the carboxylate group was originally situated. The identification of the ion as chloride is based on 1) satisfactory refinement as a chloride, 2) its association via 1 water with the pre-existing sodium ion, and 3) its absence from crystals grown in co-crystallization buffer lacking chloride. The new location of Glu198 places its carboxylate 2.6 Å from the carboxylate of Glu128, suggesting a shared proton. Other changes include the movement of His55 to be associated (2.8 Å) with the carboxylate of Glu198, and of Gln622 to avoid close contacts with the INH. The density corresponding to a molecule of INH is clearly visible in the F_o-F_c omit maps (Fig. 5.3). The apparent interactions include the INH carbonyl oxygen being 2.9 Å from the Nε of Arg123, the INH N2 being 3.2 Å from carboxylate of Glu198 and the INH N1 being 3.4 Å from the chloride ion. The movement of Gln622 removes it from having any contact with the INH although it does form one side of the pocket into which the INH is inserted. Despite the binding pockets in subunits A and B being essentially

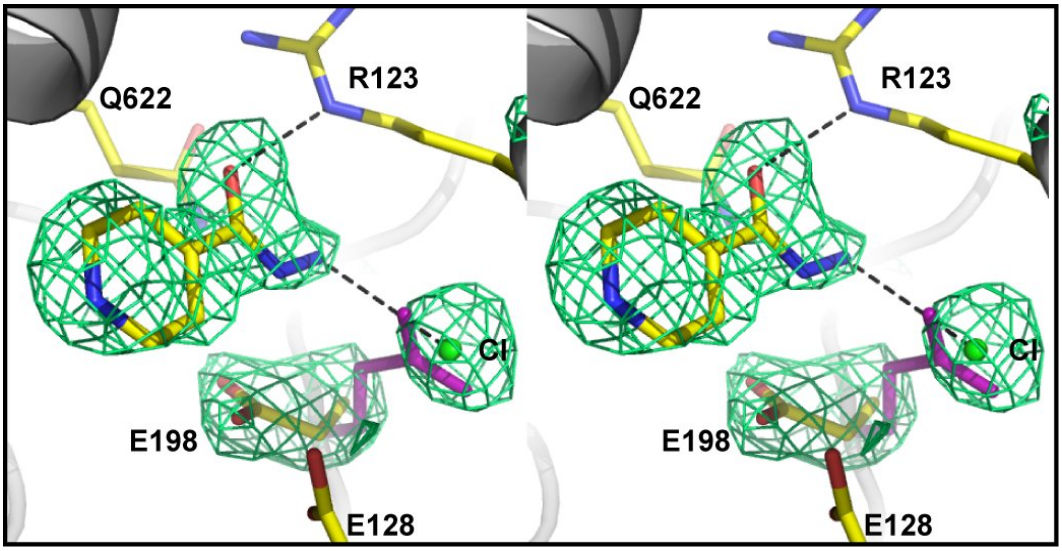

Figure 5.3. Stereo view of the Glu198 INH binding site and position of Glu198 with (yellow) and without (purple) INH bound. The F_o-F_c omit electron density maps were calculated using a model lacking INH and drawn at $\sigma = 3.0$ in green.

identical, occupancy was invariably higher in subunit B. However as described below, occupancy of INH in S324T was essentially 100 % in both subunits suggesting that it is the rate of INH turnover that affects the occupancy, but it is not clear why there would be greater reactivity in one subunit over the other.

The other binding location adjacent to Arg161 and Arg730, near the NAD^+ binding site (Fig. 5.4 A), is evident in only the B subunit, possibly because it is stabilized by interactions at the crystal interface. Unlike the binding site near Glu198, there always appeared to be some INH occupancy at this location although it was frequently disordered making model placement ambiguous and the density maps were usually satisfied by no more than 80 % occupancy. Two examples of this heterogeneous situation are shown in Fig. 5.4. The F_o-F_c omit maps in panel B fit the model of a single INH conformation whereas the maps in panel C best fit 2 overlapping orientations with weaker density associated with the putative hydrazide portions. Indeed, some of the electron density maps could be considered to be consistent with INH degradation products such as isonicotinyl aldehyde. Here again, there is a correlation with the length of time of crystal growth and the fit of the INH with increasing disorder or possibly degradation over time.

There is only 1 polar interaction between the INH carbonyl oxygen and the guanidinium group of Arg161 (2.9 Å). Of the hydrogens on the pyridine ring, only the one on C3/C5 is involved in a van der Waals contact (C3/C5 is 3.4 Å from Cγ of Pro396 in the symmetry related subunit). It should be noted that the second site overlaps the region of poorly structured electron density in the maps

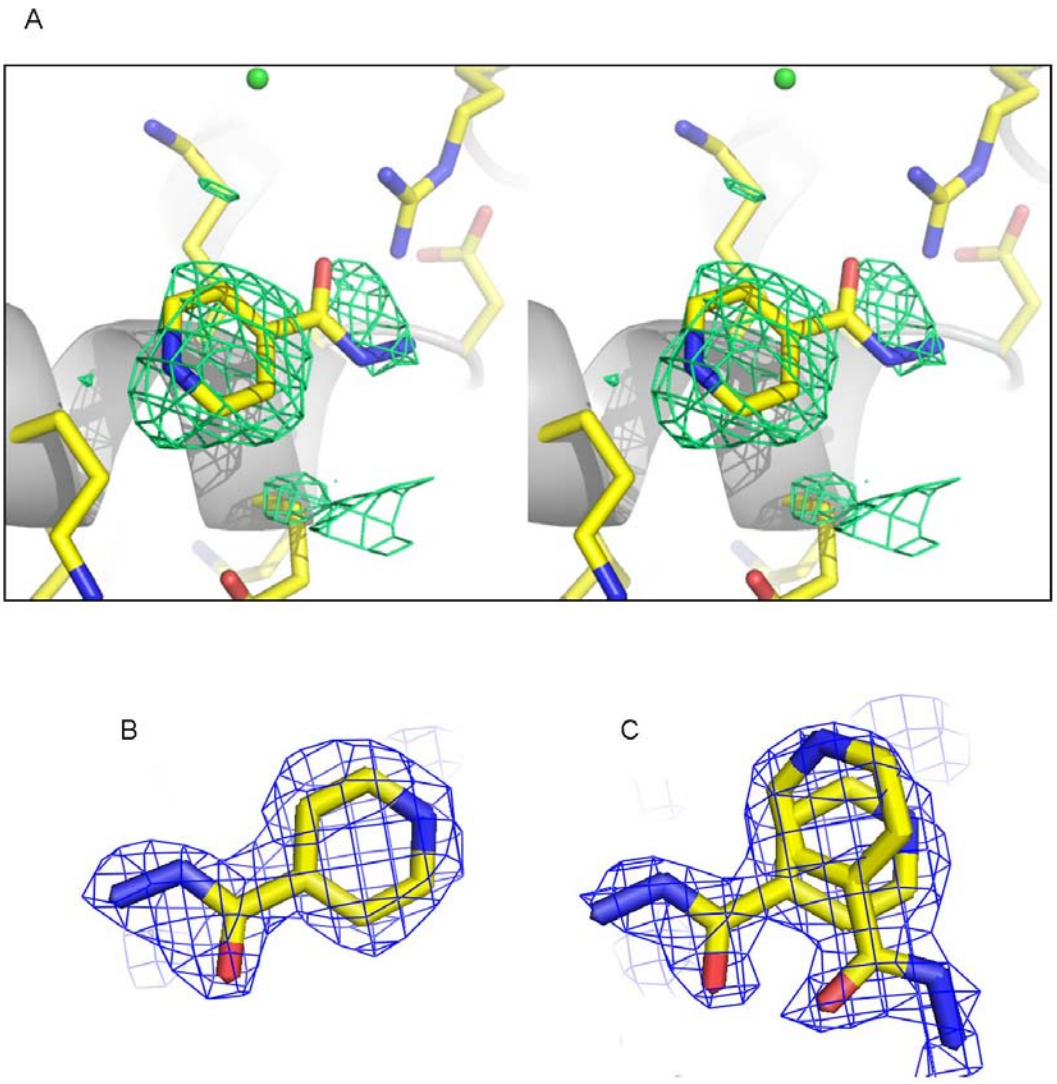

Figure 5.4. Stereo view of the Arg161 and Arg730 INH binding site (panel A). Panel B: INH in a single conformation. Panel C: INH in 2 overlapping orientations. The F_o-F_c omit electron density maps were calculated using a model lacking INH and drawn at $\sigma = 3.0$ in green (panel A) and blue (panels B and C).

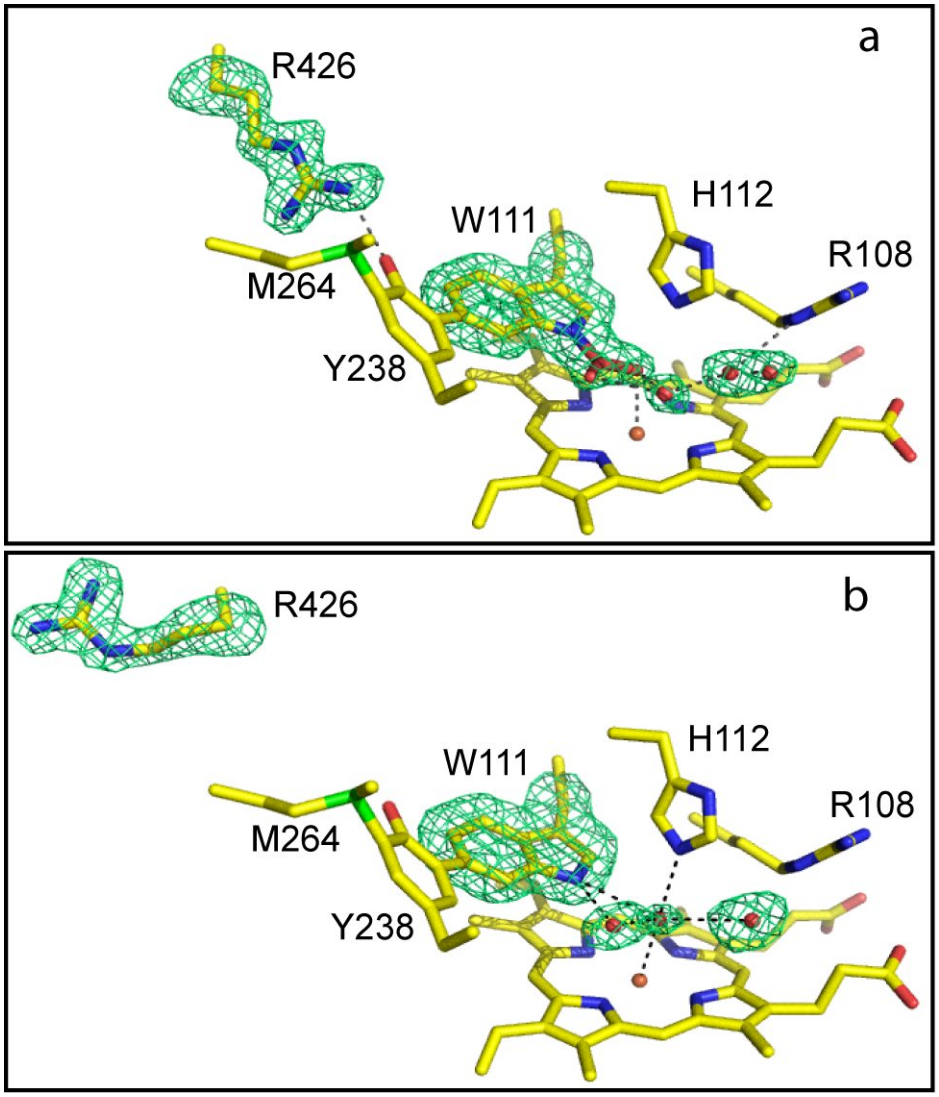

Figure 5.5. Comparison of the heme environment in crystals grown in the absence (panel a) and presence (panel b) of INH. The F_o-F_c electron density maps were calculated using a model lacking Trp111 without (a) and with the perhydroxy modification (b), Arg426 (both a and b) and the indicated waters are drawn at σ = 3.0 in green. A model containing the omitted residues and waters is superimposed.

of BpKatG-NAD^+ that was tentatively attributed to the partially disordered nicotinamide portion of NAD^+. This is consistent with attempts to co-crystallize BpKatG with both NAD^+ and INH resulting in even weaker electron density in this region than is observed with either ligand separately, suggesting possible competition between the nicotinamide of NAD^+ and INH for the site (Table 5.3).

Finally, 2 additional changes were observed in the protein structure of every crystal grown in the presence of INH. The first was the absence of the perhydroxy modification on the indole nitrogen of Trp111 (N-OOH) first noticed in S324T (Deemagarn *et al*, 2005) compared to crystals grown without INH but in the same buffer. The second change involves the side chain of Arg426 moving from >70 % association with Tyr238 of the Met-Tyr-Trp adduct (Y orientation) in the absence of INH to >90 % occupancy of the R orientation in the presence of INH as shown in Fig. 5.5. Changes at these 2 locations had previously been linked to changes in pH and oxidation state (See Chapter 3, and Carpena *et al*, 2005 and 2006), and suggest the existence of an electron transfer pathway between the heme and at least one of the INH binding sites.

5.2.3. Crystal structures of S324T and E198A with INH bound

A major challenge in rationalizing the role of KatG in INH activation is to provide an explanation for INH resistance caused by the S315T variant of MtKatG. The only change in the variant caused by the mutation is a narrowing of the access channel leading to the heme cavity such that even water occupancy is reduced (Deemagarn *et al*, 2005, and Zhao *et al*, 2006), but the remoteness of INH binding from the heme cavity precludes the original explanation that the

Table 5.4. Data collection and structural refinement statistics for S324T with and without INH bound.

Data collection statistics	**S324T**[f]	**S324T-INH**
Space group	$P2_12_12_1$	$P2_12_12_1$
Unit cell parameters		
a (Å)	100.3	99.8
b (Å)	116.0	113.4
c (Å)	174.7	173.3
α, β, γ (°)	90, 90, 90	90, 90, 90
Resolution (Å)	31.3-1.8 (1.90-1.80)[a]	33.2-1.9 (2.00-1.90)
Unique reflections	164,513	154,832
Completeness (%)	88.0 (78.4)	100.0 (100.0)
R_{sym}[b]	0.088 (0.380)	0.242 (0.90)
$\langle I/\sigma I \rangle$ (%)	9.7 (2.6)	4.8 (1.8)
Multiplicity	3.8 (3.1)	6.6 (6.5)
Model refinement statistics		
No. of reflections	156,314	147,103
R_{cryst} (%)[c]	15.9	18.6
R_{free} (%)[d]	19.5	22.6
Non hydrogen atoms	12,732	12,560
Water molecules	1524	1357
Average *B*-factor (Å^2)		
Protein	12.7	16.6
Heme group	8.4	26.0
Waters	21.7	11.6
Est. Coordinate error (Å)[e]	0.068	0.094
Rms deviations		
In bonds (Å)	0.025	0.024
In angles (º)	1.85	1.87

[a]Values in parentheses correspond to the highest resolution shell.
[b]$R_{sym} = \Sigma_{hkl} \Sigma_j |I_{hkl,j} - \langle I_{hkl} \rangle| / \Sigma_{hkl} \langle I_{hkl} \rangle$.
[c]$R_{cryst} = \Sigma ||F_{obs}| - |F_{calc}|| / \Sigma |F_{obs}|$.
[d]R_{free} is as for R_{cryst} but calculated for a test set of reflections not used in the refinement.
[e]Based on maximum likelihood.
[f]From Deemagarn *et al*, 2005 (PBD id. 1X7U).

Table 5.4. Data collection and structural refinement statistics for E198A with and without INH bound.

Data collection statistics	**E198A**	**E198A-INH**
Space group	$P2_12_12_1$	$P2_12_12_1$
Unit cell parameters		
a (Å)	100.3	100.6
b (Å)	116.0	115.9
c (Å)	174.7	174.7
α, β, γ (°)	90, 90, 90	90, 90, 90
Resolution (Å)	29.1-1.6 (1.69-1.60)[a]	29.1-1.7 (1.79-1.70)
Unique reflections	267,486	204,869
Completeness (%)	100.0 (100.0)	91.8 (79.1)
R_{sym}[b]	0.084 (0.550)	0.102 (0.451)
$\langle I/\sigma I \rangle$ (%)	11.9 (2.8)	8.9 (2.3)
Multiplicity	5.9 (5.5)	5.3 (4.6)
Model refinement statistics		
No. of reflections	253,932	194,460
R_{cryst} (%)[c]	16.0	15.5
R_{free} (%)[d]	18.7	18.5
Non hydrogen atoms	13,038	12,718
Water molecules	1861	1555
Average *B*-factor (Å^2)		
Protein	13.2	13.7
Heme group	9.7	9.5
Waters	24.7	24.3
Est. Coordinate error (Å)[e]	0.093	0.052
Rms deviations		
In bonds (Å)	0.022	0.027
In angles (º)	1.73	2.00

[a]Values in parentheses correspond to the highest resolution shell.
[b]$R_{sym} = \Sigma_{hkl} \Sigma_j |I_{hkl,j} - \langle I_{hkl} \rangle| / \Sigma_{hkl} \langle I_{hkl} \rangle$.
[c]$R_{cryst} = \Sigma ||F_{obs}| - |F_{calc}|| / \Sigma |F_{obs}|$.
[d]R_{free} is as for R_{cryst} but calculated for a test set of reflections not used in the refinement.
[e]Based on maximum likelihood.

narrower channel restricts entry of INH. Also, as described above, in order to bind INH at the Glu198 site a number of side chain adjustments have to occur with the adoption of a new conformation of the Glu198 side chain being the key to accommodate INH. To that end, the analogous S324T variant along with the variant E198A were crystallized in the presence of INH. Brownish parallelepiped shaped crystals reaching about 0.5 x 0.2 x 0.2 mm in size of both variants with and without INH were obtained within a few days and were indistinguishable from the previously described native crystals (Carpena *et al*, 2002). Similar to native crystals, crystals of S324T and E198A with and without INH belonged to the orthorhombic space group $P2_12_12_1$ and contained a dimer in the asymmetric unit. The diffraction data sets were refined to 1.90 Å for S324T with INH, and 1.60 and 1.70 Å for E198A with and without INH respectively (Tables 5.4 and 5.5).

As noted above, the crystals of S324T grown in the presence of INH clearly show INH bound at both locations at near 100 % occupancy, much higher than even the best wild-type enzyme crystal complex that contained no more than 80 % INH occupancy. INH binding in S324T is identical to that described for the wild-type enzyme with the only exception being that S324T crystals grown in the presence of INH do not have the slightly poorer data collection and refinement statistics that were observed with the wild-type enzyme. This is consistent with the greatly reduced INH lyase activity reported in this variant which would not reduce the effective INH concentration, with the result that there would be less

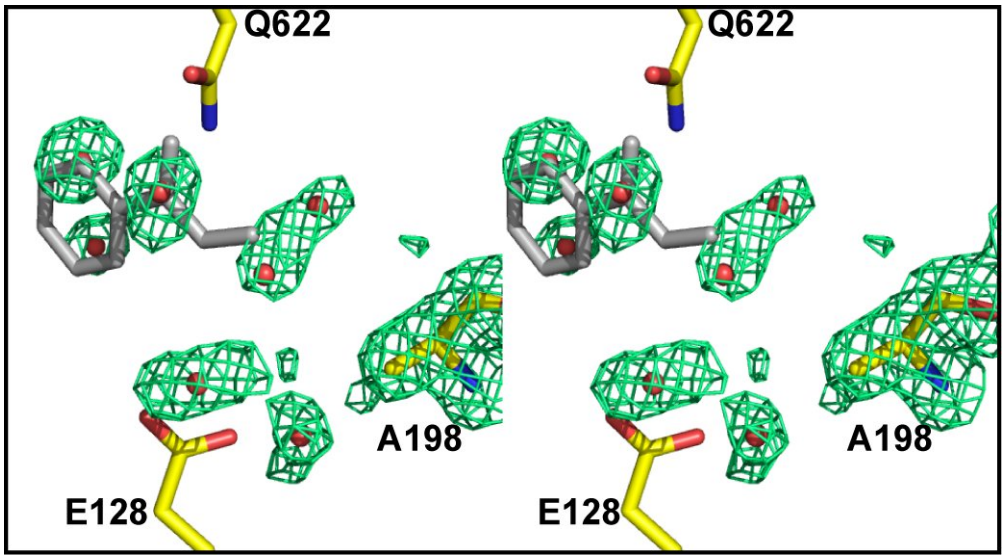

Figure 5.6. Stereo view of the Glu198 INH binding site and position of the mutated Ala198 residue in crystals of E198A grown in the presence of INH showing no INH binding. For comparison, superimposed is the position of bound INH as seen in the wild-type enzyme (grey). The F_o-F_c omit electron density maps were calculated using a model lacking Ala198 and indicated waters are drawn at $\sigma = 3.0$ in green. A model containing the omitted residues and waters is superimposed.

reaction to create a disordered crystal that was reflected in poorer refinement statistics seen in the wild-type protein crystals with INH.

Crystals of E198A clearly show the presence of an alanine in place of the longer, negatively charged glutamate creating a slightly larger entrance to the funnel shaped channel (Fig. 5.6) consistent with the mutation. Crystals of E198A grown in the presence of INH revealed no INH or chloride binding at the Glu198 location, but did have some new density adjacent to Arg161. However, as described for the wild-type enzyme, some electron density maps here could also be considered to be consistent with INH degradation products such as isonicotinyl aldehyde suggesting that INH cleavage may occur at more than one location.

5.3. Discussion

The INH binding sites identified here are not in the heme cavity as predicted by work with eukaryotic peroxidases (Metcalfe *et al*, 2008, and Singh *et al*, 2009). The first INH binding site, near Glu198, is at the end of a funnel shaped channel and requires the movement of Glu198 for INH to bind. The apparent interactions between INH and the protein include the INH carbonyl oxygen being 2.9 Å from the Nε of Arg123, the INH N2 being 3.2 Å from the carboxylate of Glu198 and the INH N1 being 3.4 Å from the chloride ion. This is consistent with the STD-NMR results (Wiseman *et al*, in preparation), predicting that all 4 protons of the pyridine ring are involved in van der Waals contacts with C2, C3, C5 and C6 all being within 3.3 to 3.6 Å of either the carboxylate of Glu128 or the main chain carbonyl oxygen of Gln622.

The second INH binding site is located near Arg161, Arg730, and the NAD^+ binding site. Unlike the first INH binding site near Glu198, no clear pathway for electrons to travel to the heme has so far been identified for this site. However, its proximity to the NAD^+ site suggests that one must exist, because electrons must be transferred from NADH at the same site to the heme during NADH oxidation. Also, this site is located at the crystal interface between 2 protein dimers, a location where INH binding might be enhanced by interactions between the two interacting proteins. The fact that the NAD^+ binding site is nearby and in a spot where the nicotinamide of NAD^+ may be located, albeit poorly defined, suggests this may be the site of the IN-NAD synthesis reaction and that INH alone is simply binding where the isonicotinoyl part of the IN-NAD adduct would fit when the whole IN-NAD is present. Thus not surprisingly, when both NAD^+ and INH were co-crystallized together, the complete IN-NAD adduct has never been seen in the electron density maps and in fact both ligands show much lower occupancy than when crystallized separately since not only does the nicotinamide portion of NAD and INH compete for this site effectively reducing the binding of each, the IN-NAD synthesis reaction would be reducing the concentrations of both ligands lowering their effective concentrations. It also seems likely that the addition of the extra bulk of isonicotinoyl to NAD to create the final IN-NAD would cause it to become unbound from the protein.

Whereas the previous studies on eukaryotic peroxidases have suggested that INH binds in the heme cavity (Henriksen *et al*, 1998, Metcalfe *et al*, 2008, and Singh *et al*, 2009), the binding sites described here are quite removed from

the heme active site. Also, the fact that the leading cause of INH resistance is the S315T mutation located in the main access channel further suggested that INH activation occurs in or near the heme cavity. However, recent EPR results have revealed that INH reduced Trp radicals are well removed from the heme cavity in MtKatG (Singh *et al*, 2007). In fact, the idea that KatGs might bind INH outside the heme cavity is not surprising since KatGs have a much longer and more constricted access channel leading to the heme active site compared to eukaryotic peroxidases and this would make INH access much more difficult. However, a remote binding site presents a challenge in explaining the IN-NAD synthesis capabilities of KatGs, and in explaining the INH resistance imparted by the S315T mutation. This unusual IN-NAD synthesis reaction is much slower than the catalase and peroxidase reactions ($<10^{-5}$ and $<10^{-2}$, respectively (Singh *et al*, 2008)) and does not require external oxidants such as hydrogen peroxide or peroxyacetic acid (Singh *et al*, 2004) suggesting that INH activation does not occur via the peroxidase reaction cycle as previously assumed.

A recently discovered electron pathway linking the heme and Trp139 supports the first site near Glu198 as being a physiologically relevant binding site for INH (Colin *et al*, 2009). Trp139, Trp330, and Trp153 have recently been identified as 3 sites where stable oxoferryl-Trp$^{\bullet}$ intermediates are formed in the peroxidase reaction of BpKatG (Colin *et al*, 2009), and 2 separate electron transfer pathways were concluded to be linking Trp139 (via Trp111) and Trp153 (via Trp94 and Trp95), respectively, with the heme and Trp330. As shown in Fig. 5.7, the Trp139-Trp111 pathway provides a route for electrons to travel from the

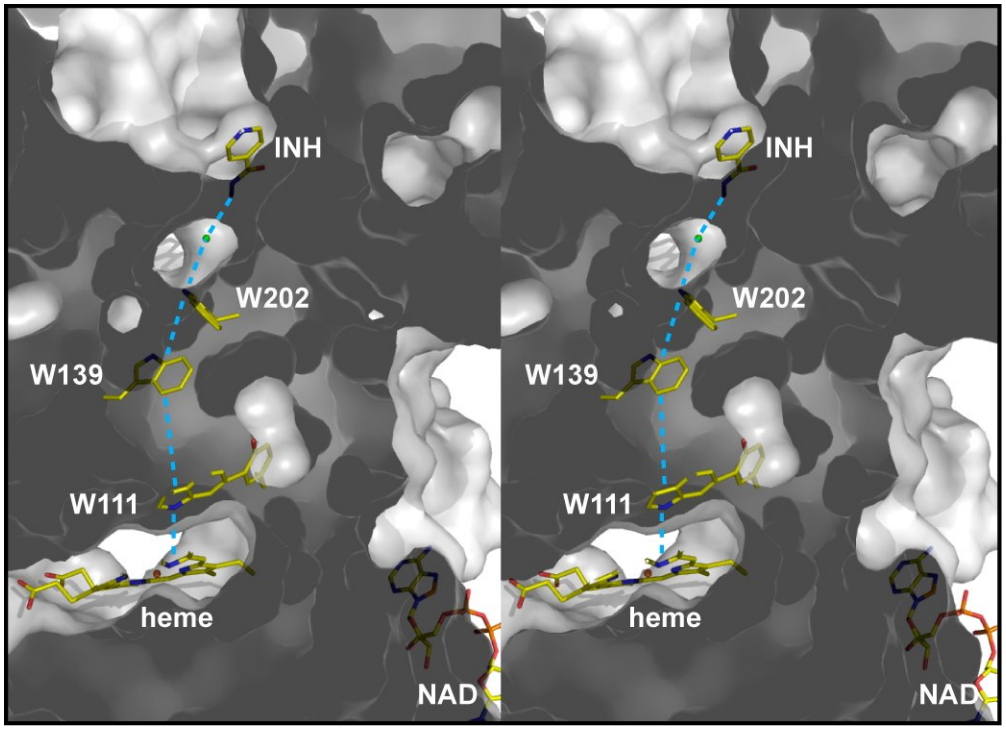

Figure 5.7. Stereo view of the surface of BpKatG and the NAD^+ and INH binding sites in relation to the heme active site and Trp139-Trp111 pathway.

INH bound near Glu198 and the heme. Changes in the structure of the heme cavity caused by INH including the loss of the perhydroxy modification on Trp111 and shift of the mobile Arg426 from >70% Y conformation (associated with Tyr238 of the adduct) to >90% R conformation (shifted away from Tyr238) are consistent with a change in electron balance caused by electrons from INH and superoxide formation (Carpena *et al*, 2005).

A link between superoxide and INH activation has been previously documented, but its role or how it is related to IN-NAD synthesis has never been clarified. It was shown however, that radical production in a KatG/INH mixture was reduced by greater than 60 % by superoxide dismutase (Shoeb *et al*, 1985 and Wengenack *et al*, 1999) suggesting that electrons from INH are used to reduce O_2 to $O_2\bullet^-$. Furthermore, the presence of a perhydroxy modification on Trp111 in both native BpKatG and its variants confirm that the heme cavity is the site of a facile reaction with O_2 and that O_2 binding occurs in the vicinity of Trp111. Thus the Trp139-Trp111 pathway potentially provides a route for electrons to travel between the bound INH at the Glu198 site and O_2 bound near the heme for its reduction to $O_2\bullet^-$.

Similar to the INH binding sites, the NAD^+ binding site described here is not in the heme cavity, or even in the access channel leading to the heme cavity, but on the protein surface located approximately 20 Å from the edge of the opening of the channel (Fig. 5.2 and Fig.5.7). The weak STD-NMR signals (Wiseman *et al*, in preparation) and the slow rate of NADH oxidase (Singh *et al*, 2004) might be considered to be inconsistent with the high occupancy of NAD^+

observed in the crystal, but the discrepancy can be explained by the location of the binding site close to a crystal interface which would reduce protein flexibility and stabilize the binding site. However, even though binding at this site is being enhanced through interactions at the crystal interface in the crystal, the resulting electron density maps are very consistent with independent STD-NMR experiments done in solution (Wiseman *et al*, in preparation) that show only the ADP portion of NAD^+ interacting with the protein. This is further confirmed by structures of both AMP and ADP bound to BpKatG that show virtually identical binding to that seen with NAD^+. Also consistent with the STD-NMR experiments, the nicotinamide portion, which ultimately reacts with the isonicotinoyl radical to form the final NAD-IN adduct, is more disordered in the crystal structure suggesting weaker (if any at all) binding and the poorly defined area of electron density attributed to it is in a location easily accessible to substrates entering or leaving the heme cavity.

The binding site identified for NAD^+ leads to several important conclusions with regards KatG function. First of all, for the NADH oxidase or peroxidase reactions, there must be an electron transfer pathway to move electrons from the surface location to the heme cavity to reduce the oxyferryl species in the peroxidatic reaction or to generate superoxide or H_2O_2, depending on the pH in the oxidase reaction (Singh *et al*, 2004). Second, the isonicotinyl moiety, very likely an isonicotinyl radical must migrate from wherever it is generated on the KatG protein to the NAD^+ binding site for conversion to IN-NAD. Third, the apparent disorder of the nicotinamide portion of NAD^+ suggests

that there is little if any steric constraint placed on it by the protein consistent with the formation of both stereo isomers of IN-NAD, suggesting that the final joining of IN• and NAD is a non-enzymatic event, or at least involves a poorly constrained nicotinamide group.

A mechanism for IN-NAD synthesis, based on the observations of the remote substrate binding location of both NAD^+ and INH (Fig. 5.7), evidence for electron transfer to generate superoxide within the protein, and evidence for superoxide involvement in IN-NAD synthesis, is outlined in Fig. 5.8. INH cleavage generates, separately, the IN• radical and an electron that then travel along parallel reaction paths. The electron is transported via the Trp139-Trp111 pathway (Colin *et al*, 2009) (if generated at the Glu198 site) or by an undefined route (if generated at Arg161 site) to the heme for O_2 reduction to $O_2\bullet^-$, which subsequently diffuses out of the heme cavity. The IN• radicals would have to diffuse to the NAD^+ binding site to generate IN-NAD• which is subsequently reduced by $O_2\bullet^-$ free in solution. Reduction of IN-NAD• by $O_2\bullet^-$ is a favorable reaction based on the standard reduction potentials (E^o) of -0.33 V and +0.3 V for the [$O_2/O_2\bullet^-$] and [H^+, NAD•/NADH] half cell reactions, respectively (Farrington *et al*, 1980).

The identification of INH binding sites greatly removed from the heme active site or access channel all but eliminates the reason for INH resistance previously proposed for the S315T variant of MtKatG which was that INH binding was reduced in the variant. Interestingly, the S324T crystal structure without INH bound contained a perhydroxy modification on Trp111 suggesting

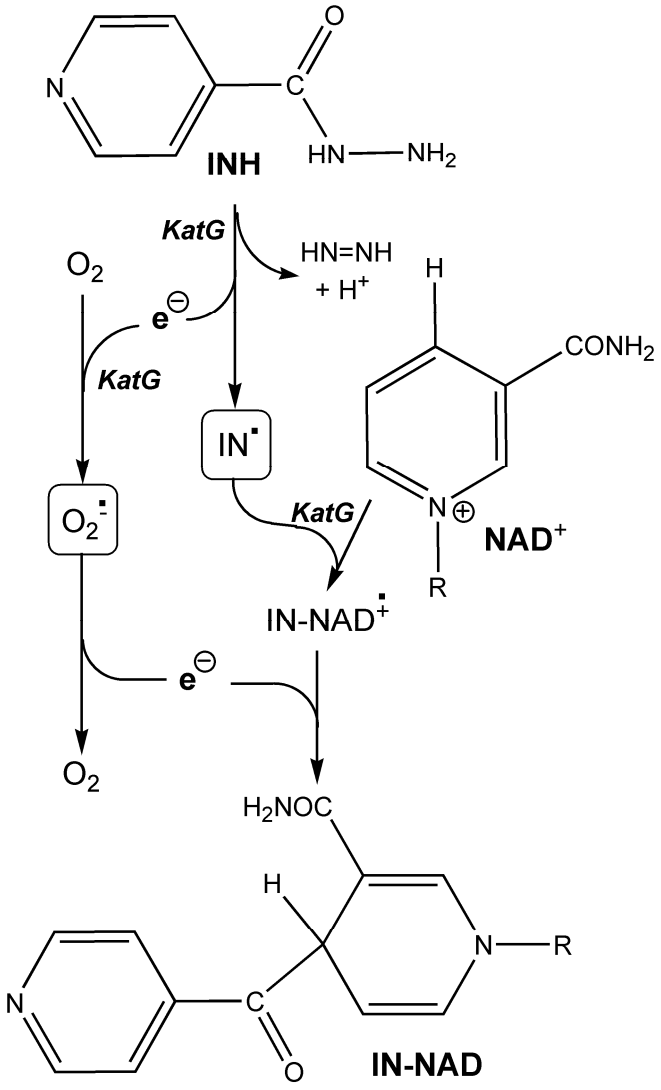

Figure 5.8. A proposed scheme for the synthesis of the IN-NAD adduct catalyzed by KatGs.

that O_2 binds there (Deemagarn *et al*, 2005) and may have a role in the process. The scheme in Fig. 5.8 emphasizes the need for diffusion of $O_2\bullet^-$ out of the cavity (and possibly O_2 diffusion into the cavity) which would be affected by the much narrower access channel in S324T (Deemagarn *et al*, 2005). In addition to physical hindrance, movement through the narrower channel would force the superoxide to pass closer to the negatively charged carboxylate of Asp141 situated in the heme channel (Deemagarn *et al*, 2007). Evidence of 60 % slower $O_2\bullet^-$ diffusion from the S324T variant compared to the native (Deemagarn *et al*, 2005) supports this idea, and in fact INH occupancy in the S324T-INH complexed crystal is much higher in all 3 sites compared to the native complex, consistent with a much slower reaction with INH.

5.4. Conclusion

INH is activated to its anti-tubercular form, IN-NAD, through an unusual combination of enzyme catalyzed and non-catalyzed reactions involving the diffusion of reaction intermediates between sites on the protein. The enzymatic role of KatGs in the process includes the production of $O_2\bullet^-$ and IN•, the internal electron transfer and the binding of NAD^+. The remainder of the process involves the non-enzymatic diffusion of $O_2\bullet^-$ and IN• and their subsequent reaction assisted only by the NAD^+, NAD• and IN-NAD• being bound to the protein. The reaction of $O_2\bullet^-$ with both NAD^+ and IN-NAD• and the formation of both stereoisomers of IN-NAD from the reaction of IN• with either NAD^+ or NAD• speak to the non-specificity evident in the reactions.

NAD^+ was found to bind at the crystal interface about 20 Å from the opening of the main access channel, with only the ADP portion of NAD^+ in contact with the protein, consistent with STD-NMR results (Wiseman *et al*, in preparation). INH was found to bind at 3 locations in crystals of BpKatG, all well removed from the heme cavity and main access channel. Specifically it binds in a funnel shaped channel near Glu198 in both subunits and at the crystal interface near Arg161 and Arg730. The sites near Glu198 involve movement of its side chain to accommodate INH and the Arg161 site is close to the NAD^+ binding site. STD-NMR (Wiseman *et al*, in preparation) and EPR (Colin *et al*, 2009) results are most consistent with the first site, near Glu198 as being a physiologically relevant binding site. The recently discovered Trp139-Trp111 pathway (Colin *et al*, 2009) is implicated in linking INH bound at the Glu198 site to the active site. Electrons from INH travel through this pathway to reduce O_2 bound at Trp111 to produce $O_2\bullet^-$. Finally, this mechanism suggests that the greatly reduced INH activation seen in S324T is due to a reduction in the rate of diffusion of $O_2\bullet^-$ out of the much narrower access channel.

6. CONCLUSIONS

Catalase-peroxidases (KatGs), responsible for the activation of the anti-tubercular prodrug isoniazid (INH), are unusual members of the class I plant peroxidase family that possess strong catalase activity as well as peroxidase activity despite an active site and overall topology similar to other monofunctional peroxidases. Due to their strong catalase activity and their ability to activate INH, KatGs have been the subject of intense study for many years, and thus the goal of this work was to further characterize the enzymatic properties of this enzyme in the hope of gaining a better understanding into these unusual reactions.

6.1. The role of Arg426 and the Met264-Tyr-238-Trp111 adduct

Recent successful crystallization of the catalase-peroxidase from *Burkholderia pseudomallei* (Carpena *et al*, 2003b) and 3 other organisms (Yamada *et al*, 2002, Wada *et al*, 2002, and Bertrand *et al*, 2004) have confirmed their relation to other members of the class I peroxidases, but have also revealed structural features unique to KatGs including the adduct of Trp111-Tyr238-Met264, a mobile Arg426 that associates with Tyr238, and Asp141 located in the main access channel at the entrance to the heme active site. Previous studies had confirmed that removing any of these residues dramatically abolishes catalase activity with little to no affect on peroxidase activity.

Together with previous studies (Deemagarn *et al*, 2007) showing that Asp141, located at the entrance to the heme active site, promotes catalase activity by directing the incoming hydrogen peroxide to alternate binding sites for either

compound I formation (Arg108-His112) or compound I reduction (Trp111-His112), the switch-like movement of Arg426 described in chapter 3 can potentially explain the robust catalase activity that has been built into a peroxidase core. This molecular switch modulates the reactivity by shifting electrons into the active site and favouring oxidation to compound I when Arg426 is toggled in the R conformation (away from Tyr238) and pulling electrons out of the active site to favour compound I reduction when Arg426 is toggled to the Y conformation (in association with Tyr238). Thus, Arg426 influences the heme reaction center through its ionic interaction with Tyr238, an association made possible by the pKa of the Tyr having been lowered close to physiological pH by the Met-Tyr-Trp adduct structure.

Unfortunately, attempts to crystallize variants of the Trp111-Tyr238-Met264 adduct or even the mobile Arg426 have so far been unsuccessful. There has been an initial report of successful crystallization of the variant Met244Ala of the KatG from *Haloarcula marismortui* (Ten-I *et al*, 2007) but to date no structure has been released. It is already known from mass spectrometry that the Tyr-Trp portion of the adduct will still be intact (Jakopitsch *et al*, 2003b, and Ghiladi *et al*, 2005b), but the position of the analogous Arg426 in this variant would be interesting since it is speculated that the lack of catalase activity in this variant is caused by the return of a pKa for Tyr238 back to that of a typical tyrosine residue which prevents Arg426 from associating with it at physiological pH. Crystal structures of the variants of the Trp111-Tyr238-Met264 adduct would undoubtedly help confirm this, but larger crystal screenings would be required

since it appears they will not crystallize under wild-type enzyme conditions. If crystals can be produced, similar experiments of soaking crystals at varying pHs prior to X-ray data collection as done for the wild-type enzyme (Carpena *et al*, 2006) could be done to monitor the position of Arg426 and thus the pKa of Tyr238 in these variants. Also, the complete lack of catalase activity in these variants could make their crystals amenable to soakings with hydrogen peroxide prior to X-ray data collection to potentially see enzyme complexes with hydrogen peroxide.

6.2. Stopped-flow characterization with peroxyacetic acid and the influence of pH

The robust catalase activity of KatGs makes studying reaction intermediates with the natural substrate hydrogen peroxide difficult. To overcome this problem organic peroxy-acids are often used in order to trap and study the reaction intermediates. Interestingly, analysis of the reaction of BpKatG with peroxyacetic or 3-chloroperoxybenzoic acid using stopped-flow spectrophotometry revealed an initial, rapidly formed enzyme-substrate complex before the formation of the oxoferryl compound I. Kinetic characterization revealed that formation of both the enzyme-substrate complex and the oxoferryl species were dependent on peroxyacetic acid concentration implying that 2 molecules of peroxyacetic acid are required to form the typical oxoferryl compound I intermediate.

Whether this mechanism of 2 molecules of peroxyacetic acid being required for the formation of compound I can be applied to the natural substrate of

hydrogen peroxide is unknown, although the mechanism outlined in chapter 3 suggests that it is not. Unfortunately, the robust catalase activity seen in catalase-peroxidases makes studying any intermediates that may exist prior to compound I formation difficult with a traditional stopped-flow instrument. Even in monofunctional peroxidases, that lack any catalase activity, the formation of compound I with hydrogen peroxide is so rapid that spectroscopic evidence of a Por Fe-H_2O_2 complex prior to the formation of compound I is elusive. The fact that this 2-step pathway to compound I is seen with both peroxyacetic acid and 3-chloroperoxybenzoic acid suggests that it could be applied to all peroxy-acids, and additional studies with a few more peroxy-acids could easily confirm this.

The reaction with peroxyacetic acid also revealed that the electronic structure of compound I appears to be an equilibrium between protein and porphyrin radicals with a pH dependence. Absorption spectra of the reaction between BpKatG and PAA revealed a clear trend to a larger proportion of the $Por^{\bullet+}$ Fe^{IV}=O species as the pH increased and a greater proportion of Por Fe^{IV}-OH $Trp^{\bullet+}$ as the pH decreased. Simple monitoring of the absorption spectra as compound I is generated at one pH followed by a rapid change to another pH could easily be performed on a traditional stopped-flow instrument equipped with a sequential mixer.

The apparent correlations between the conformation of Arg426 and also the electronic structure of compound I with pH can potentially explain the characteristic pH optima for the peroxidase (pH 4.5) and catalase (pH 6.5) reactions of KatGs. At acidic pH, where the peroxidase reaction is at its

maximum, Tyr238 will be protonated, Arg426 will be predominately in the R conformation, and there will be a larger proportion of protein radicals. The peroxidase reaction, only using hydrogen peroxide for compound I formation is facilitated at acidic pH when Arg426, in conformation R, favours heme oxidation to compound I, but not its reduction. In addition, the greater proportion of protein radicals at acidic pH will facilitate the oxidation at sites remote from the heme of bulky peroxidase substrates that would not be able to bind near the heme active site. At near neutral pH, where the catalase reaction is at its maximum, there will be an equilibrium between protein and porphyrin radicals, and R and Y conformations of Arg426, allowing both the formation and reduction of compound I with hydrogren peroxide. The neutral pH allows for optimal toggling of Arg426 between both conformations and the availability of porphyrin radicals needed in the catalase reaction. Consequently, at basic pH, even though there will be a greater proportion of porphyrin radicals needed for the catalase reaction, Arg426 will be predominately in the Y conformation favoring heme reduction with hydrogen peroxide, but not its oxidation.

6.3. Co-crystallization of BpKatG with INH and NAD^+

Finally, the identification of the binding sites for the anti-tubercular prodrug isoniazid (INH) and its co-substrate, NAD^+, required for the synthesis of the active form of INH, isonicotinoyl-NAD potentially answers many of the questions regarding KatG's role in this unusual reaction. The structures suggest that an unusual combination of enzymatic and nonenzymatic reactions is needed to produce the final antimicrobial compound. The enzymatic role of KatG in INH

activation includes INH binding, the production of the isonicotinoyl and superoxide radicals, and the binding of NAD^+. A nonenzymatic coupling to form the final IN-NAD adduct occurs once the isonicotinoyl radical diffuses from the INH binding site and is facilitated by the ability of this enzyme to bind both INH and NAD^+ bringing the two molecules in close contact. The identification of 3 INH binding sites, all on the opposite side of the protein from the access channel and the binding of only the ADP portion of NAD^+ on the surface of the protein, about 20 Å from the opening of the main access channel, all suggest the unspecific and very slow reaction seen in the formation of the final active IN-NAD product.

The leading cause of INH resistance in *Mycobacterium tuberculosis* is the point mutation S315T which results in a much narrower main access channel leading to the heme active site compared to the wild-type enzyme. The identification of INH binding sites well removed from the main access channel and heme cavity strongly suggests that the narrowing of the channel cannot be affecting INH access to the heme cavity and therefore its reaction. An alternative explanation for the physiological effect of the S315T mutation lies in its effect on superoxide diffusion which is generated in the heme cavity but required for IN-NAD synthesis outside of the cavity. The narrower channel would interfere with superoxide diffusion out of the cavity, thereby providing an explanation for INH resistance in the variant and clarifying the role of superoxide in INH activation.

These structures for the first time demonstrate INH and NAD^+ binding in a catalase-peroxidase, but many questions remain unanswered. For example, the

role of Mn ion is not immediately apparent. Is Mn actively binding to KatGs and acting as a co-enzyme in the activation of INH, or is it acting independently in a nonenzymatic reaction to activate INH? In addition, the significance of multiple INH binding sites requires investigation. Multiple binding sites are perhaps not surprising given the small size of INH that has already been shown to bind to ascorbate peroxidase at 2 locations, one at the heme edge and one on the surface (Metcalfe *et al*, 2008). Also, previous EPR studies have identified various protein based radicals (Singh *et al*, 2007) whose location is unknown but are quenched in the presence of INH. Structure guided site-directed mutagenesis of many of the key residues in these newly discovered binding sites is the first and most obvious step in confirming which sites are physiologically relevant by hopefully producing variants that are incapable of INH activation. If there are in fact multiple INH binding sites however, this may require the creation of double or triple mutants to actually reduce the rate of activation. Determination of the locations of the other protein based radicals should also help in determining other potential electron transfer routes between INH and the enzyme similar to the one described for the Glu198 binding site and the Trp139-Trp111 pathway. Similar EPR studies to those described by Singh *et al* (2007) using these variants (for example variants of Trp139 and/or Glu198) might hopefully independently confirm these binding sites.

7. REFERENCES

Abelskov, A.K., Smith, A.T., Rasmussen, C.B., Dunford, H. B., and Welinder, K.G. (1997) pH dependence and structural interpretation of the reactions of *Coprinus cinereus* peroxidase with hydrogen peroxide, ferulic acid, and 2,2'-azinobis. *Biochemistry* **36:** 9453–9463.

Ahmad, S., and Mokaddas, E. (2004) Contribution of AGC to ACC and other mutations at codon 315 of the *katG* gene in isoniazid-resistant *Mycobacterium tuberculosis* isolates from the Middle East. *Int. J. Antimicrob. Agents.* **23:** 437-479.

Ausubel, F.M., Brent, R., Kingston, R.E., Moore, D.D., Seidman, J.G., Smith, J.A., and Strunhl, K. (1989) *Current Protocols in Molecular Biology.* Green Publishing-Wiley Interscience. New York.

Baker, R.D., Cook, C.O., and Goodwin, D.C. (2004) Properties of catalase-peroxidase lacking its C-terminal domain. *Biochem. Biophys. Res. Commun.* **320:** 833-839.

Baker, R.D., Cook, C.O., and Goodwin, D.C. (2006) Catalase-peroxidase active site restructuring by a distant and "inactive" domain. *Biochemistry* **45:** 7113-7121.

Banerjee, A., Dubnau, E., Quemard, A., Balasubramanian, V., Um, K.S., Wilson, T., Collins, D., de Lisle, G., Jacobs, W.R. Jr. (1994) InhA, a gene encoding a target for isoniazid and ethionamide in *Mycobacterium tuberculosis*. *Science* **263:** 227-230.

Bardou, F., Raynaud, C., Ramos, C., Lanéelle, M.A., and Lanéelle, G. (1998) Mechanism of isoniazid uptake by *Mycobacterium tuberculosis*. *Microbiology* **144:** 2539-2544.

Berglund, G.I., Carlsson, G.H., Smith, A.T., Szoke, H., Henriksen, A., and Hajdu, J. (2002) The catalytic pathway of horseradish peroxidase at high resolution. *Nature* **417:** 463-468.

Berthet, S., Nykyri, L., Bravo, J., Maté, M.J., Berthet-Colominas, C., Alzari, P.M., Koller, F., and Fita, I. (1997) Crystallization and preliminary structural analysis of catalase-A from *Saccharomyces cerevisiae. Protein Sci.* **6:** 481-483.

Bertrand, T., Eady, N.A.J., Jones, J.N., Nagy, J.M., Jamart-Grégoire, B., Raven, E.L., and Brown, K.A. (2004) Crystal structure of *Mycobacterium tuberculosis* catalase-peroxidase. *J. Biol. Chem.* **279:** 38991-38999.

Bhaskar, B., Immoos, C.E., Shimizu, H., Sulc, F., Farmer, P.J., and Poulos, T.L. (2003) A novel heme and peroxide-dependent trytophan-tyrosine cross-link in a mutant of cytochrome *c* peroxidase. *J. Mol. Biol.* **328:** 157-166.

Blodig, W., Smith, A.T., Winterhalter, K., and Piontek, K. (1999) Evidence from spin-trapping for a transient radical on tryptophan residue 171 of lignin peroxidase. *Arch. Biochem. Biophys.* **370:** 86-92.

Bonagura, C.A., Bhaskar, B., Shimizu, H., Li, H., Sundaramoorthy, M., McRee, D.E., Goodin, D.B., and Poulos, T.L. (2003) High-resolution crystal structures and spectroscopy of native and compound I cytochrome *c* peroxidase. *Biochemistry* **42:** 5600-5608.

Bravo, J., Mate, M.J., Schneider, T., Switala, J., Wilson, K., Loewen, P.C., and Fita, I. (1999) Structure of catalase HPII from *Escherichia coli* at 1.9 Å resolution. *Proteins* **34:** 155-166.

Bravo, J., Verdaguer, N., Tormo, J., Betzel, C., Switala, J., Loewen, P.C., and Fita, I. (1995) Crystal structure of catalase HPII from *Escherichia coli. Structure* **3:** 491-502.

Campbell, N.A., and Reece, J.B. (2005). *Biology, 7th Edition*. San Francisco: Pearson - Benjamin Cummings.

Carpena, X., Loprasert, S., Mongkolsuk, S., Switala, J., Loewen, P.C., and Fita, I. (2003b) Catalase-peroxidase KatG of *Burkholderia pseudomallei* at 1.7 Å resolution. *J. Mol. Biol.* **327:** 475-489.

Carpena, X., Melik-Adamyan, W., Loewen, P.C., and Fita, I. (2004) Structure of the C-terminal domain of the catalase-peroxidase KatG from *Escherichia coli*. *Acta. Crystallogr.* **D60:** 1824-1832.

Carpena, X., Perez, R., Ochoa, W.F., Verdaguer, N., Klotz, M.G., Switala, J., Melik-Adamyan, W., Fita, I., and Loewen, P.C. (2001) Crystallization and preliminary X-ray analysis of clade I catalases from *Pseudomonas syringae* and *Listeria seeligeri*. *Acta. Crystallogr.* **D57:** 1184-1186.

Carpena, X., Soriano, M., Klotz, M.G., Duckworth, H.W., Donald, L.J., Melik-Adamyan, W., Fita, I., and Loewen, P.C. (2003a) Structure of the clade I catalase, CatF of *Pseudomonas syringae*, at 1.8 Å resolution. *Proteins* **50:** 423-436.

Carpena, X., Switala, J., Loprasert, S., Mongkolsuk, S., Fita, I. & Loewen, P. C. (2002) Crystallization and preliminary X-ray analysis of the catalase-peroxidase KatG from *Burkholderia pseudomallei*. *Acta Crystallog.* **D58:** 2184–2186.

Carpena, X., Wiseman, B., Deemagarn, T., Herguedas, B., Ivancich, A., Singh, R., Loewen, P.C., and Fita, I. (2006) Roles of Arg426 and Trp111 in the modulation of NADH oxidase activity of the catalase-peroxidase KatG from *Burkholderia pseudomallei* inferred from pH-induced structural changes. *Biochemistry* **45:** 5171-5179.

Carpena, X., Wiseman, B., Deemagarn, T., Singh, R., Switala, J., Ivancich, A., Fita, I., and Loewen, P.C. (2005) A molecular switch and electronic circuit modulate catalase activity in catalase-peroxidases. *EMBO reports* **6:** 1156-1162.

Chelikani, P., Carpena, X., Fita, I., and Loewen, P.C. (2003) An electrical potential in the access channel of catalases enhances catalysis. *J. Biol. Chem.* **278:** 31290-31296.

Chelikani, P., Fita, I., and Loewen, P. C. (2004) Diversity of structures and properties among catalases. *Cell. Mol. Life. Sci.* **61:** 192-208.

Childs, R.E., and Bardsley, W.G. (1975) The steady-state kinetics of peroxidase with 2,2-azino-di-(3-ethyl-benzthiazoline-6-sulphonic acid) as chromagen. *Biochem. J.* **145:** 93-103.

Christman, M.F., Morgan, R.W., Jacobson, F.S., and Ames, B.N. (1985) Positive control of a regulon for defenses against oxidative stress and some heat-shock proteins in *Salmonella typhimurium*. *Cell* **41:** 753-762.

Chung, C.T., Niemala, S.L., and Miller, R.H. (1989) One-step preparation of competent *Escherichia coli*: transformation and storage of bacterial cells in the same solution. *Proc. Natl. Acad. Sci. U.S.A.* **86:** 2172-2175.

Claiborne, W., and Fridovich, I. (1979) Purification of the o-dianisidine peroxidase from *Escherichia coli*. Physicochemical characterization and analysis of its dual catalatic and peroxidatic activities. *J. Biol. Chem.* **254:** 4245-4252.

Collaborative Computational Project Number 4. (1994) The CCP4 suite: programs for protein crystallography. *Acta Crystallogr.* **A50:** 760–763.

Colin, J., Wiseman, B., Switala, J., Loewen, P.C., and Ivancich, A. (2009) Distinct role of specific tryptophans in facilitating electron transfer or as [Fe(IV)=O Trp$^{\bullet}$] intermediates in the peroxidase reaction of *Bulkholderia pseudomallei* catalase-peroxidase: a multifrequency EPR spectroscopy investigation. *J. Am. Chem. Soc.* **131:** 8557-8563.

Deemagarn, T. (2004b) Structure-function studies of the catalase-peroxidase BpKatG from *Burkholderia pseudomallei. M.Sc. thesis.* Department of Microbiology. University of Manitoba.

Deemagarn, T. (2008) Structure analyses of KatG mutations imparting isoniazid resistance. *Ph.D. thesis*. Department of Microbiology. University of Manitoba.

Deemagarn, T., Carpena, X., Singh, R., Wiseman, B., Fita, I., and Loewen, P.C. (2004a) Structural Characterization of the Ser324Thr variant of the catalase-peroxidase (KatG) from *Burkholderia pseudomallei*. *J. Mol. Biol.* **345:** 21-28.

Deemagarn, T., Wiseman, B., Carpena, X., Ivancich, A., Fita, I., and Loewen, P.C. (2007) Two alternative substrate paths for compound I formation and reduction in catalase-peroxidase KatG from *Burkholderia pseudomallei*. *Proteins* **66:** 219-228.

DeLano, W.L. (2002) The PyMOL Molecular Graphics System. http://www.pymol.org.

Derat, E., Shaik, S., Rovira, C., Vidossich, P., and Alfonso-Prieto, M. (2007) The effect of a water molecule on the mechanism of formation of compound 0 in horseradish peroxidase. *J. Am. Chem. Soc.* **129:** 6346-6347.

Deretic, V., Philipp, W., Dhandayuthapani, S., Mudd, M.H., Curcic, R., Garbe, T., Heym, B., Via, L.E., and Cole, S.T. (1995) *Mycobacterium tuberculosis* is a natural mutant with an inactivated oxidative-stress regulatory gene: implications for sensitivity to isoniazid. *Mol. Microbiol.* **17:** 889-900.

Dessen, A., Quémard, A., Blanchard, J.S., Jacobs, W.R. Jr., Sacchettini, J.C. (1995) Crystal structure and function of the isoniazid target of *Mycobacterium tuberculosis*. *Science* **267:** 1638-1641.

Diaz, A., Horjales, E., Rudino-Pinera, E., Arreola, R., and Hansberg, W. (2004) Unusual Cys-Tyr covalent bond in a large catalase. *J. Mol. Biol.* **342:** 971-985.

Diaz, G.A. and Wayne, L.G. (1974) Isolation and characterization of catalases produced by *Mycobacterium tuberculosis*. *Am. Rev. Respir. Dis.* **110:** 312-319.

Donald, L.J., Krokhin, O.V., Duckworth, H.W., Wiseman, B., Deemagarn, T., Singh, R., Switala, J., Carpena, X., Fita, I., and Loewen, P.C. (2003) Characterization of the catalase-peroxidase (KatG) from *Burkholderia pseudomallei* by mass spectrometry. *J. Biol. Chem.* **278:** 35687-35692.

Dunford, H.B. (1999) *Heme Peroxidases.* Wiley-VCH. New York.

Edwards, S.L., Raag, R., Wariishi, H., Gold, M.H., and Poulos, T.L. (1993) Crystal structure of lignin peroxidase. *Proc. Natl. Acad Sci. U.S.A.* **90:** 750-754.

Emsley, P. and Cowtan, K. (2004) *Coot*: model-building tools for molecular graphics. *Acta Crystallogr.* **D60:** 2126-2132.

Erman, J.E., Vitello, L.B., Mauro, J.M., and Kraut, J. (1989) Detection of an oxyferryl porphyrin π-cation-radical intermediate in the reaction between hydrogen peroxide and a mutant yeast cytochrome *c* peroxidase. Evidence for tryptophan-191 involvement in the radical site of compound I. *Biochemistry* **28:** 7992-7995.

Erman, J. E. and Vitello, L. B. (2002) Yeast cytochrome *c* peroxidase: mechanistic studies via protein engineering. *Biochim. Biophys. Acta* **1597:** 193-220.

Escolar, L., Perez-Martin, J., and de Lorenzo, V. (1999) Opening the iron box: transcriptional metalloregulation by the Fur protein. *J. Bacteriol.* **181:** 6223-6229.

Faguy, D.M., and Doolittle, W.F. (2000) Horizontal transfer of catalase-peroxidase genes between archea and pathogenic bacteria. *Trends. Genet.* **16:** 196-197.

Farrington, J.A., Land, E.J., and Swallow, J. (1980) The one-electron reduction potentials of NAD. *Biochim Biophys Acta* **590:** 273-276.

Finzel, B., Poulos, T. L., and Kraut J. (1984) Crystal structure of yeast cytochrome *c* peroxidase refined at 1.7-Å resolution. *J. Biol. Chem.* **259:** 13027-13036.

Fita, I. and Rossmann, M.G. (1985) The active center of catalase. *J. Mol. Biol.* **185:** 21-37.

Fita, I., Silva, A.M., Murthy, M.R.N., and Rossmann, M.G. (1986) The refined structure of beef liver catalase at 2.5 Å resolution. *Acta Crystallogr.* **B42:** 497-515.

Fox, H.H. (1952) The chemical approach to the control of tuberculosis. *Science* **116:** 129-134.

Gajhede, M., Schuller, D.J., Henriksen, A., Smith, A.T., and Poulos, T.L. (1997) Crystal structure of horseradish peroxidase C at 2.15 Å resolution. *Nat. Struct. Biol.* **4:** 1032-1038.

Gaspar, T., Penel, C., and Greppin, H. (1992) Peroxidases 1980-1990. Topics and detailed literature on molecular, biochemical and physiological aspects. University of Geneva, Geneva.

Gaspar, T., Penel, C., Thorpe, T., and Greppin, H. (1982) Peroxidases 1970-1980. A survey of their biochemical and physiological roles in higher plants. University of Geneva, Geneva.

Ghiladi, R.A., Cabelli, D.E., and Ortiz de Montellano, P.R. (2004) Superoxide reactivity of KatG: insights into isoniazid resistance pathways in TB. *J. Am. Chem. Soc.* **126:** 4772-4773.

Ghiladi, R.A., Knudsen, G.M., Medzihradszky, K.F., and Ortiz de Montellano, P.R. (2005a) The Met-Tyr-Trp cross-link in *Mycobacterium tuberculosis* catalase-peroxidase (KatG): autocatalytic formation and effect on enzyme catalysis and spectroscopic properties. *J. Biol. Chem.* **280:** 22651-22663.

Ghiladi, R.A., Medzihradszky, K.F., and Ortiz de Montellano, P.R. (2005b) Role of the Met-Tyr-Trp cross-link in *Mycobacterium tuberculosis* catalase-peroxidase (KatG) as revealed by KatG(M255I). *Biochemistry.* **44:** 15093-15105.

Ghiladi, R.A., Medzihradszky, K.F., Rusnak, F.M., and Ortiz de Montellano, P.R. (2005c) Correlation between isoniazid resistance and superoxide reactivity in *Mycobacterium tuberculosis* KatG. *J. Am. Chem. Soc.* **127:** 13428–13442.

Gouet, P., Jouve, H.M., and Dideberg, O. (1995) Crystal structure of *Proteus mirabilis* PR catalase with and without bound NADPH. *J. Mol. Biol.* **249:** 933-954.

Håkansson, K.O., Brugna, M., and Tasse, L. (2004) The three-dimensional structure of catalase from *Enterococcus faecalis. Acta Crystallogr.* **D60:** 1374-1380.

Hara, I., Ichise, N., Kojima, K., Kondo, H., Ohgiya, S., Matsuyama, H., and Yumoto, I. (2007) Relationship between the size of the bottleneck 15 Å from iron in the main channel and the reactivity of catalase corresponding to the molecular size of substrates. *Biochemistry* **46:** 11-22.

Henriksen, A., Schuller, D.J., Meno, K., Welinder, K.G., Smith, A.T., Gajhede, M. (1998) Structural interactions between horseradish peroxidase C and the substrate benzohydroxamic acid determined by X-ray crystallography. *Biochemistry* **37:** 8054-8060.

Henriksen, A., Welinder, K.G., and Gajhede, M. (1998) Structure of barley grain peroxidase refined at 1.9 Å resolution. A plant peroxidase reversibly inactivated at neutral pH. *J. Biol. Chem.* **273:** 2241-2248.

Heym, B., Alzari, P.M., Honore, N., and Cole, S.T. (1995) Missence mutations in the catalase-peroxidase gene, katG, are associated with isoniazid resistance in *Mycobacterium tuberculosis*. *Mol. Microbiol.* **15:** 235-245.

Heym, B., and Cole, S.T. (1992) Isolation and characterization of isoniazid-resistant mutants of *Mycobacterium smegmatis* and *M. aurum*. *Res. Microbiol.* **143:** 721-730.

Hillar, A., Peters, B., Pauls, R., Loboda, A., Zhang, H., Mauk, A.G., and Loewen, P.C. (2000) Modulation of the activities of catalase-peroxidase HPI of *Escherichia coli* by site-directed mutagenesis. *Biochemistry.* **39:** 5868-5875.

Humphrey W., Dalke A., and Schulten, K. (1996) VMD—visual molecular dynamics. *J. Mol Graphics* **14:** 33–38.

Imlay, J.A. (2008) Cellular defenses against superoxide and hydrogen peroxide. *Annu. Rev. Biochem.* **77:** 755-776.

Ivancich, A., Jakopitsch, C., Auer, M., Un, S., and Obinger, C. (2003) Protein-based radicals in the catalase-peroxidase of *Synechocystis* PCC6803: a multifrequency EPR investigation of wild-type and variants on the environment of the heme active site. *J. Am. Chem. Soc.* **125:** 14093-14102.

Jakopitsch, C., Auer, M., Ivancich, A., Rüker, F., Furtmüller, P.G., and Obinger, C. (2003a) Total conversion of bifunctional catalase-peroxidase (KatG) to monofunctional peroxidase by exchange of a conserved distal side tyrosine. *J. Biol. Chem.* **278:** 20185-20191.

Jakopitsch, C., Auer, M., Regelsberger, G., Jantschko, W., Furtmüller, P.G., Rüker, F., and Obinger, C. (2003c) Distal site aspartate is essential in the catalase activity of catalase-peroxidases. *Biochemistry*. **42:** 5292-5300.

Jakopitsch, C., Droghetti, E., Schmuckenschlager, F., Furtmüller, P.G., Smulevich, G., and Obinger, C. (2005) The role of the main access channel of catalase-peroxidase in catalysis. *J. Biol. Chem.* **280:** 42411-42422.

Jakopitsch, C., Ivancich, A., Schmuckenschlager, F., Wanasinghe, A., Pöltl, G., Furtmüller, P.G., Rüker, F., and Obinger, C. (2004) Influence of the unusual covalent adduct on the kinetics and formation of radical intermediates in *Synechocystis* catalase-peroxidase. *J. Biol. Chem.* **279:** 46082-46095.

Jakopitsch, C., Kolarich, D., Petutschnig, G., Furtmüller, P.G., and Obinger, C. (2003b) Distal side tryptophan, tyrosine and methionine in catalase-peroxidases are covalently linked in solution. *FEBS Lett.* **522:** 135-140.

Jakopitsch, C., Obinger, C., Un, S., and Ivancich, A. (2006) Identification of Trp106 as the tryptophanyl radical intermediate in *Synechocystis* PCC6803 catalase-peroxidase by multifrequency electron paramagnetic resonance spectroscopy. *J. Inorg. Biochem.* **100:** 1091-1099.

Jakopitsch, C., Vlasits, J., Wiseman, B., Loewen, P.C., and Obinger, C. (2007) Redox intermediates in the catalase cycle of catalase-peroxidases from *Synechocystis* PCC 6803, *Burkholderia pseudomallei*, and *Mycobacterium tuberculosis*. *Biochemistry* **46:** 1183-1193.

Johnsson, K., Froland, W.A., and Schultz, P.G. (1997) Overexpression, purification, and characterization of the catalase-peroxidase KatG from *Mycobacterium tuberculosis*. *J. Biol. Chem.* **272:** 2834-2840.

Jones, T.A., Zou, J.Y., Cowan S.W., and Kjeldgaard, M. (1991) Improved methods for building protein models in electron density maps. *Acta Crystallogr.* **A47:** 1100–1119.

Klotz, M.G. and Loewen, P.C. (2003) The molecular evolution of catalatic hydroperoxidases: Evidence for multiple lateral transfer of genes between prokaryota and from bacteria into eukaryota. *Mol. Biol. Evol.* **20:** 1098-1112.

Ko, T.P., Day, J., Malkin, A.J., and McPherson, A. (1999) Structure of orthorhombic crystals of beef liver catalase. *Acta Crystallogr.* **D55:** 1383-1394.

Kono, Y. and Fridovich, I. (1983) Isolation and characterization of the pseudocatalase of *Lactobacillus plantarum*. *J. Biol. Chem.* **258:** 6015-6019.

Kunishima, N., Fukuyama, K., Matsubara, H., Hatanaka, H., Shibano, Y., and Amachi, T. (1994) Crystal structure of the fungal peroxidase from *Arthromyces ramosus* at 1.9 Å resolution. Structural comparisons with the lignin and cytochrome *c* peroxidases. *J. Mol. Biol.* **235:** 331-344.

Kunishima, N., Amada, F., Fukuyama, K., Kawamoto, M., Matsunaga, T., and Matsubara, H. (1996) Pentacoordination of the heme iron of *Arthromyces ramosus* peroxidase shown by a 1.8 Å resolution crystallographic study at pH 4.5. *FEBS Lett.* **378:** 291-294.

Kunkel, T.A., Roberts, J.D., and Zankour, R.A. (1987) Rapid and efficient site-directed mutagenesis without phenotypic selection. *Methods Enzymol.* **154:** 367-382.

Layne, E. (1957) Spectrophotometric and turbidimetric methods for measuring proteins. *Methods Enzymol.* **3:** 447-454.

Leadbetter, J.R., Crosby, L.D., and Breznak J.A. (1998) *Methanobrevibacter filiformis* sp. nov., A filamentous methanogen from termite hindguts. *Arch Microbiol.* **169:** 287-92.

Lei, B., Wei, C.J., and Tu, S.C. (2000) Action mechanism of antitubercular isoniazid. Activation by *Mycobacterium tuberculosis* KatG, isolation, and characterization of *inhA* inhibitor. *J. Biol. Chem.* **275:** 2520-2526.

Loew, G. and Dupuis, M. (1996) Structure of a model transient peroxide intermediate of peroxidases by *ab initio* methods. *J. Am. Chem. Soc.* **118:** 10584-10587.

Loew, O. (1901) Catalase, a new enzyme of general occurrence with special reference to the tobacco plant. *U.S. Dept. Agr. Rep.* **68:** 47.

Loewen, P.C., Carpena, X., Rovira, C., Ivancich, A., Perez-Luque, R., Haas, R., Odenbreit, S., Nicholls, P., and Fita, I. (2004) Structure of *Helicobacter pylori* catalase, with and without formic acid bound, at 1.6 Å resolution. *Biochemistry* **43:** 3089-3103.

Loewen, P.C., and Switala, J. (1986) Purification and characterization of catalase HPII from *Escherichia coli. Biochem. Cell Biol.* **64:** 638-646.

Loewen, P.C., Switala, J., Smolenski, M., and Triggs-Raine, B.L. (1990) Molecular characterization of three mutations in katG affecting the activity of hydroperoxidase I of *Escherichia coli. Biochem. Cell Biol.* **68:** 1037-1044.

Loewen, P. C., Switala, J., and Triggs-Raine, B. L. (1985) Catalases HPI and HPII in *Escherichia coli* are induced independently. *Arch. Biochem. Biophys.* **243:** 144-149.

Magliozzo, R.S., and Marcinkeviciene, J.A. (1997) The role of Mn(II)-peroxidase activity of mycobacterial catalase-peroxidase in activation of the antibiotic isoniazid. *J. Biol. Chem.* **272:** 8867-8870.

Maté, M.J., Zamocky, M., Nykyri, L.M., Herzog, C., Alzari, P.M., Betzel, C., Koller, F., and Fita, I. (1999) Structure of catalase-A from *Saccaromyces cerevisiae. J. Mol. Biol.* **286:** 135-139.

Mathews, R.A. and Wittenberg, J.B. (1979) Cytochrome *c* peroxidase. Interconversion of chemically and enzymatically reactive and unreactive forms of the ferric protein. *J. Biol. Chem.* **254:** 5991 - 5996

McCord, J.M., and Fridovich, I. (1988) Superoxide dismutase: the first twenty years (1968-1988). *Free Radic. Biol. Med.* **5:** 363–369.

Mdluli, K., Slayden, R.A., Zhu, Y., Ramaswamy, S., Pan, X., Mead, D., Crane, D.D., Musser, J.M., and Barry, C.E. 3rd. (1998) Inhibition of a *Mycobacterium tuberculosis* beta-ketoacyl ACP synthase by isoniazid. *Science* **280:** 1607-1610.

Mead, D.A., Skorupa, E.S., and Kemper, B. (1985) Single-stranded DNA SP6 promoter plasmids for engineering mutant RNAs and proteins: synthesis of a 'stretched' prepoparathyroid hormone. *Nucl. Acids. Res.* **13:** 1103-1118.

Metcalfe, C., Macdonald, I.K., Murphy, E.J., Brown, K.A., Raven, E.L., and Moody, P.C. (2008) The tuberculosis prodrug isoniazid bound to activating peroxidases. *J. Biol. Chem.* **283:** 6193-6200.

Meyer, H. and Malley, J. (1912) Uber hydrazinederivate de pyridincarbonsauren. *Montashefte. Chem.* **33:** 393-414.

Middlebrook, G. (1952) Sterilization of tubercle bacilli by isonicotinic acid hydrazide and the incidence of variants resistant to the drug *in vitro*. *Am. Rev. Tuberc.* **65:** 765-767.

Middlebrook, G. (1954) Isoniazid-resistance and catalase activity of tubercle bacilli; a preliminary report. *Am. Rev. Tuberc.* **69:** 471-472.

Middlebrook, G. and Cohn, M.L. (1953) Some observations on the pathogenicity of isoniazid-resistant variants of tubercle bacilli. *Science* **118:** 297-299.

Mo, L., Zhang, W., Wang, J., Weng, X.H., Chen, S., Shoa, L.Y., Pang, M.Y., and Chen, Z. (2004) Three-dimensional model and molecular mechanism of *Mycobacterium tuberculosis* catalase-peroxidase (KatG) and isonizid-resistant katG mutants. *Microbial Drug Resist.* **10:** 269-279.

Moore, R.L., Powell, L.J., and Goodwin, D.C. (2008) The kinetic properties producing the perfunctory pH profiles of catalase-peroxidases. *Biochim Biophys Acta.* **1784:** 900-907.

Mulvey, M.R., Switala, J., Borys, A., and Loewen, P.C. (1990) Regulation of transcription of *kat*E and *kat*F in *Escherichia coli*. *J. Bacteriol.* **172:**6713-6720.

Murshudov, G.N., Vagin, A.A., and Dodson, E.J. (1997) Refinement of macromolecular structures by the maximum likelihood method. *Acta Crystallog.* **D53:** 240–255.

Murshudov, G.N., Melik-Adamyan, W.R., Grebenko, A.I., Barynin, V.V., Vagin, A.A., Vainshtein, B.K., dauter, Z., and Wilson, K.S. (1982) Three-dimensional structure of catalase from *Micrococcus lysodeikticus* at 1.5 Å resolution. *FEBS Lett.* **312:** 127-131.

Murthy, M.R.N., Reid, T.J., Sicignano, A., Tanaka, N., and Rossmann, M.G. (1981) Structure of beef liver catalase. *J. Mol. Biol.* **152:** 465-499.

Nagy, J.M., Cass, A.E., and Brown, K.A. (1997) Purification and characterization of recombinant catalase-peroxidase, which confers isoniazid sensitivity in *Mycobacterium tuberculosis*. *J. Biol. Chem.* **272:** 31265-31271.

Nguyen, N., Claparols, C., Bernadou, J., and Meunier, B. (2001) A fast and efficient metal-mediated oxidation of isoniazid and identification of isoniazid-NAD(H) adducts. *Chembiochem* **2:** 877-883.

Nicholls, P., Fita, I., and Loewen, P. C. (2001) Enzymology and structure of catalases. *Adv. Inorg. Chem.* **51:**51-106.

Oldham, M.L., Brash, A.R., and Newcomer, M.E. (2005) The structure of a core allene oxide synthase reveals a catalase adapted for metabolism of a fatty acid hydroperoxide. *Proc. Natl. Acad. Sci. U.S.A.* **102:** 297-302.

Offe, H.A., Siefken, W., and Domagk, G. (1952) The tuberculostatic activity of hydrazine derivatives from pyridine carboxylic acids and carbonyl compounds. *Z. Naturforsch.* **7b:** 462-468.

Otwinowski, Z., and Minor, W. (1996) Processing of X-ray diffraction data collected in oscillation mode. *Methods Enzymol.* **276:** 307–326.

Pansy, F., Stander, H., and Donovick, R. (1952) *In vitro* studies on isonicotinic acid hydrazide. *Am. Rev. Tuberc.* **65:** 761-764.

Passardi, F., Bakalovic, N., Teixeira, F.K., Margis-Pinheiro, M., Penel, C., and Dunand, D. (2007a) Prokaryotic origins of the non-animal peroxidase superfamily and organelle-mediated transmission to eukaryotes. *Genomics* **89:** 567-579.

Passardi, F., Cosio, C., Penel, C., and Dunand, C. (2005) Peroxidases have more functions than a Swiss army knife. *Plant Cell Rep.* **24:** 255-265.

Passardi, F., Zámocky, M., Favet, J., Jakopitch, C., Penel, C., Obinger, C., and Dunand, C. (2007b) Phylogenetic distribution of catalase-peroxidases: Are there patches of order in chaos? *Gene* **397:** 101-113.

Patterson, W. R. and Poulos, T. L. (1995) Crystal structure of recombinant pea cytosolic ascorbate peroxidase. *Biochemistry* **34:** 4331-4341.

Patterson, W. R., Poulos, T. L., and Goodin, D. B. (1995) Identification of a porphyrin π-cation radical in ascorbate peroxidase compound I. *Biochemistry* **34:** 4342-4345.

Pelletier, H. and Kraut, J. (1992) Crystal structure of a complex between electron transfer partners, cytochrome *c* peroxidase and cytochrome *c*. *Science* **258:** 1748-1755.

Petersen, J.F., Kadziola, A., and Larsen, S. (1994) Three-dimensional structure of a recombinant peroxidase from *Coprinus cinereus* at 2.6 Å resolution. *FEBS Lett.* **339:** 291-296.

Pipirou, Z., Bottrill, A.R., Metcalfe, C.M., Mistry, S.C., Badyal, S.K., Rawlings, B.J., and Raven, E.L. (2007) Autocatalytic formation of a covalent link between tryptophan 41 and the heme in ascorbate peroxidase. *Biochemistry* **46:** 2174-2180.

Pipirou, Z., Guallar, V., Basran, J., Metcalfe, C.L., Murphy, E.J., Bottrill, A.R., Mistry, S.C., and Raven, E.L. (2009) Peroxide-dependent formation of a covent link between Trp51 and the heme in cytochrome *c* peroxidase. *Biochemistry* **48:** 3593-3599.

Planche, L.A. (1810) Note sur la sophistication de la résine de jalap et sur les moyens de la reconnaître, etc. *Bull. Pharmacie* **2:** 578-580.

Poulos, T.L., Edwards, S.L., Wariishi, H., and Gold, M.H. (1993) Crystallographic refinement of lignin peroxidase at 2 A. *J. Biol. Chem.* **268:** 4429-4440.

Poulos, T. L., Freer, S. T., Alden, R. A., Edwards, S. L., Skoglund, U., Takio, K., Eriksson, B., Xuong, H. -h., Yonetani, T., and Kraut, J. (1980) The crystal structure of cytochrome *c* peroxidase. *J. Biol. Chem.* **255:** 575-580.

Poulos, T. L. and Kraut, J. (1980) The stereochemistry of peroxidase catalysis. *J. Biol. Chem.* **255:** 8199-8205.

Putnam, C.D., Arvai, A.S., Bourne, Y., and Tainer, J.A. (1999) Active and inhibited human catalase structures: ligand and NADPH binding and catalytic mechanism. *J. Mol. Biol.* **296:** 295-309.

Quémard, A., Sacchettini, J.C., Dessen, A., Vilcheze, C., Bittman, R., Jacobs, W.R. Jr., and Blanchard, J.S. (1995) Enzymatic characterization of the target for isoniazid in *Mycobacterium tuberculosis*. *Biochemistry* **34:** 8235-8241.

Ramaswamy, S.V., Reich, R., Dou, S.J., Jasperse, L., Pan, X., Wanger, A., Quitugua, T., and Graviss, E.A. (2003) Single nucleotide polymorphisms in genes associated with isoniazid resistance in *Mycobacterium tuberculosis*. *Antimicrob. Agents Chemother.* **47:** 1241-50.

Regelsberger, G., Jakopitsch, C., Rüker, F., Krois, D., Peschek, G.A., and Obinger, C. (2000) Effect of distal cavity mutations on the formation of compound I in catalase-peroxidases. *J. Biol. Chem.* **275:** 22854-22861.

Robitzek, E.H. and Selikoff, I.J. (1952) Hydrazine derivatives of isonicotinic acid (Rimifon, Marsilid) in the treatment of progressive caseous-pneumonic tuberculosis. A priminary report. *Am. Rev. Tuberc.* **65:** 402-428.

Rodriguez-Lopez, J.N., Smith, A.T., and Thorneley, R.N.F. (1996) Role of arginine 38 in horseradish peroxidase. *J. Biol. Chem.* **271:** 4023-4030.

Rørth, M., and Jensen, P.K. (1967) Determination of catalase activity by means of the Clark oxygen electrode. *Biochim. Biophys. Acta.* **139:** 171-173.

Rozwarski, D.A., Grant, G.A., Barton, D.H., Jacobs, W.R. Jr., and Sacchettini, J.C. (1998) Modification of the NADH of the isoniazid target (InhA) from *Mycobacterium tuberculosis*. *Science* **279:** 98-102.

Riise, E.K., Lorentzen, M.S., Helland, R., Smalas, A.O., Leiros, H.K.S., and Willassen, N.P. (2007) The first structure of a cold-active catalase from *Vibrio salmonicida* at 1.96 Å reveals structural aspects of cold adaptation. *Acta Crystallogr.* **D63:** 135-148.

Saint-Joanis, B., Souchon, H., Wilming, M., Johnsson, K., Alzari, P.M., and Cole, S.T. (1999) Use of site-directed mutagenesis to probe the structure, function and isoniazid activation of the catalase-peroxidase, KatG from *Mycobacterium tuberculosis*. *Biochem J.* **338 (Part 3):** 753-760.

Sambrook, J., Fritsch, E.F., and Maniatis, T. (1989) *Molecular Cloning: A Laboratory Manual.* Cold Harbour Laboratory. Cold Spring Harbour Press. New York.

Sanger, F.S., Nicklen, S., and Coulson, A.R. (1977) DNA sequencing with chain terminating inhibitors. *Proc. Natl. Acad. Sci. U.S.A.* **74:** 5463-5467.

Santoni, E., Jakopitsch, C., Obinger, C., and Smulevich, G. (2004) Comparison between catalase-peroxidase and cytochrome *c* peroxidase. The role of the hydrogen-bond networks for protein stability and catalysis. *Biochemistry* **43:** 5792-5802.

Santos, W. G. D., Pacheco, I., Liu, M., Teixeira, M., Xavier, A. V., and LeGall, J. (2000) Purification and characterization of an iron superoxide dismutase and a catalase from the sulfate-reducing bacterium *Desulfovibrio gigas*. *J. Bacteriol.* **182:** 796-804.

Schonbaum, G.R. (1973) New complexes of peroxidases with hydroxamic acids, hydrazides, and amides. *J. Biol. Chem.* **248:** 502 – 511.

Schuller, D.J., Ban, N., Huystee, R.B., McPherson, A., and Poulos, T.L. (1996) The crystal structure of peanut peroxidase. *Structure* **4:** 311-321.

Sharp, K. H., Mewies, M., Moody, P. C. E., and Raven, E. L. (2003) Crystal structure of the ascorbate peroxidase-ascorbate complex. *Nat. Struc. Biol.* **10:** 303-307.

Shoeb, H.A., Bowman, Jr. B.U., Ottolenghi, A.C., and Merola, A.J. (1985a) Peroxidase-mediated oxidation of isoniazid. *Antimicrob Agents Chemother.* **27:** 399-403.

Shoeb, H.A., Bowman, Jr. B.U., Ottolenghi, A.C., and Merola, A.J. (1985b) Evidence for the generation of active oxygen by isoniazid treatment of extracts of *Mycobacterium tuberculosis* H37R. *Antimicrob Agents Chemother.* **27:** 404-407.

Shoeb, H.A., Bowman, Jr. B.U., Ottolenghi, A.C., and Merola, A.J. (1985c) Enzymatic and nonenzymatic superoxide-generating reactions of isoniazid. *Antimicrob Agents Chemother.* **27:** 408-412.

Sicking, W., Korth, H-G., de Groot, H., and Sustmann, R. (2008) On the functional role of a water molecule in clade 3 catalases: a proposal for the mechanism by which NADPH prevents the formation of compound II. *J. Am. Chem. Soc.* **130:** 7345–7356.

Silva, M.S., Senna, S.G., Rineiro, M.O., Valim, A.R., Telles, M.A., Kritski, A., Morlock, G.P., Cooksey, R.C., Zaha, A., and Rossetti, M.L. (2003) Mutations in *katG*, *inhA*, and *ahpC* genes of Brazilian isoniazid-resistant isolates of *Mycobacterium tuberculosis.* *J. Clinl. Microbiolo.* **41:** 4471-4474.

Singh, A.K., Kumar, R.K., Pandey, N., Singh, N., Sinha, N., Bushan, A., Kaur, P., Sharma, H., and Singh, T.P. (2009) Mode of binding of the tuberculosis prodrug isoniazid to heme peroxidases: binding studies and crystal structure of bovine lactoperoxidase with isoniazid at 2.7 Å resolution. *J Biol Chem* In press M109.060327.

Singh, R. (2006) Comparative study of catalase-peroxidases (KatGs). *Ph.D. thesis.* Department of Microbiology. University of Manitoba.

Singh, R., Switala, J., Loewen, P.C., and Ivancich, A. (2007) Two [Fe(IV)=O Trp$^{\bullet}$] intermediates in *M. tuberculosis* catalase-peroxidase discriminated by multifrequency (9-285 GHz) EPR spectroscopy: reactivity toward isoniazid. *J. Am. Chem. Soc.* **129:** 15954-15963.

Singh, R., Wiseman, B., Deemagarn, T., Donald, L.J., Duckworth, H.W., Carpena, X., Fita, I., and Loewen, P.C. (2004) Catalase-peroxidase (KatG) exhibit NADH oxidase activity. *J. Biol. Chem.* **279:** 43098-43106.

Singh, R., Wiseman, B., Deemagarn, T., Jha, V., Switala, J., and Loewen, P.C. (2008) Comparative study of catalase-peroxidases (KatGs). *Arch. Biochem. Biophys.* **471:** 207-214.

Sivaraja, M., Goodin, D. B., Smith, M., and Hoffman, B. M. (1989) Identification by ENDOR of Trp191 as the free-radical site in cytochrome *c* peroxidase compound ES. *Science* **245:** 738-740.

Shima, S., Sordel-Klippert, M., Brioukhanov, A., Netrusov, A., Linder, D., and Thauer, R. K. (2001) Characterization of a heme-dependent catalase from *Methanobrevibacter arboriphilus*. *Appl. Environ. Microbiol.* **67:** 3041-3045.

Smulevich, G., Jakopitsch, C., Droghetti, E., and Obinger, C. (2006) Probing the structure and bifunctionality of catalase-peroxidase (KatG). *J. Inorg. Biochem.* **100:** 568-585.

Sollewijn Gelpke, M.D., Lee, J., and Gold, M.H. (2002) Lignin peroxidase oxidation of veratryl alcohol: effects of the mutants H82A, Q222A, W171A, and F267L. *Biochemistry* **41:** 3498-3506.

Spolitak, T., Dawson, J.H., and Ballou, D.P. (2005) Reaction of ferric cytochrome P450cam with peracids: kinetic characterization of intermediates on the reaction pathway. *J. Biol. Chem.* **280:** 20300-20309.

Storz, G. and Imlay, J. A. (1999) Oxidative stress. *Curr. Opin. Microbiol.* **2:** 188-194.

Sundaramoorthy, M., Kishi, K., Gold, M.H., and Poulos, T.L. (1994) The crystal structure of manganese peroxidase from *Phanerochaete chrysosporium* at 2.06-Å resolution. *J. Biol. Chem.* **269:** 32759-32767.

Switala, J. and Loewen, P.C. (2002) Diversity of properties among catalases. *Arch. Biochem. Biophys.* **401:** 145-154.

Switala, J., O'Neil, J.O., and Loewen, P.C. (1999) Catalase HPII from *Escherichia coli* exhibits enhanced resistance to denaturation. *Biochemistry* **38:** 3895-3901.

Ten-I, T., Kumasaka, T., Higuchi, W., Tanaka, S., Yoshimatsu, K., Fujiwara, T., and Sato, T. (2007) Expression, purification, crystallization and preliminary X-ray analysis of the Met244Ala variant of catalase-peroxidase (KatG) from the haloarchaeon *Haloarcula marismortui*. *Acta Crystallogr.* **F63:** 940-943.

Triggs-Raine, B.L., Doble, B.W., Mulvey, M.R., Sorby, P.A., and Loewen, P.C. (1988) Nucleotide sequence of *katG*, encoding catalase HPI of *Escherichia coli*. *J. Bacteriol.* **170:** 4415-4419.

Vainshtein, B.K., Melik-Adamyan, W.R., Barynin, V.V., Vagin, A.A., and Grebenko, A.I. (1981) Three-dimensional structure of the enzyme catalase. *Nature* **293:** 411-412.

Vainshtein, B.K., Melik-Adamyan, W.R., Barynin, V.V., Vagin, A.A., Grebenko, A.I., Borisov, V.V., Bartels, K.S., Fita, I., and Rossmann, M.G. (1986) Three-dimensional structure of catalase from *Penicillium vitale* at 2.0 Å resolution. *J. Mol. Biol.* **188:** 49-61.

Veich, N.C. (2004) Horseradish peroxidase: a modern view of a classic enzyme. *Phytochemistry* **65:** 249-259.

Vidossich, P., Alfonso-Prieto, M., Carpena, X., Loewen, P.C., Fita, I., and Rovira, C. (2007) Versatility of the electronic structure of compound I in catalase-peroxidases. *J. Am. Chem. Soc.* **129:** 13436-13446.

Vieira, J. and Messing, J. (1987) Production of single-stranded plasmid DNA. *Methods Enzymol.* **153:** 3-11.

Vilchèze, C. and Jacobs, W.R. Jr. (2007) The mechanism of isoniazid killing: clarity through the scope of genetics. *Annu. Rev. Microbiol.* **61:** 35-50.

Vilchèze, C., Wang, F., Arai, M., Hazbón, M.H., Colangeli, R., Kremer, L., Weisbrod, T.R., Alland, D., Sacchettini, J.C., and Jacobs, W.R. Jr. (2006) Transfer of a point mutation in *Mycobacterium tuberculosis inhA* resolves the target of isoniazid. *Nat. Med.* **12:** 1027-29.

Vlasits, J., Jakopitsch, C., Schwanninger, M., Holubar, P., and Obinger, C. (2007) Hydrogen peroxide oxidation by catalase-peroxidase follows a non-scrambling mechanism. *FEBS Let.* **581:** 320-324.

Wada, K., Tada, T., Nakamura, Y., Kinoshita, T., Tamoi, M., Sigeoka, S., and Nishimura, K. (2002) Crystallization and preliminary X-ray diffraction studied of catalase-peroxidase from *Synechococcus* PCC7492. *Acta Crystallogr.* **D58:** 157-159.

Wang, J-Y., Burger, R.M., and Drlica, K. (1998) Role of superoxide in catalase-peroxidase-mediated isoniazid action against Mycobacteria. *Antimicrob Agents Chemother.* **42:** 709-711.

Warburg, O. and Christian, W. (1941) Isolierung und kristallisation des garungsfrements enolase. *Biochemische Zeitschrift* **310:** 384-421.

Weber, K., Pringle, J.R., and Osborn, M. (1972) Measurement of molecular weights by electrophoresis on SDS-polyacrylamide gels. *Methods Enzymol.* **26:** 3-27.

Wei, C.J., Lei, B., Musser, J.M., and Tu, S.C. (2003) Isoniazid activation defects in recombinant *Mycobacterium tuberculosis* catalase-peroxidase (KatG) mutants evident in InhA inhibitor production. *Antimicrob. Agents Chemother.* **47:** 670-675.

Welinder, K.G. (1991) Bacterial catalase-peroxidases are gene duplicated members of the plant peroxidase superfamily. *Biochim. Biophys. Acta.* **1080:** 215-220.

Welinder, K.G. (1992) Superfamily of plant, fungal and bacterial peroxidases. *Curr. Opin. Struct. Biol.* **2:** 388-393.

Wengenack, N.L., Hoard, H.M., and Rusnak, F. (1999) Isoniazid oxidation by *Mycobacterium tuberculosis* KatG: a role for superoxide which correlates with isoniazid susceptibility. *J. Am. Chem. Soc.* **121:** 9748-9749.

Wengenack NL, Todorovic S, Yu L, and Rusnak F. (1998) Evidence for differential binding of isoniazid by *Mycobacterium tuberculosis* KatG and the isoniazid-resistant mutant KatG(S315T). *Biochemistry* **37:** 15825-15834.

Wengenack, N.L., Uhl, J.R., St. Amand, A.L., Tomlinson, A.J., Benson, L.M., Naylor, S., Kline, B.C., Cockerill, F.R. 3rd, and Rusnak, F. (1997) Recombinant *Mycobacterium tuberculosis* KatG(S315T) is a competent catalase-peroxidase with reduced activity toward isoniazid. *J. Infect. Dis.* **176:** 722-727.

Winder, F.G. and Collins, P.B. (1970) Inhibition by isoniazid of synthesis of mycolic acids in Mycobacterium tuberculosis. *J. Gen. Microbiol.* **63:** 41-48.

Wiseman, B., Colin, J., Smith, A.T., Ivancich, A., and Loewen, P.C. (2009) Mechanistic insight into the initiation step of the reaction of *Burkholderia pseudomallei* catalase-peroxidase with peroxyacetic acid. *J. Biol. Inorg. Chem.* **14:** 801-811.

Yamada, Y., Fujiwara, T., Sato, T., Igarashi, N., and Tanaka, N. (2002) The 2.0 Å crystal structure of the catalase-peroxidase from *Haloarcula marismortui. Nat. Struct. Biol.* **9:** 691-695.

Yamada, Y., Saijo, S., Sato, T., Igarashi, N., Usui, H., Fujiwara, T., and Tanaka, N. (2001) Crystallization and preliminary X-ray analysis of catalase-peroxidase from halophilic archaeon *Haloarcula marismortui. Acta Crystallogr.* **D57:** 1157-1158.

Yanisch-Perron, C., Vieira, J., and Messing, J. (1985) Improving M13 phage cloning vectors and host strains: nucleotide sequences of the M13mp18 and pUC19 vectors. *Gene* **33:** 103-119.

Yu, S., Girotto, S., Lee, C., and Magliozzo, R.S. (2003a) Reduced affinity for isoniazid in the S315T mutant of *Mycobacterium tuberculosis* KatG is a key factor in antibiotic resistance. *J. Biol. Chem.* **278:** 14769-14775.

Yu, S., Girotto, S., Zhao, X., and Magliozzo, R.S. (2003b) Rapid formation of compound II and a tyrosyl radical in the Y229F mutant of *Mycobacterium tuberculosis* catalase-peroxidase disrupts catalase but not peroxidase function. *J. Biol. Chem.* **278:** 44121-44127.

Zabinski, R.F., and Blanchard, J.S. (1997) The requirement for manganese and oxygen in the isoniazid-dependent inactivation of *Mycobacterium tuberculosis* enoyl reductase. *J. Am. Chem. Soc.* **119:** 2331-2332.

Zahrt, T.C., Song, J., Siple, J., and Deretic, V. (2001) Mycobacterial FurA is a negative regulator of catalase-peroxidase gene *katG*. *Mol. Microbiol.* **39:** 1174-1185.

Zámocky, M. (2004) Phylogenic relationships in class I of the superfamily of bacterial, fungal, and plant peroxidases. *Eur. J. Biochem.* **271:** 3297-3309.

Zámocky, M., Furtmüller, P.G., and Obinger, C. (2008a) Evolution of catalases from bacteria to humans. *Antioxid. Redox Signal.* **10:** 1-21.

Zámocky, M., Jakopitsch, C., Furtmüller, P. G, Dunand, C., and Obinger, C. (2008b) The peroxidase-cyclooxygenase superfamily: Reconstructed evolution of critical enzymes of the innate immune system. *Proteins* **71:** 589-605

Zámocky, M., Janeček, Š., and Koller, F. (2000) Common phylogeny of catalase-peroxidases and ascorbate peroxidase. *Gene* **256:** 169-182.

Zhang, M., Yue, J., Yang, Y.P., Zhang, H.M., Lei, J.Q., Jin, R.L., Zhang, X.L., and Wang, H.H. (2005) Detection of mutations associated with isoniazid resistance in *Mycobacterium tuberculosis* isolates from China. *J. Clin. Microbiol.* **43:** 5477-82.

Zhang, Y., Heym, B., Allen, B., Young, S., and Cole, S. (1992) The catalase-peroxidase gene and isoniazid resistance of *Mycobacterium tuberculosis*. *Nature* **358:** 591-593.

Zhao, X., Girotto, S., Yu, S., and Magliozzo, R. S. (2004) Evidence for Radical Formation at Tyr-353 in *Mycobacterium tuberculosis* Catalase-Peroxidase (KatG). *J. Biol. Chem.* **279:** 7606-7612.

Zhao, X., Yu, H., Yu, S., Wang, F., Sacchettini, J.C., and Magliozzo, R.S. (2006) Hydrogen peroxide-mediated isoniazid activation catalyzed by *Mycobacterium tuberculosis* catalase-peroxidase (KatG) and its S315T mutant. *Biochemisrty* **45:** 4131-4140.

Zheng, M. and Storz, G. (2000) Redox sensing by prokaryotic transcription factors. *Biochem. Pharmacol.* **59:** 1-6.